Search for the Top Quark in the All-Jets Channel

by

Cathy Elaine Cretsinger

Submitted in Partial Fulfillment
of the
Requirements for the Degree
Doctor of Philosophy

Supervised by
Professor Thomas Ferbel
Department of Physics and Astronomy
The College
Arts and Sciences

University of Rochester
Rochester, New York
1995

Curriculum Vitae

The author was born in Fort Wayne, Indiana, on November 9, 1967. She attended the California Institute of Technology from 1986 to 1987 and the University of Arizona from 1988 to 1990. She graduated Summa Cum Laude from the University of Arizona with a Bachelor of Science degree in 1990. She came to the University of Rochester in the fall of 1990 and began graduate studies in Physics. She received a Sproull Fellowship in 1990 and 1991, and a Graduate Student Fellowship from the National Science Foundation in 1991, 1992, and 1993. She pursued her research in Particle Physics under the direction of Professor Thomas Ferbel and received the Master of Arts degree in 1992.

Acknowledgements

First, I thank my advisor, Tom Ferbel, who has been helpful in many ways, including his knowledge of physics and his detailed editorial comments.

This project would have been inconceivable without the work of the many members of the DØ collaboration. I thank them for the years they have devoted to building and operating the detector, and developing the software tools that are necessary to any analysis project.

I also thank the members and leaders of the Top Physics Group for their hard work, which led to the observation of the top quark in other channels, and for their contributions to the analysis of the all-jets channel. I am especially indebted to the members of the $t\bar{t} \rightarrow$ all-jets subgroup for their determination to succeed and their ceaseless toil, and to Boaz Klima, Chip Stewart and Norm Amos for leading the subgroup over the years.

No group of people could be more helpful (or vocal) in evaluating a student's work than my fellow collaborators from the University of Rochester. I thank them all for their willingness to share their insights and for their friendship.

Finally, I thank all my friends inside and outside the collaboration, who helped me stay sane through five and a half long years; my parents, who have always been supportive; and my husband, who will always be my hero.

This material is based upon work supported in part under a National Science Foundation Graduate Fellowship. Additional support was provided by the United States Department of Energy and by the Sproull Fellowship program at the University of Rochester.

Abstract

We have searched for $t\bar{t}$ production in the "all-jets" channel, in which both the t and $\bar{t}$ quarks decay to lighter quarks that are observed as collimated jets of particles. The search was performed using the DØ detector at the Tevatron $p\bar{p}$ collider at Fermilab, operating at a center-of-mass energy of 1.8 TeV. Data corresponding to an integrated luminosity of 58.4 pb^{-1} were used in the search.

According to the Standard Model, the all-jets channel is the most common decay mode of $t\bar{t}$. However, the signal is obscured by an enormous background from other processes that produce multijet final states. To reject this background, we defined four kinematic parameters that provide discrimination between $t\bar{t}$ production and other processes, and imposed requirements on the values of these parameters. To further enhance the proportion of signal in the data, and to estimate the remaining background, we selected interactions that were likely to include a heavy (b or c) quark by requiring that each event have a muon with low transverse momentum near a jet.

After imposing all selection criteria, we found 11 candidate events, with an expected background of 7.7 ± 1.1 events. This corresponds to a cross section of 4.9 ± 4.6 pb for $t\bar{t}$ production. Although the size of the excess is not large enough to establish the unambiguous presence of a signal, the cross section found for the all-jets channel is consistent with that expected from other $t\bar{t}$ modes.

Contents

List of Tables

List of Figures

Foreword

The DØ experiment is a large collaborative effort, in which more than 400 physicists and students from 48 institutions are currently participating. The University of Rochester group is active in monitoring of liquid-argon purity, in data acquisition and reconstruction efforts, and in analysis of data in the areas of QCD and top-quark physics. The group is also participating in development and construction projects for a scintillating-fiber tracking chamber to be included in the upgrade of the DØ detector.

I have been involved in work in several of these areas. I participated in early research and development projects for the scintillating fiber tracker by helping to develop techniques for the construction of ribbons of scintillating fibers and by performing studies of photodetector characteristics. In addition, I created an event-display program for use in a cosmic-ray test of a prototype scintillating fiber tracker. During the 1993–95 running period of the Tevatron, I was actively involved in the day-to-day operation of the data acquisition system. I also participated in operating the offline processor farm that reconstructed events from the detector signals and have had primary responsibility for maintaining and improving the control processes that handle communications between the server and worker nodes on the farm. My analysis project has been the search for the top quark in the all-jets channel.

Chapter 1

Introduction

In the twentieth century, scientists have made great progress in the quest for the fundamental constituents of matter. Atoms, which a hundred years ago were thought to be elementary particles, were found to possess structure. Explaining atomic structure required an entirely new physical theory, quantum mechanics, which radically altered earlier concepts of subatomic particles. Scientists soon learned that the atomic nucleus was made of even smaller particles: protons and neutrons. New forces were postulated to explain nuclear interactions. More recently, structure was found within the proton and neutron. Today, the known elementary particles are six quarks and six leptons, along with the gluons, W and Z bosons, and photons, which interact with the quarks and leptons.

The interactions of these particles over the full range of energies accessible to study (a few electron volts to 1.8 TeV) are described by the Standard Model. This model is the basis for almost all modern experiments in particle physics. At places such as the Fermi National Accelerator Laboratory, the Stanford Linear Accelerator Center, and the European Laboratory for Particle Physics (CERN), physicists measure the model's free parameters, attempt to identify new particles whose existence the model predicts, and search for phenomena or particles beyond those encompassed by the model.

Like our knowledge of elementary particles, the methods used to study them have also changed a great deal in this century. In 1911, Rutherford was able to discover the atomic nucleus using a beam of alpha particles and a fluorescent zinc sulfide screen [1]. In the 1930s and 40s, experimenters using photographic emulsions to study cosmic rays discovered the muon and the pion [1]. In 1995, the top quark was found in proton-antiproton collisions at Fermilab's Tevatron collider [2, 3]. This accelerator produces beams of protons and antiprotons that collide at an energy of 1.8 TeV (almost a thousand times their rest energy) hundreds of thousands of times per second. Identification of the top quark required the use of detectors weighing over four thousand tons, to study more than two years' worth of these collisions. Finding the Higgs boson, another particle expected in the Standard Model, will probably require an even larger accelerator and more advanced detectors.

The discovery of the top quark was the most recent confirmation of the Standard Model, which predicted its existence. However, many questions about the top quark still remain unanswered. Better measurements of its mass, its production cross section and its branching ratios are needed to confirm their consistency with the model's predictions. This dissertation describes a search for top-quark production in one of its expected decay channels, the "all-jets" channel. The results will be used to address some of these questions.

In this chapter, we review the Standard Model and the state of our knowledge of production and decay properties of the top quark and indicate why the top quark is a necessary part of the theory. In Chapter 2, we describe the Tevatron collider and the DØ detector. Particle identification is discussed in Chapter 3, and selection of the data samples used in our search in Chapter 4. Chapter 5 is devoted to the techniques used to distinguish a signal for $t\bar{t}$ production in the all-jets channel from backgrounds. In Chapter 6, the final selection criteria and results of the search are presented. Conclusions are drawn in Chapter 7.

1.1 The Standard Model

Physicists began searching for the top quark in the late 1970s, when it was established that this particle was a necessary ingredient of the Standard Model. To understand why the top quark is required, and to establish the context that underlies studies of this quark, we will begin with a brief review of the Standard Model. More detailed descriptions are presented in many textbooks, including [1, 4, 5, 6].

At the subatomic level, matter is composed of a small number of particles, the quarks and leptons, each with spin $\frac{1}{2}$. These particles interact via four fundamental forces: gravity, electromagnetism, and the strong and weak interactions. Quarks are distinguished from leptons by the fact that the former participate in strong interactions while the latter do not. Neutrinos are further distinguished by their lack of electric charge; they participate only in weak interactions.

The known "matter" particles are the six types (or "flavors") of quarks, three charged leptons, and three lepton neutrinos. These particles are listed in the first part of Table 1.1, where they are grouped into three "families" (or "generations") based on similarities among their properties. As the listed masses indicate, particles in the second family are more massive than their counterparts in the first; those in the third family are more massive still. The masses for u, d, c, s, and b quarks are somewhat ill-defined because these quarks exist only within hadrons. For each matter particle listed in the table, there is a corresponding particle of antimatter, which has the same mass, but opposite internal quantum numbers.

Ordinary matter is made up of particles from the first family: electrons; electron

Table 1.1: Particles in the Standard Model. The mass or mass limit for each matter particle is given in parenthesis, in units of MeV/c^2. The values used are those of Ref. [7], except for the t quark mass, which is taken from Ref. [2].

Matter Particles (fermions)				
				Charge (e)
Quarks	$u(\sim 5)$ $d(\sim 10)$	$c(\sim 1300)$ $s(\sim 200)$	$t(200,000)$ $b(\sim 5000)$	$+\frac{2}{3}$ $-\frac{1}{3}$
Leptons	$\nu_e(< 0.0000051)$ $e(0.511)$	$\nu_\mu(< 0.3)$ $\mu(106)$	$\nu_\tau(< 31)$ $\tau(1777)$	0 -1
Gauge Particles (bosons)				
Field		**Mass (GeV/c^2)**		
Electromagnetic	γ (photon)	0		0
Strong	g (gluon)	0		0
Weak	$W^\pm$ Z	80.22 ± 0.26 91.187 ± 0.007		± 1 0
Scalar Higgs	H	> 58.4		0

neutrinos, which are released in beta decay; and up and down quarks, which make up protons and neutrons. The other particles can be created in accelerators, but they decay to the lighter particles of the first family. Ignoring cosmic rays, particles from the second and third families are present in ordinary matter only in virtual form. The Standard Model does not explain the number of observed families; the existence of the quarks and leptons listed in Table 1.1 is an experimental fact. Only the ν_τ has not as yet been observed directly, but there is compelling indirect evidence of its existence [7].

Interactions are described in the formalism of quantum field theory [6]. Each distinct fundamental particle is assumed to be the quantum of a field. Interactions are modeled by requiring these fields to be invariant under an appropriate set of local symmetry transformations; this leads to the introduction of one or more new fields. These "gauge" fields interact with the matter fields and, if the symmetry group is non-Abelian, with each other as well. Each gauge field is quantized, and its quantum is identified with a particle that mediates the interaction. These particles are listed in the second part of Table 1.1. The Higgs field is special, and its role will be discussed later.

Of the four fundamental interactions, only gravity has not been described successfully by a quantum field theory [6, Chapter 19], so it is not part of the Standard Model. Conveniently, at currently accessible energies, the effect of gravity on elementary particles can be ignored because the interaction is extremely weak compared to the other interactions—the electromagnetic interaction, for instance, is typically $\sim 10^{36}$ times stronger [4, Chapter IX]. We will now look in more detail at the other interactions, which are included in the Standard Model.

The first successful quantum field theory was quantum electrodynamics (QED), which describes electromagnetic interactions to an unprecedented precision. QED is based on $U(1)$ symmetry transformations of the fields corresponding to charged particles [5, Chapter II], [6, Chapters 4–7]. Preserving gauge invariance of the interaction requires a neutral field with spin 1 that couples to charged particles in proportion to their charges; the quantum of this field is the photon (γ). The proportionality constant is $\alpha_{\rm EM}$.

When the momentum transfer in the interaction is small, corresponding to interactions at large distances, the electromagnetic coupling $\alpha_{\rm EM}$ is about $\frac{1}{137}$. However, at larger momentum transfers, corresponding to distances shorter than $\hbar c/m_e$, $\alpha_{\rm EM}$ increases. This is an effect of polarization of the vacuum, which at large distances "screens" the bare charge so that only part of it is observable. At short distances, particles penetrate part of the screening, more of the bare charge is effective, and $\alpha_{\mathrm{EM}} = e^2/\hbar c$ increases. In fact, according to the theory, the bare charge of an electron is infinite, but this infinity is masked by an infinite vacuum polarization, leaving a finite apparent charge (e) to be observed. The mathematics of these cancelling infinities is called renormalization, and it is a general feature of all useful (renormalizable) gauge theories [6, Chapter 7].

Precision tests of QED have shown remarkable agreement between theory and experiment. For instance, measurements of the Lamb shift, an energy difference between the $2s^{1/2}$ and $2p^{1/2}$ energy levels of the hydrogen atom, are in excellent agreement with predictions from higher-order effects in QED [5]. Perhaps the most famous test of QED is its prediction of an anomalous magnetic moment of the electron, which agrees with experiments to an astonishing one part in 10^7 [5]. Not surprisingly, many physicists regard QED as the most successful theory in all of physics [8].

Now we turn to the strong interaction, which is described by quantum chromodynamics (QCD) [5, Chapter IV], [6, Chapter 11]. QCD is based on the invariance of matter fields under $SU(3)$ transformations of "color charge," which is a three-valued internal degree of freedom assigned to quarks. Leptons are assigned zero color because they do not participate in strong interactions. Local $SU(3)$ invariance requires eight spin-1 mediating fields. These are associated with eight gluons, each of which has a distinct (properly symmetrized) color state. A gluon couples a quark of a given flavor and color to a quark of the same flavor but different color. Because $SU(3)$ is a non-Abelian symmetry group, gluons carry color, and they can interact among themselves. All strong interactions are characterized by a single coupling strength, α_S.

Just as in the case of α_{EM}, this coupling "constant" depends on the distance, or renormalization, scale of the interaction. However, α_S becomes smaller, not larger, as the distance decreases. This is due to the non-Abelian nature of the gluon fields, and it gives rise to "asymptotic freedom," or the phenomenon that at short distances, quarks and gluons within a hadron act almost independently of each other [5, pages 380–397]. As a result, scattering of quarks and gluons with large momentum transfer can be described by a perturbative expansion in α_S [7].

The fact that free quarks have not been observed can be explained if colored particles are not allowed to exist in isolation. Although this has not yet been proven [6, Chapter 15], this confinement is believed to be a property of QCD. Because α_S grows for increased distance scales, a perturbative expansion in α_S is not possible at low energies, but numeric calculations indicate that the energy in the QCD field diverges as the separation between colored particles increases. If this is true, it follows that colored particles must be confined in color-neutral bound states within a relatively limited spatial volume. Consequently, quarks can exist only inside composite particles called hadrons, of which there are two types: mesons, which consist of quark-antiquark pairs, and baryons, which consist of three quarks. Likewise, free gluons cannot exist. Color-neutral bound states consisting of several gluons, or of gluons and quarks, are theoretically possible but have not been definitively established (see Ref. [7] for a review of searches for such states).

One implication of confinement is the inevitable formation of "jets" in any process involving interacting partons, *i.e.*, either quarks or gluons. As interacting partons move away from each other, the energy in the field between them increases to the point where new quark-antiquark pairs are produced from the vacuum, forming bound states with the original partons. In a high-energy collision, this fragmentation produces collimated jets of hadrons, which can be observed with a suitable detector. The partons themselves cannot be observed.

Perturbative calculations in QCD are notoriously ambiguous for finite scales, and determining the energies of partons from the jets they create is also somewhat problematic, so the precision with which QCD can be compared to experiment is not as high as with QED. Within these limitations, characteristics of jet production have been studied and found to be in good agreement with QCD predictions at leading order and next-to-leading order in α_S. These characteristics include the inclusive differential cross section for jet production, and correlations between jets in two-jet events [9]. Furthermore, bound states of heavy quarks (c and b) have been studied, and their properties are also consistent with predictions of QCD [7].

Finally, we turn to the quantum field theory of the weak interaction. This theory is complicated by the fact that the W and Z bosons have mass. A renormalizable gauge theory of the weak interaction requires that the mediators be massless [5, page 371], [6, Chapter 7]. However, treating the weak and electromagnetic fields together yields a renormalizable theory through the mechanism of spontaneous symmetry breaking.

The weak interaction can be modeled using "weak isospin," T, an internal quantum number that is mathematically analogous to angular momentum [5, pages 496–506]. Like spin, only one component of the weak isospin vector, usually denoted T_3, has a definite value. To account for the observed parity violation in weak interactions, right-handed fermions, such as e_R^-, u_R, and d_R, are assigned to weak isospin singlets. Left-handed fermions are assigned to doublets ($T = \frac{1}{2}$). In each generation, the two leptons constitute a doublet, with the neutrino having $T_3 = \frac{1}{2}$ and the charged lepton having $T_3 = -\frac{1}{2}$; the two quarks constitute a second doublet, with $T_3 = \frac{1}{2}$ corresponding to the quark with positive charge. The interaction is mediated by a weak isospin triplet of massive fields—W^+, W^-, and W^0—which couple equally to all weak isopin doublets. The charged W fields have $T_3 = \pm 1$, so they couple one member of a doublet to the other; thus, charged leptons are coupled to neutrinos (*e.g.*, $W^- \to e^- \bar{\nu}_e$), and quarks of one flavor (*e.g.*,

u) are coupled to quarks of another (*e.g.*, d). It is worth noting that the quark eigenstates of the weak interaction are not the same as those of the strong interaction. There is a mixing in the weak sector that accounts for the decays of strange and bottom quarks by allowing them to couple to a virtual W^- and a positively charged quark of another generation (*e.g.*, $W^- \rightarrow b\bar{c}$). The mixing is parametrized by the Cabibbo-Kobayashi-Maskawa (CKM) matrix, the elements of which are determined experimentally [7]. The neutral field has $T_3 = 0$, and as a result of the CKM parametrization, it effectively preserves both quark and lepton flavor.

The quanta of the charged W fields are readily identified as intermediate vector bosons. The W^0 field, however, includes a contribution from the electromagnetic field and cannot be identified as a distinct particle. It is therefore necessary to consider a combined electroweak theory, in which the remainder of the electromagnetic field is added to the three W fields [5, pages 491–496]. This field couples to weak hypercharge, defined as $Q - T_3$, where Q is the electric charge and T_3 is the known component of weak isospin. Separating the electromagnetic and weak contributions to the neutral fields yields two fields, whose quanta are the photon and the Z boson. In addition, it follows that the Z boson is more massive than the charged W bosons. Their masses are related by the electroweak mixing parameter, $\sin\theta_W$, whose value is not predicted by theory.

Now we turn to the problem caused by the fact that the mediators are massive. The solution is the Higgs mechanism, through which mediators can acquire mass by coupling to a symmetry-breaking field [5, pages 502–528], [6, Chapter 10]. This mechanism produces a renormalizable theory with massive mediators. Thus, the Standard Model incorporates an electroweak theory based on the requirement of invariance under the symmetry group $SU(2)_L \times U(1)_Y$, where the subscript L denotes that only left-handed particles are involved in the $SU(2)$ transformations, and Y denotes weak hypercharge. This theory yields four massless gauge fields:

a weak isospin triplet from $SU(2)$ invariance and a singlet field arising from $U(1)$ invariance. The quanta of these fields are the W and Z bosons and the photon. To explain the observed W and Z masses, a new field is introduced that breaks the symmetry by its coupling to the gauge fields. A suitable choice for the vacuum state of this new field induces mass in the W and Z fields but leaves the photon massless. A consequence of this procedure is the existence of a new field, whose quantum is the neutral scalar Higgs boson, H^0, the final particle in Table 1.1. This particle couples not only to the W and Z bosons, but also to the fermions. The latter interactions cause the fermions to acquire mass, but the fermion masses and their relative sizes are free parameters of the theory, as is the mass of the Higgs boson itself.

This electroweak model has been extensively tested since its development in the early 1970s. The W and Z bosons were first observed in 1983 [10], and their cross sections, masses, and decays agree with predictions [7]. Most recently, the existence of the top quark—which, as we shall see, is required by the model—has been demonstrated. The Higgs boson, however, has not yet been detected. It might be observed at the higher energies of the the Large Hadron Collider, now under construction at CERN.

Many physicists find the Standard Model unsatisfying because it includes many parameters whose values cannot be predicted from the theory, such as the masses of the fermions and of the W and Z bosons, the charges of the particles, the coupling strengths of the interactions, the electroweak mixing angle, the CKM matrix elements, and so on. Furthermore, gravitational effects, which become important at very high energies, must be incorporated into any final theory of elementary particles. As a result, numerous speculative theories of physics beyond the Standard Model have been developed, including supersymmetry, Grand Unified Theories, and superstring theories [6, Chapters 18–21]. However, no evidence of a departure from the Standard Model, or in support of any new theories, has yet been clearly demonstrated.

1.2 The Top Quark

1.2.1 Why the Standard Model Requires the Top Quark

The Standard Model does not predict the number of fermion generations. However, it does require that each generation consist of two quarks and two leptons. Thus, when the tau lepton and the bottom, or b, quark were discovered, in 1975 and 1977, respectively, it seemed apparent that a third generation existed, and the top quark was predicted as the weak-isospin partner of the b quark [1].

There are several reasons why the top quark is expected to exist. The first involves the decay of the b quark. If the b were a weak isospin singlet, it would have to decay by somehow mixing with the s (or the d) quark, which would then decay by coupling to a virtual W boson, accounting for the observed b-quark decays. However, the strange quark could also radiate a virtual Z boson, which would give rise to other, unobserved, decay modes for the b quark. The ratio of Z-channel to W-channel decays would be about 0.11. Studies of b-quark decays rule out the Z channels to well below this level [11, Chapter 25]. Assuming that the rest of the Standard Model is correct, it follows that that the b quark must decay by directly coupling to a virtual W boson, which implies that it has $T = \frac{1}{2}$ and is part of a weak isospin doublet, not a singlet.

Confirmation that the b quark is in fact a member of a weak isospin doublet comes from measurements of the charge asymmetry in the production of $b\bar{b}$ pairs in e^+e^- collisions at the Z mass. These measurements yield a value for T_3 of the left-handed b quark of $-0.504^{+0.018}_{-0.011}$ [11, Chapter 25], which is consistent with a

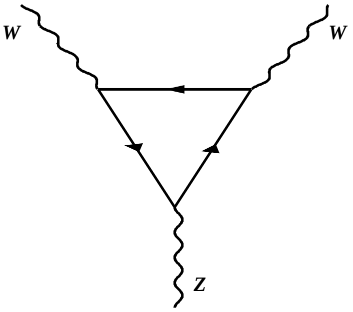

Figure 1.1: Triangle diagram for an anomalous WWZ coupling.

doublet but inconsistent with a singlet interpretation.

The top quark is also needed in the Standard Model to deal with corrections to the couplings among the W and Z bosons. At higher orders, there are anomalies in the WWZ coupling, due to "triangle" diagrams such as Fig. 1.1, in which the fermion line can represent any quark or lepton. Each fermion in such a diagram contributes a divergent term to the coupling; however, these divergences will cancel if the sum of the charges of all fermions in each generation is zero (each quark enters the sum three times, due to its three distinct color possibilities) [6, Chapter 12]. Thus, given the existence of the b quark and tau lepton, the top quark is required to preserve the standard electroweak theory.

The W and Z masses and $\sin\theta_W$ are related at lowest order, and higher-order processes involving fermion loops modify the W and Z masses from their leading-order values [12]. The mass of the top quark can therefore be predicted from measurements of the electroweak parameters of the Standard Model. Based on theoretical calculations of these corrections and on precise measurements of the electroweak parameters, the mass of the top quark has been estimated to be 169^{+16+17}_{-18-20} GeV/c^2 [7]. (The first set of errors is due to statistical uncertainty, and the second due to systematic uncertainty in the calculation.) However, like the preceding arguments, this estimate assumes the presence of the top quark but does not prove its existence.

1.2.2 Discovery of the Top Quark

Proof that the top quark exists requires a direct search. Searches conducted prior to 1994 at CERN and Fermilab established lower limits on the mass of the top quark, based on the absence of characteristic signals in excess of expectation from background. In 1993, the D0 collaboration set the highest limit on the mass of the top quark, 131 GeV/c^2 (95% confidence level) [13]. In 1994, the CDF collaboration reported evidence for top-quark production, with a cross section of $13.9^{+6.1}_{-4.8}$ pb and a mass of $174 \pm 10^{+13}_{-12}$ GeV/c^2; however, the observed excess of events was not large enough to rule out background fluctuations [14].

In 1995, after collecting substantially more data, both D0 and CDF observed clear signals due to the production of $t\bar{t}$ pairs. D0 reported a cross section of 6.4 ± 2.2 pb and a mass of $199^{+19}_{-21} \pm 22$ GeV/c^2 [2]. CDF reported a cross section of $6.8^{+3.6}_{-2.4}$ pb and a mass of $176 \pm 8 \pm 10$ GeV/c^2 [3]. (Again, the first set of errors reflects statistical, and the second systematic, uncertainty in the measurement.) However, much remains to be learned about the top quark. The mass, cross section, and branching ratios to the different decay channels must be measured more precisely so that comparisons with predictions of the Standard Model can be made. In addition, measurements of the masses of the top quark and W boson can be used to constrain the mass of the Higgs boson. At present, a meaningful constraint is not possible due to the large uncertainty in the mass of the top quark. The uncertainty in the W mass, while not large, also must be reduced before this constraint will be effective.

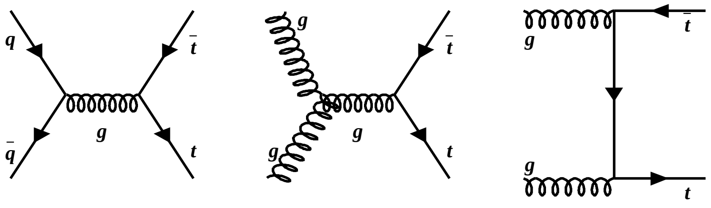

Figure 1.2: Leading order diagrams for $t\bar{t}$ production.

1.2.3 Top Production and Decay

The Tevatron collider produces proton-antiproton collisions at a center-of-mass energy $\sqrt{s} = 1.8$ TeV. At this energy, the Standard Model predicts that the top quark will be produced mainly in the form of $t\bar{t}$ pairs, through the $q\bar{q}$ annihilation and gluon fusion diagrams shown in Fig. 1.2 [12]. For a given mass, the cross section for $t\bar{t}$ production ($\sigma_{t\bar{t}}$) can be calculated using QCD [15]. As shown in Fig. 1.3, $\sigma_{t\bar{t}}$ decreases with increasing top-quark mass. The relative contribution expected from the gluon-initiated processes decreases with increasing top-quark mass. Because the gluon content of the proton is not known very accurately, the theoretical uncertainty is greater at lower mass.

In the Standard Model, the top quark almost always decays to a W boson and a b quark. The decay proceeds quite rapidly, and the top-quark lifetime is $\sim 10^{-24}$ seconds, too short for it to form bound states with other quarks [16]. Hadrons containing top quarks are not likely to exist, and only the decay products of individual top quarks should be observable. For a $t\bar{t}$ pair, we expect to observe a jet from each of the two b quarks, and additional particles from the decays of the two W bosons. The W bosons can decay either to lepton-neutrino pairs, or

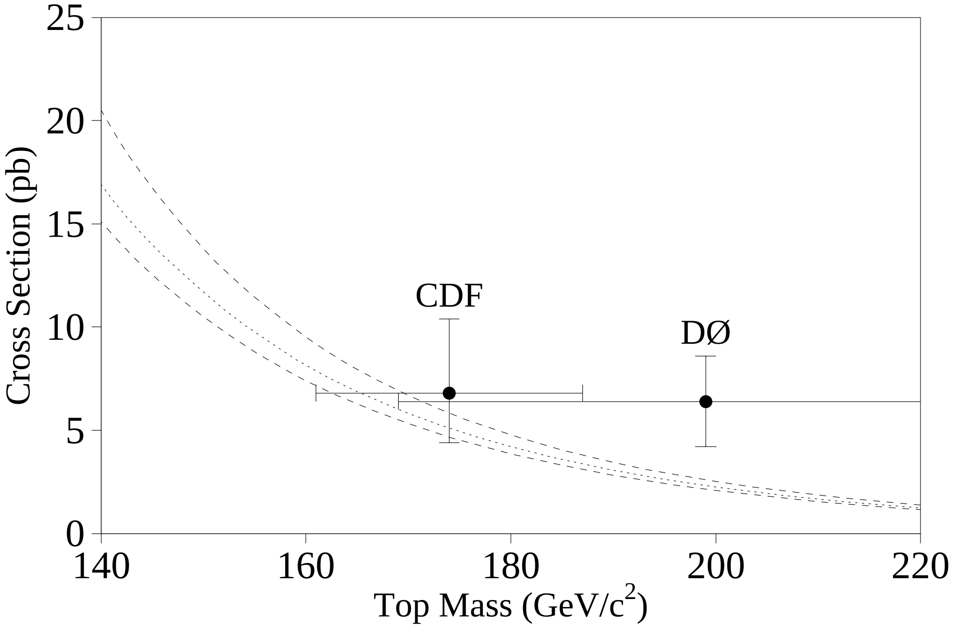

Figure 1.3: Theoretical prediction [15] for $t\bar{t}$ cross section as a function of top-quark mass. The outer curves indicate the uncertainty for the central prediction. Results from DØ and CDF are also shown.

Table 1.2: Branching fractions for $t\bar{t}$ decay channels.

		$W^+ \rightarrow$ $q\bar{q}'$ (2/3)	 $e^+\nu_e$ (1/9)	 $\mu^+\nu_\mu$ (1/9)	 $\tau^+\nu_\tau$ (1/9)
$W^- \rightarrow q'\bar{q}$	(2/3)	4/9	2/27	2/27	2/27
$e^-\bar{\nu}_e$	(1/9)	2/27	1/81	1/81	1/81
$\mu^-\bar{\nu}_\mu$	(1/9)	2/27	1/81	1/81	1/81
$\tau^-\bar{\nu}_\tau$	(1/9)	2/27	1/81	1/81	1/81

to light quarks that fragment into jets. The specific W decays distinguish one $t\bar{t}$ decay channel from another.

Because the coupling strength of W bosons to fermions is universal, we can predict the branching ratio for any possible $t\bar{t}$ decay channel simply by counting states. Taking into account the three colors available for each quark pair, it follows that each leptonic decay mode of the W boson has a branching fraction of 1/9, and each quark decay mode has a branching fraction of 1/3. This results in the predictions of Table 1.2 for the $t\bar{t}$ branching fractions [12]. Published results from DØ and CDF have used those channels for their searches where at least one of the W bosons decays to an electron or muon: the ee, $e\mu$, $\mu\mu$, e+jets, and μ+jets channels.

Each kind of channel has certain advantages. The dilepton channels have the smallest branching ratios, but backgrounds from other processes are small, especially in the $e\mu$ channel. However, the presence of two neutrinos, which are not measured, makes it difficult to reconstruct the mass of the top quark. In the lepton+jets channels, the branching fraction is larger, but there are substantial backgrounds from other processes that produce W+jets final states. There is only one neutrino, which simplifies somewhat the determination of the top mass. For that reason, the current DØ and CDF mass measurements are based on candidates from the lepton+jets channels. The channels involving tau leptons have also received attention, but taus decay before they can be detected, which complicates the task of identifying these final states. Nonetheless, the tau channels are interesting because they are sensitive to new particles predicted by supersymmetric extensions of the Standard Model [12].

The focus of this dissertation is the "all-jets" channel, in which both W bosons decay to quarks that are observed in the detector as jets of hadrons. This channel offers the advantages of a large branching fraction (44%) and complete kinematic information that can be used to reconstruct the top mass. The signature consists of the two b-quark jets and two more jets from the decay of each W boson, for a total of six. Additional jets may be produced by gluons that are radiated by the quarks in the final state (final state radiation, or FSR), or by the colliding partons (initial state radiation, or ISR).

The signal in the all-jets channel is obscured by an extremely large background from other QCD or semi-weak processes that mimic the six-jet signature. Because of the ambiguities in perturbative QCD calculations, these processes cannot be modeled very precisely. For example, a "tree-level" calculation of the $gg \to 6g$ process involves 2,520 subprocesses and is well beyond the capacity of modern supercomputers [17]. Approximation techniques that agree well with the exact tree-level results for five-jet final states can be used to estimate the size of the six-jet cross section [18, 19]. If each jet is required to have transverse momentum of at least 25 GeV/c, the six-jet cross section is expected to be about 200 pb. This is clearly much larger than the expected cross section for $t\bar{t}$ production.

Extracting a top signal from this background is a challenging problem. Because most QCD events do not produce b quarks, identifying one or both of the b-quark jets can improve the signal to background ratio. This alone is not likely to yield a clear signal, and more discrimination may be needed. Here, we will present several parameters used for characterizing event "shape." These parameters are sensitive to differences in the kinematics of processes that produce $t\bar{t}$ and ordinary QCD multijet final states. On the basis of these parameters, and in conjunction with identification ("tagging") of b-quark jets, we should be able to achieve sensitivity to a top-quark signal in the all-jets mode.

Chapter 2

Experimental Apparatus

In this chapter, we describe the accelerator and detector used to collect data for this search for the top quark. The Tevatron collides protons and antiproton at a center-of-mass energy ($\sqrt{s}$) of 1.8 TeV, currently the highest energy available at any accelerator in the world. The DØ detector is a sophisticated tool for studying the products of these collisions.

2.1 The Tevatron

Operation of the Tevatron collider requires that proton and antiproton beams be produced and accelerated to 900 GeV each. We will briefly describe the steps in this process. A more detailed account of accelerator operations is given in Ref. [20]. Ref. [21] offers an account of the history of the Tevatron.

The accelerator complex is shown in Fig. 2.1. It consists of the pre-accelerator, a linear accelerator (Linac), the Booster synchrotron, the Main Ring, the antiproton source, and finally, the Tevatron. The operation of all of the accelerators exploits simple principles of electrodynamics. First, the energy of a charged particle is increased by applying an electric field along its trajectory. Second, particles are steered by applying a magnetic field in the plane normal to the trajectory, causing them to change direction and thereby maintain the desired orbit [22].

2.1.1 The Accelerators

The acceleration cycle begins in the pre-accelerator [20], shown at the top of Fig. 2.1. Here, hydrogen gas is converted to negatively charged hydrogen ions (H^-) in a magnetron surface-plasma source [20, 23]. An electric field, pulsed at a rate of 15 Hz, extracts ions from the source and accelerates them to 18 keV. Magnets bend the beam through a right angle to filter out unwanted particles. Next, an electrostatic accelerator, the high voltage for which is produced by a Cockcroft-Walton generator, boosts the energy of the ions to 750 keV. The H^- ions are then injected into the linear accelerator, or Linac.

The Linac [20] consists of a series of drift tubes with field gaps between them. Radio-frequency (RF) electromagnetic fields are present in these gaps. Particle injection into the Linac is synchronized with the RF oscillations so that the H^- ions are in the gaps when the field is in the accelerating direction, and in the tubes (shielded from the field) when the field is in the reverse direction. In addition, the time variation of the RF field strength is exploited to minimize the momentum spread of the beam. Particles traveling faster than the average particle arrive in the field gap early, when the field is small, and consequently, they receive a smaller accelerating "kick." Similarly, slower particles arrive late and receive a larger than average kick from the field. At the end of the Linac, the H^- ions pass through a carbon foil, which strips off their electrons, leaving bare protons to continue through the acceleration cycle. The energy of the beam at the end of the Linac was 200 MeV until Fall, 1993, when a section of the Linac was replaced. This

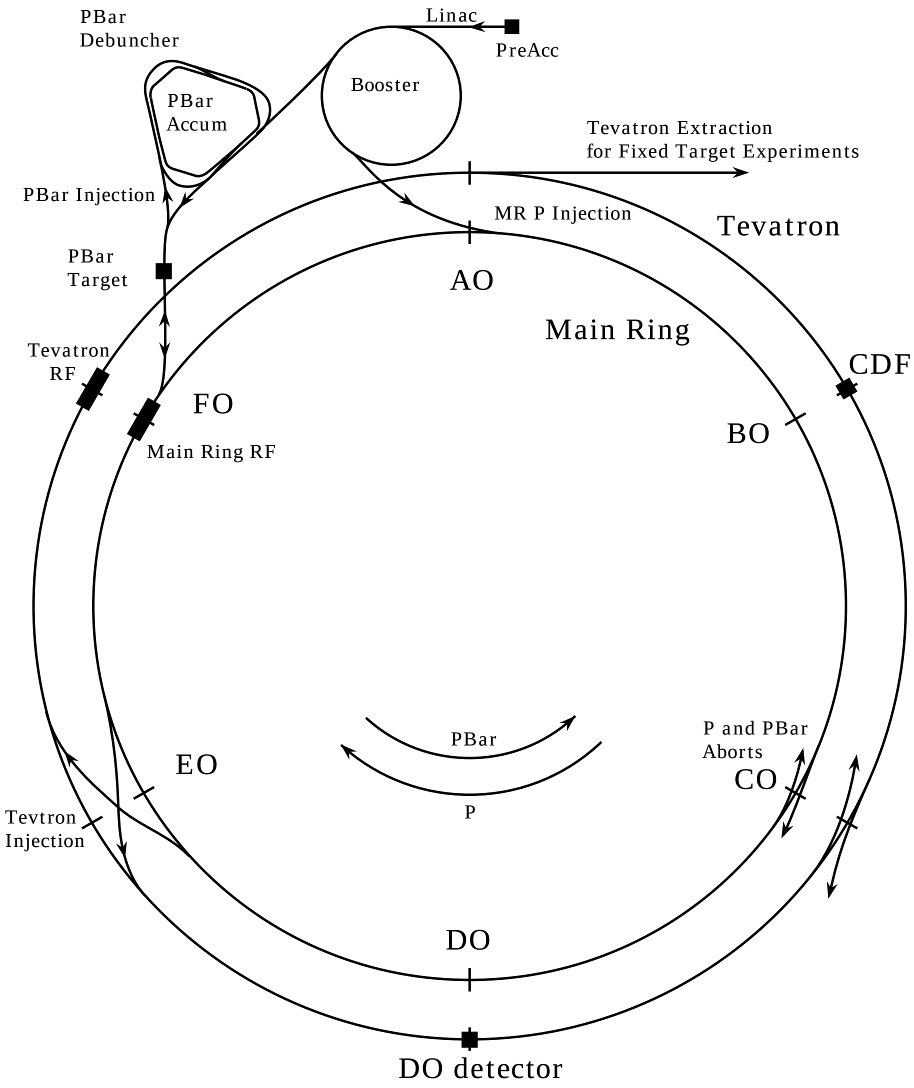

Figure 2.1: The Fermilab accelerators (not to scale). For clarity, the Tevatron is drawn as outside of the Main Ring.

upgrade increased the beam energy to 400 MeV [20].

The remaining accelerators are all synchrotrons. In these circular accelerators, magnetic fields steer the charged particles in closed orbits, while RF fields at certain points around the ring accelerate them. By increasing the magnetic field strength synchronously with the increasing particle energy, synchrotrons are able to keep the particles in orbit throughout the acceleration cycle. The maximum energy of a synchrotron is limited by its radius and maximum magnetic field [22].

At Fermilab, protons from the Linac are injected into the Booster [20], which is a synchrotron 151 meters in diameter. Here, the protons are accelerated to an energy of 8 GeV in a process that takes about 33 milliseconds.

At the end of the Booster cycle, the protons are transferred to the Main Ring [20], a synchrotron that is 2000 meters in diameter. Until 1983, the Main Ring was Fermilab's most powerful accelerator, delivering proton beams with a maximum energy of 400 GeV to an array of fixed-target experiments [21]. Now the Main Ring is used for the production of antiprotons and as an injector for the Tevatron.

The Tevatron, which shares the tunnel with the Main Ring, is also a synchrotron. Its beam pipe is located about 2 feet below the Main Ring beam pipe. Special overpasses for the Main Ring have been placed at the BØ and DØ interaction regions to allow space for the detectors. Unfortunately, the height of the overpass at DØ is only 89 inches, so the Main Ring passes through the outer sections of the DØ calorimeters. The consequences of this will be discussed below.

While the Tevatron is no larger than the Main Ring, its magnets have superconducting coils cooled to liquid helium temperature [24]. These magnets generate much larger fields than the conventional magnets used in the Main Ring, so that beams with higher energies can be contained in the Tevatron orbit. At present, the standard operating energy is 900 GeV.

The Tevatron can be used as a source of high-energy proton beams for fixed-target experiments. In this mode, protons are accelerated, then extracted as indicated in Fig. 2.1. It can also be used as a proton-antiproton collider. Because protons and antiprotons have the same mass but opposite charge, only one set of magnets and RF cavities is needed to steer and accelerate the two counter-rotating beams.

2.1.2 Antiproton Production and Storage

Antiprotons for the Tevatron collider are created by directing a 120-GeV beam of protons from the Main Ring onto a nickel or copper target disk. For every 10^{12} protons that strike the target, about 10^7 antiprotons are produced [20]. They pass through a cylindrical piece of lithium in which a large electric current produces a focusing magnetic field that collimates the beam of outgoing particles.

Next, a spectrometer magnet selects antiprotons with an energy of 8 GeV. These antiprotons enter the Debuncher [20], which is, roughly speaking, a triangular storage ring. Here, the antiprotons are steered in closed orbits that have three straight sections. RF fields are applied to reduce the momentum spread of the beam, which increases the beam's temporal spread. At the same time, the transverse dimension of the antiproton beam is reduced through "stochastic cooling" [20]. The antiprotons are then transferred to the Accumulator, a somewhat smaller storage ring that shares the tunnel with the Debuncher, and merged with the existing stack. The debunching and cooling procedures continue in the Accumulator.

2.1.3 Collider Operation

In its collider mode, the Tevatron is operated as a storage ring, in which beams are accelerated to their maximum energy, then allowed to continue to circulate and collide for many hours before they are removed and the process started over again [22].

In preparation for a "store" [20], protons are injected into the Main Ring, accelerated to 150 GeV, and transferred to the Tevatron. Six bunches, each of which contains typically 120×10^9 ("Run Ia") to 230×10^9 ("Run Ib") protons, are injected into the Tevatron in this way. Then a fraction of the antiprotons are transferred from the stack in the Accumulator to a counterclockwise orbit in the Main Ring. Like the protons, the antiprotons are accelerated to 150 GeV and transferred to the Tevatron. Six antiproton bunches, each of which typically contains 30×10^9 (Run Ia) to 55×10^9 (Run Ib) particles, are injected. After all the bunches have been injected, they are accelerated to 900 GeV. Then focusing magnets are used to minimize the transverse size of the beams at the centers of the DØ and CDF detectors and to bring the two beams into collision. Electrostatic separators are used to increase beam lifetimes by reducing the rate of interactions at other points in the ring. The beams continue to circulate and collide for up to 20 hours, while stacking operations continue in the Main Ring and in the antiproton source, replenishing the supply of antiprotons in preparation for the next store.

2.1.4 Luminosity

The interaction rate in a collider experiment depends on the intensity of the beams. We measure the instantaneous "luminosty" ($\mathcal{L}$) of colliding beams by measuring the interaction rate (R) for a process whose cross section (σ) is well known. $\mathcal{L}$ can be determined from the defining relation $R = \sigma\mathcal{L}$. The total number of interactions observed is just the time integral of R, which is proportional to $\int \mathcal{L} dt$. This quantity, the time-integrated luminosity, is the standard measure of the amount of data recorded by a colliding-beam experiment. It is reported in events per unit cross section, often denoted just by pb^{-1} (*e.g.*, 10 events per picobarn of cross section is usually cited as 10 pb^{-1}) [22].

DØ collected data during two running periods of the Tevatron: Run Ia, which lasted from May, 1992, to May, 1993, and Run Ib, which began in December, 1993, and ended in July, 1995. For Run Ia, the data correspond to an integrated luminosity of about 13 pb^{-1}, and for Run Ib, to about 80 pb^{-1}. All of the data from Run Ia and the first 45.3 pb^{-1} of the data from Run Ib will be used in this search.

2.2 The DØ Detector

The DØ detector, shown in Fig. 2.2, consists of three major subsystems: the inner tracking system, made of drift chambers and a transition radiation detector; the uranium/liquid-argon calorimeters; and a muon tracking system surrounding the calorimeters. The detector is described in detail in Ref. [25].

The DØ detector was designed to be a general-purpose tool for the study of $p\overline{p}$ collisions at $\sqrt{s} = 1.8$ TeV, with a view toward testing the Standard Model and searching for new phenomena. The physics goals that motivated the design of DØ included precision measurements of the mass and width of the W boson, and of the production and decays of W and Z bosons; studies of jet cross sections and other jet production characteristics, and measurement of the coupling constant of QCD (α_S); discovery and measurement of the mass and decay properties of the top quark; and searches for evidence of new physics, including supersymmetry, technicolor, and quark or lepton compositeness [26]. In all of these studies, the important signals correspond to production of jets, charged leptons, and neutrinos. Therefore, DØ was designed to detect and measure the energies of jets, electrons, and muons with good resolution, and to determine the missing transverse energy (see Sec. 2.2.1)

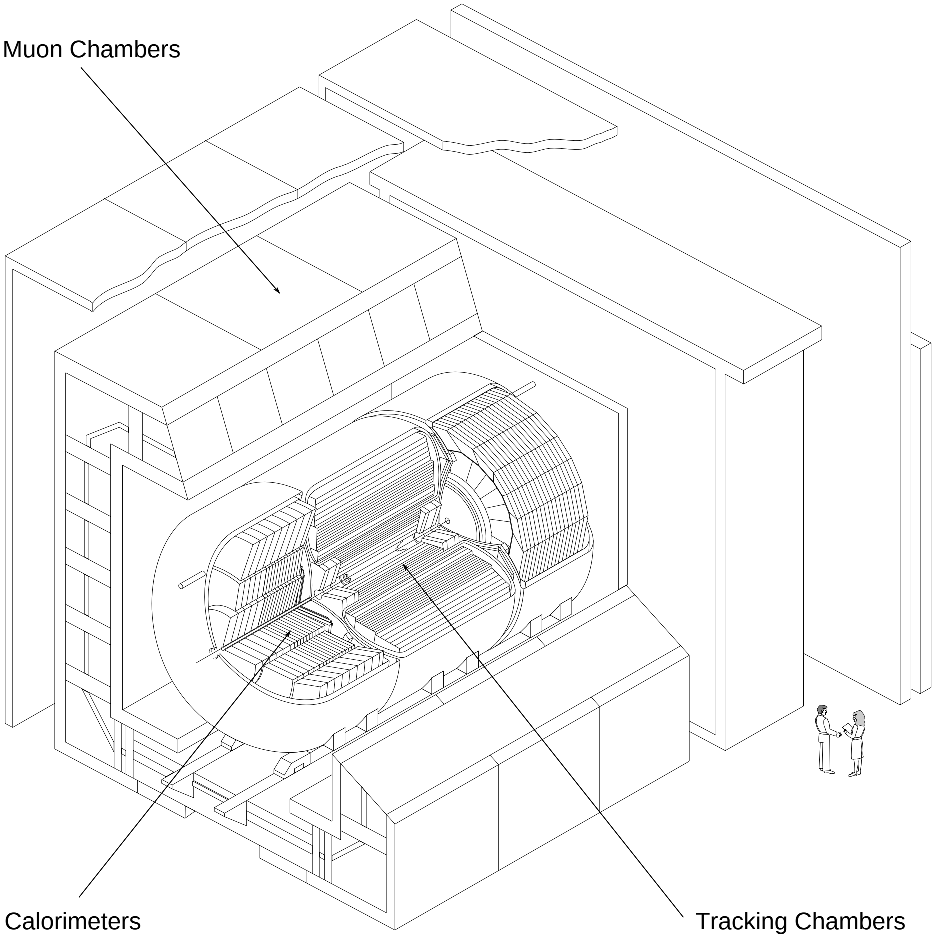

Figure 2.2: The DØ detector.

in events, from which the presence of neutrinos can be inferred. Consequently, the design emphasizes good calorimetry over most of the 4π solid angle, electron identification and separation from a background of pions and photons, and muon detection.

Many general-purpose collider detectors use a solenoid to produce a magnetic field in the central tracking volume in order to measure the momenta of charged particles [12]. DØ has no magnetic field in the central region. This design choice makes it possible to have a compact calorimeter that covers the maximum solid angle, unobstructed by the coils or supports of a magnet. It was expected that, for high energies, the resolution from the calorimetry would be better than the momentum resolution achievable using a reasonable (several tesla) magnetic field. Furthermore, the ability to detect and measure jets with large transverse energy is enhanced by the absence of a field, which causes the paths of the charged components to diverge from the production axis of the jet [26, 27].

The DØ detector rests on a support platform that provides space for much of the front-end electronics and for services for the power, gas, and cryogenic systems [25]. The platform is moveable so that the detector can be rolled in and out of the position of the beam. An articulating bridge carries the cables from the detector elements to a moveable counting house, which travels with the detector platform in order to minimize the lengths of the cables. This counting house contains the digitizing electronics for the detector signals and the electronics for the Level 1 trigger system. It is far enough from the beam path that it can be accessed during data taking.

2.2.1 Coordinate System and Definitions

We define the standard DØ coordinate system [25] as a right-handed coordinate system, with origin at the center of the detector. The z axis is along the direction of the proton beam, and the positive y axis points upward. It is often convenient to use cylindrical or spherical polar coordinates, with the azimuthal (ϕ) and polar (θ) angles defined in the standard way: ϕ is zero along the positive x axis and $\pi/2$ along the positive y axis, while θ is zero along the positive z axis.

A useful variable is the rapidity, $y \equiv \frac{1}{2} \ln \frac{E+p_z}{E-p_z}$. A Lorentz boost in the z direction changes y by an additive constant [7, 28]. When $E \gg m$, y can be approximated by the pseudorapidity $\eta \equiv -\ln(\tan \frac{\theta}{2})$. Because of its Lorentz transformation properties, η is often used instead of the polar angle θ.

Two other useful variables are the transverse momentum, $p_T \equiv \sqrt{p_x^2 + p_y^2}$, and the transverse energy, $E_T \equiv \sqrt{E^2 - p_z^2}$. Both of these are invariant under boosts in the z direction. When $E \gg m$, we can approximate $E_T = p_T = E \sin \theta$.

In $p\overline{p}$ collisions, the interacting partons have negligible transverse momenta, and therefore the total p_T in the final state should be approximately zero. We define the "missing" p_T as the p_T vector that would make the final momenta sum to zero in the transverse plane. This vector can be associated with any non-interacting neutrino, and because $m_\nu \approx 0$, it is more commonly called the missing E_T, or $\not{E}_T$.

2.2.2 Tracking of Charged Particles

The central tracking system is shown in Fig. 2.3. In the central region ($45^\circ < \theta < 135^\circ$), charged particles are tracked using an inner Vertex Drift Chamber, followed by a transition radiation detector and central drift chambers. Forward drift chambers, in the plane perpendicular to the beam pipe, extend coverage to $\theta \approx 5^\circ$.

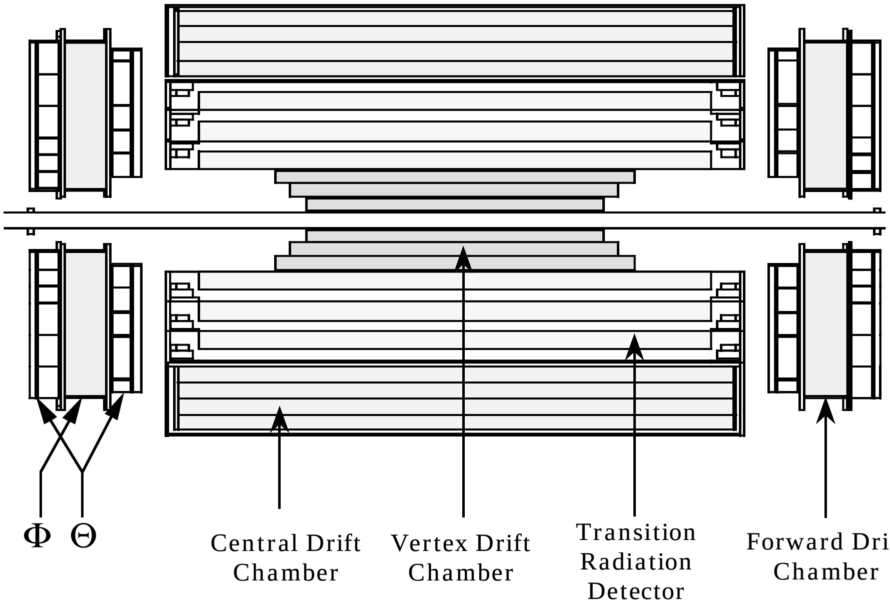

Figure 2.3: Central tracking chambers viewed in the r-z plane. The interaction point is in the center of the figure.

The central tracking system relies on use of drift chambers. Before describing the DØ tracking chambers in detail, we will review the principles of drift chamber operation.

Drift Chamber Principles

When a charged particle with sufficient energy passes through matter, it can ionize atoms along its trajectory. A drift cell consists of a gas-filled volume that serves as an ionizing medium for passing charged particles. A uniform electric field is applied to most of the sensitive region so that the ionization electrons drift at constant velocity toward the positive electrode, which is typically a thin wire oriented transversely to the particle's trajectory and held at high voltage. Very near this electrode, the electric field becomes so intense that the ionization electrons acquire enough energy to create more electron-ion pairs, thereby producing an avalanche.

This fast negative charge is collected on the anode wire and detected as a current pulse. Ignoring the brief time of the avalanche, the time of arrival of this signal can be compared to an appropriate reference time to determine the distance of the original charged particle from the wire [29].

Drift chambers consist of planes of drift cells with their sense wires aligned relative to one another. These anode planes can be separated by cathode foils or by planes of cathode wires. Additional wires are usually needed in these chambers to maintain the desired degree of uniformity of the field throughout the drift region [29].

A drift chamber provides position information in one direction. To determine the position in the other direction, there are several possibilities. A second chamber may be used, with its sense wires rotated by some angle relative to the first. This is not always practical given the available detector volume, so other techniques are sometimes used. Many of these involve image charges or the response of the positive ions produced in the gas [29]. The DØ drift chambers employ several techniques for measuring the longitudinal coordinate. These will be described below for each detector.

Vertex Drift Chamber

The Vertex Drift Chamber (VTX) [25, 30, 31, 32] consists of a set of three layers of axial drift chambers. The innermost chamber is divided into 16 azimuthal sectors; the other two are divided into 32 sectors each. As shown in Fig. 2.4, each layer is offset in ϕ from the previous layer in order to improve the position resolution. Each sector has eight sense wires spaced radially. Adjacent sense wires are offset by ± 100 μm to resolve the left-right ambiguity within each cell.

In the original design of the VTX, track coordinates along the beam direction

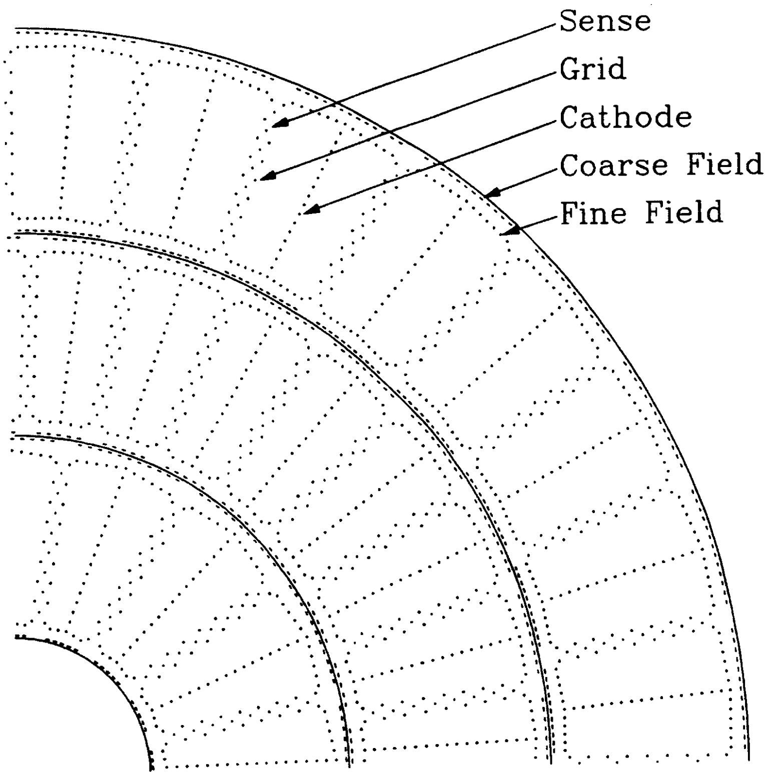

Figure 2.4: End view of the Vertex Drift Chamber, showing the cell structure.

were to be determined using helical cathode pads [33]. Unfortunately, this system could not be made to work, and instead, coordinates along the beam direction are determined using charge division, which exploits the resistivity of the readout wire. Both ends of each sense wire are read out, and the ratio of charges is used to determine the z coordinate. This technique works well if the cell occupancy is small; however, this is not the case for interactions at the Tevatron. Consequently, the VTX has poor resolution (1.5 cm) in z.

The drift gas, a mixture of CO_2 and ethane, was chosen because it provides optimal spatial resolution and ability to distinguish two tracks which are close together. The chamber has a resolution of approximately 50 μm in the transverse drift direction [25].

Other parameters for the VTX chamber are given in Table 2.1.

Transition Radiation Detector

Outside of the Vertex Drift Chamber is the Transition Radiation Detector (TRD), designed to distinguish electrons from pions. This device exploits the fact that highly relativistic particles ($\gamma > 10^3$, where $\gamma = E/m$ is the Lorentz factor) emit X-rays when they cross a boundary between two materials with different dielectric constants [35, 36]. The intensity of these X-rays is sharply peaked in the forward direction (at an angle $\theta \sim 1/\gamma$) and proportional to γ [37]. Electrons of a given energy will have much larger γ than pions of the same energy, and the difference in transition radiation produced in a suitable stack of foils can be used to distinguish the two. Other more massive particles produce essentially no X-rays at these transitions.

The TRD at DØ [25, 38, 39] has three layers. Each layer consists of a section in which X-rays are produced, followed by a radial drift chamber in which they

Table 2.1: Parameters of the Vertex Drift Chamber [25, 33, 34].

Active length	90.6 cm, 106.6 cm, 116.8 cm
Inner radius	3.7 cm
Outer radius	16.2 cm
Number of layers	3
Number of cells per layer	16, 32, 32
Number of sense wires per cell	8
Sense wire separation	4.57 mm (r), with 100 μm stagger (ϕ)
Total number of sense wires	640
z coord. measurement	Charge division
Sense wire composition	25-μm NiCoTin, 80 g tension
Sense wire voltage	+2.5 kV
Field wire composition	152-μm Au-plated Al, 360 g tension
Average drift field	$\sim$ 1 kV/cm
Gas used	CO_2 (95%) + ethane (5%) + H_2O
Pressure	1 atm
Drift velocity	7.3 μm/ns
Maximum drift distance	1.6 cm
Gas gain at sense wire	4×10^4
Resolution	$\approx$ 50 μm (r-ϕ plane), 1.5 cm (z)

are detected. Each radiator section consists of a stack of 393 polypropylene foils in a volume filled with nitrogen gas. The foils are 18 μm thick, and the gaps are typically 150 μm. X-rays are produced at each interface.

The X-rays are detected at the end of each stack of foils using a xenon/methane-filled drift chamber with a radial electric field. The X-rays liberate atomic electrons in the first section of the drift chamber. These can ionize further and drift radially outward to the amplification stage, where they are detected using sense wires parallel to the beam axis. The first two layers of the TRD have 256 sense wires each, spaced uniformly in ϕ; the third layer has 512 sense wires, but these are read out in pairs. In each layer, the cathode is segmented into 256 helical strips that are read out and used to determine the z coordinate of each energy cluster.

The total energy observed in a cluster reflects whether the source is an electron or a hadron. However, it is more useful to consider a likelihood function for the distribution of deposited energy among the three layers of the TRD. Using such a function, the TRD achieves 50:1 electron to pion rejection, for 90% electron identification efficiency [25].

Central Drift Chamber

The Central Drift Chamber (CDC) [25, 31, 40, 41, 42] surrounds the TRD. It is made of drift cells arranged in a series of four radial layers, each of which is segmented into 32 azimuthal cells. Three of these cells are shown in Fig. 2.5. Each cell has seven sense wires spaced radially, with adjacent wires staggered in ϕ by ± 200 μm to eliminate the left-right ambiguity within the cell. To provide increased azimuthal position resolution and ability to distinguish two nearby tracks, each layer is offset by half of the azimuthal angle subtended by each cell.

Delay lines are used to determine the axial coordinates of the tracks. These are

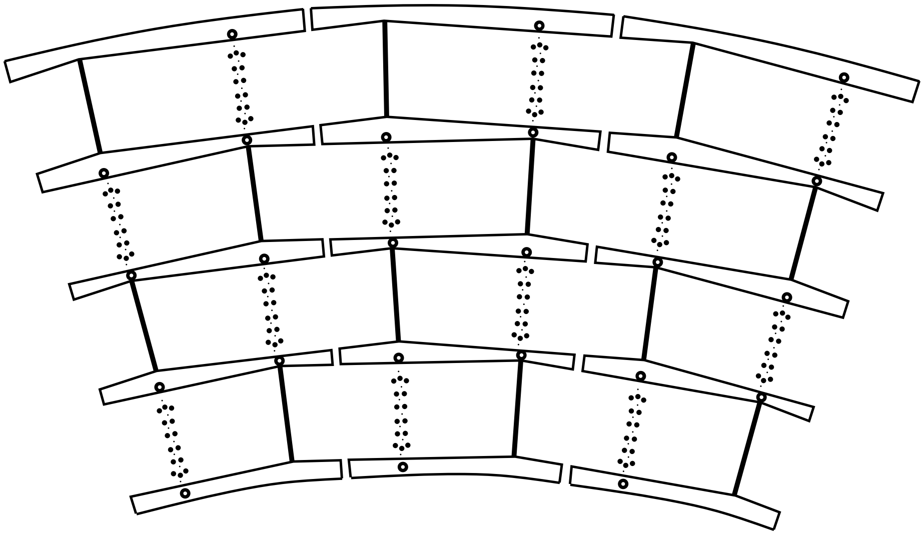

Figure 2.5: End view of the Central Drift Chamber, showing the modular geometry. Three of 32 cells are shown in the figure.

coils wound on carbon fiber epoxy cylinders that are embedded in the inner and outer cell walls and aligned with the sense wires. The nearest sense wires induce signals on the delay lines, which are read out at both ends. The difference between arrival times of signals at the two ends yields a determination of the z coordinate.

Several parameters characterizing the CDC are given in Table 2.2. Under the described operating conditions, the resolution of the CDC is about 150 μm in the drift direction, and 3.5 mm along the beam direction [25].

Forward Drift Chambers

Vertex chambers and TRDs are not used in the forward and backward regions because they offer little benefit in exchange for degradation they produce in calorimetric coverage. Here, tracking information is provided by Forward Drift Chambers (FDC) [25, 31, 43, 44] oriented in the plane perpendicular to the beam axis and configured to measure the polar angle (θ) and azimuth (ϕ) of tracks.

Table 2.2: Parameters of the Central Drift Chamber [25, 33, 34].

Active length	179.4 cm
Inner radius	51.8 cm
Outer radius	71.9 cm
Number of layers	4
Number of sectors per layer	32
Number of sense wires per cell	7
Sense wire separation	6.0 mm (r), with 200 μm stagger (ϕ)
Total number of sense wires	896
z coord. measurement	Delay lines
Number of delay lines	256 (2 per cell)
Sense wire composition	30-μm Au-plated W, 110 g tension
Sense wire voltage	+ 1.5 kV (inner) – +1.5 kV (outer)
Field wire composition	125-μm Au-plated CuBe, 670 g tension
Average drift field	620 V/cm
Gas used	Ar(92.5%)-CH_4(4%)-CO_2(3%) + H_2O(0.5%)
Pressure	1 atm
Drift velocity	34 μm/ns
Maximum drift distance	7 cm
Gas gain at sense wire	2 (inner) –6 (outer) $\times 10^4$
Resolution	150 μm (r-ϕ plane), 3.5 mm (z)

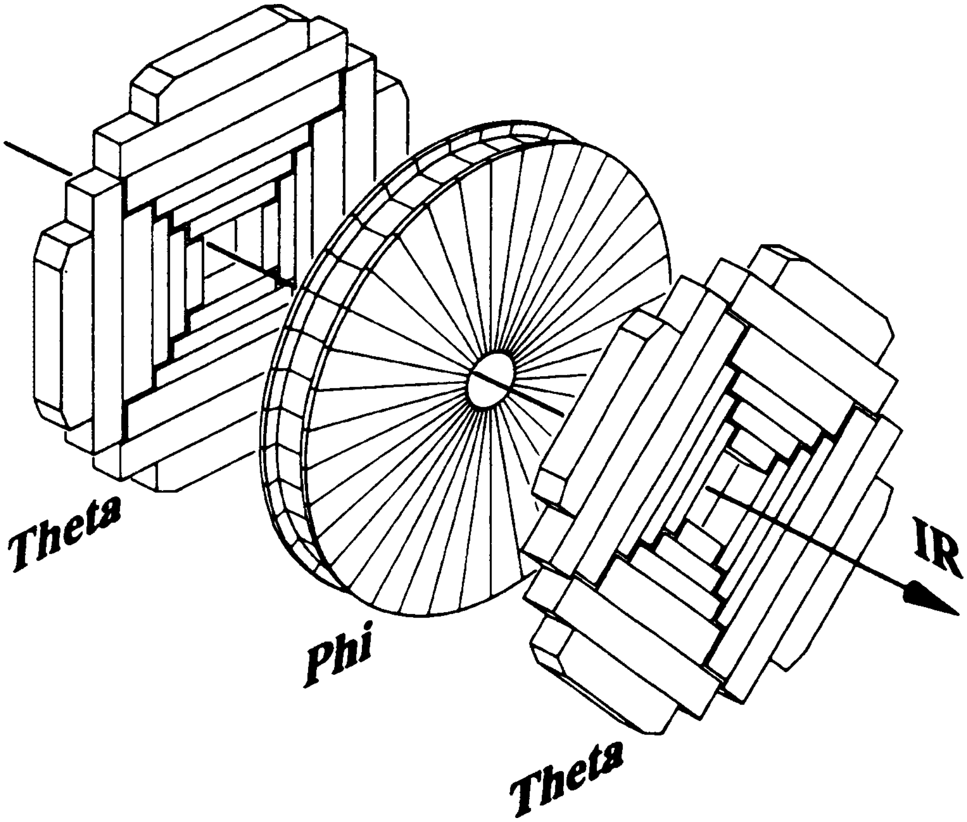

Figure 2.6: Exploded view of one set of Forward Drift Chambers.

Each FDC consists of two Θ modules with wires oriented transversely to the beam to measure θ, and one Φ module with wires running radially outward from the beam pipe to measure ϕ. An exploded view of one set of these chambers is shown in Fig. 2.6, indicating the cell structure of each chamber.

Each Θ module is made of four identical sectors. In each sector, there are six drift cells at different distances from the beam pipe. Each cell has eight sense wires along z. Like the wires in the CDC, these are staggered to remove the left-right ambiguity within the cells. Each cell also has one delay line, similar to the CDC delay lines. The two Θ modules are rotated by 45° in ϕ with respect to each other, in order to provide optimal resolution.

The Φ module has 36 azimuthal sectors. Each sector is a drift cell with 16 radial sense wires spaced along z. Once again, successive wires are staggered to remove the left-right ambiguity within the cell.

Table 2.3 lists several parameters for the FDC. The overall resolution in this region is 200–300 μm.

2.2.3 Calorimeters

The calorimeters, shown in Fig. 2.7, provide the only means of measuring the energies of electrons, photons, and jets. The calorimeters use liquid argon as the active medium, and must therefore be housed in cryostats. Three cryostats—one central and two endcaps—are used in order to allow access to the central tracking chambers, as shown in Fig. 2.7. In both the central and endcap regions, the calorimeter is divided into three longitudinal sections: electromagnetic, fine hadronic, and coarse hadronic. To minimize effects from uninstrumented material located between the cryostats, special devices have been designed to measure energy in the inter-cryostat region. Before describing the calorimeters in more detail, we will review the basic principles of calorimetry as applied in high-energy physics.

Principles of Calorimetry

A calorimeter is any instrument designed to measure the energy of an elementary particle by transforming that energy into a measurable quantity through the particle's interactions with matter [45]. Different particles interact differently, but, except for high-energy muons, the particle energies can be measured with a suitable calorimeter.

High-energy electrons interact with matter primarily through bremsstrahlung, in which the electron radiates photons. When these secondary photons have enough

Table 2.3: Parameters of the Forward Drift Chambers [25, 33, 34].

	Θ	Φ
z interval	104.8–111.2 cm 128.8–135.2 cm	113.0–127.0 cm
Inner radius	11 cm	11 cm
Outer radius	62 cm	61.3 cm
Number of cells per layer	4 quadrants, 6 cells each	36
Number of sense wires per cell	8	16
Sense wire separation	8 mm (z), 200 μm stagger	
Total number of sense wires	384/FDC	576/FDC
Long. coordinate measurement	Delay lines	
Number of delay lines	48/FDC (1 per cell)	
Sense wire composition	30-μm Au-plated W, 50–100 g tension	
Sense wire voltage	+1.55 kV	+1.66 kV
Field wire composition	163-μm Au-plated Al, 100–150 g tension	
Average drift field	1.0 kV/cm	1.0 kV/cm
Gas used	Ar(92.5%)-CH_4(4%)-CO_2(3%) + H_2O(0.5%)	
Pressure	1 atm	1 atm
Drift velocity	37 μm/ns	40 μm/ns
Maximum drift distance	5.3 cm	5.3 cm
Gas gain	2.3–5.3 $\times 10^4$	3.6 $\times 10^4$
Resolution (drift direction)	300 μm	200 μm

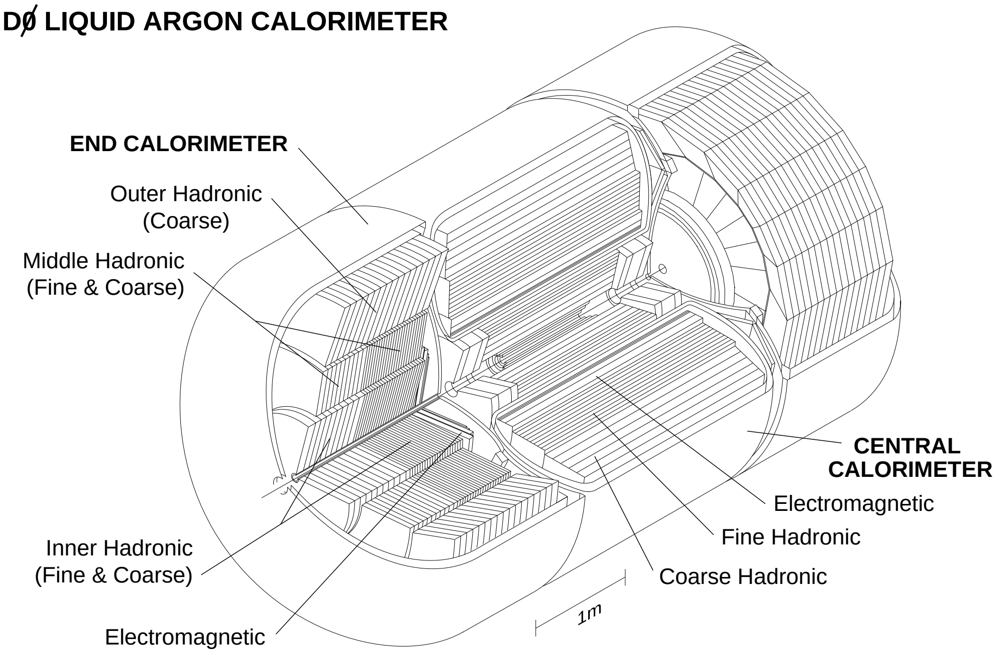

Figure 2.7: Cutaway view of the calorimeters.

energy, they produce electron-positron pairs, which in turn can radiate more photons. These processes produce a shower of electromagnetically interacting particles. When the initial particle is a photon, a similar shower will be generated, beginning with pair production by the incident photon. The secondary particles can interact via the photo-electric effect, Compton scatter, or simply ionize the intervening material. The shower continues to develop and deposit energy until the remaining particles have too little energy to produce new electron-positron pairs, at which point the remaining energy is deposited via ionization in the material [22, 46].

For any absorber, the energy loss in a length Δx through electromagnetic processes can be characterized as $\Delta E = -E\Delta x/X_0$, where X_0 is the radiation length of the absorber. The radiation length can be approximated (in units of g/cm^2) by $X_0 \simeq 180A/Z^2$, where Z is the mean atomic number and A is the mean number of nucleons [22, 46].

The summed length of all the charged-particle tracks in an electromagnetic shower is found to be essentially proportional to the energy of the incident particle. One can therefore obtain a crude measurement of the incident particle's energy by counting the number of particles produced in the shower. A more precise measurement can be made by measuring the ionization energy deposited in the absorber medium, which is proportional to the summed charged-track length [22].

Hadrons induce similar showers in matter, but only a part of their energy is deposited in the form of electromagnetic interactions. This is because hadrons can interact with atomic nuclei, and up to 40% of the incident hadron's energy can be expended in releasing nucleons from their bound state. In addition, hadronic showers can produce secondaries such as pions, kaons, or charm particles that decay to muons and neutrinos that escape the calorimeter. As opposed to electromagnetic interactions, energy loss in such processes cannot be measured precisely for individual hadrons because the fraction of energy lost in hadronic interactions is subject to large fluctuations in the mix of secondary kinds of collisions and types of produced particles. Consequently, the energy resolution for hadrons is degraded relative to that for electromagnetically interacting particles [45]. The electromagnetic vs. hadronic response of a calorimeter can be characterized by measuring the response to electrons and to pions of known energies. When the ratio (e/π) of the responses is close to unity, the calorimeter is less sensitive to fluctuations in hadronic showers, and hadronic energy resolution becomes optimal [45].

Energy loss in a hadronic shower is characterized by the nuclear absorption length (λ_A), which reflects the hadron-nuclear interaction cross section and varies for different materials approximately as $A^{1/3}$ [46]. A good calorimeter must have a sufficient thickness of absorber to contain the full shower. Otherwise, energy will escape unmeasured, leading to large fluctuations in energy deposition and poor resolution. Containing an electromagnetic shower requires about 20 radiation lengths (X_0) of material; containing hadronic showers requires 5-10 absorption lengths (λ_A), depending on the energy of the hadron [22]. For most materials, λ_A and X_0 are quite different. For instance, uranium has $X_0 \approx 0.32$ cm and $\lambda_A \approx 10.5$ cm, while for beryllium the two are comparable ($X_0 \sim \lambda_A \sim 35$ cm) [7]. As a result, electromagnetic showers in uranium will end well before hadronic showers reach their maximum. This property is useful in distinguishing between electromagnetically interacting particles and hadrons.

Obviously, a calorimeter must be able to measure the produced ionization. One technique is to choose an absorber material that also provides a detectable signal. Such calorimeters are called "homogeneous." NaI crystals, lead-glass, and scintillators are commonly used absorbers for homogeneous calorimeters. These calorimeters provide high resolution; however, their long interaction lengths make them impractical for use as hadronic calorimeters in high-energy collider experiments [46].

The alternative is to use a "sampling" calorimeter. These devices consist of layers of a dense, inactive absorber sandwiched between layers of active material. The shower is sampled as it passes through the active layers by measuring the ionization produced in that region. Much of the energy is lost in the absorber layers, but the energy of the incident particle can be determined because it is essentially proportional to the amount deposited in the active region [45].

The resolution of a calorimeter is inherently limited by fluctuations in the number of charged particles in a shower. The significance of these fluctuations decreases as the energy of the incident particle increases, which means that the energy resolution of a calorimeter improves with increasing energy. Sampling calorimeters are subject to additional fluctuations due to the fact that only a fraction of the incident particle's energy is measured [46]. This is a particularly important concern when the e/π response is not close to unity.

However, for a sampling calorimeter, it is possible to improve the e/π ratio by choosing an absorber (or active material) that compensates for the unmeasured hadronic energy. For instance, the hadronic energy response may be increased by using depleted uranium (^{238}U) as the absorber. Slow neutrons will induce fission in some of the uranium nuclei, yielding additional energy in the form of soft photons and MeV neutrons. The effect is to increase the measurable component of the hadronic shower [45]. This compensation can reduce e/π nearly to unity and thereby improve the hadronic energy resolution. Nevertheless, the resolution is still not as good as for electromagnetic showers [45, 47]. For the above reasons, depleted uranium is the absorber in most of the DØ calorimetry. In fact, it is used in all but the coarse hadronic sections, where, for financial and mechanical reasons, stainless steel or copper is employed.

Calorimeter Cells

The DØ calorimeters [25, 48, 49, 50, 51] consist of plates of absorber material alternating with active regions, as shown schematically in Fig. 2.8. The active regions are spaces filled with liquid argon, which is ionized by the passage of the charged particles in a shower. In the center of each argon gap is a signal board. The absorber plates are grounded, and a high voltage is applied to the resistive coats on the signal board. Any ionization charge in the gap flows toward the signal board, where it induces an image charge on the inner conductor (pads) that can be read out. To reduce the number of readout channels, several cells at successive longitudinal depths are ganged together and read out as one. The DØ calorimetry is read out in four longitudinal electromagnetic and three hadronic layers.

The signal boards are segmented into readout pads of $\Delta\eta = 0.1$, $\Delta\phi = 2\pi/64 \approx 0.1$, with the exception of the third electromagnetic layer in both the central and

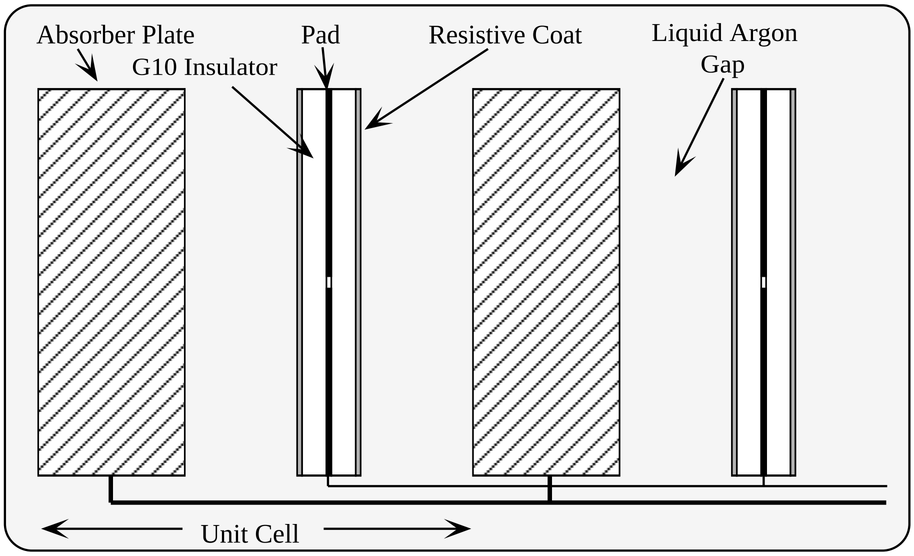

Figure 2.8: Sketch of a unit cell in the calorimeter.

end calorimeters, which have a segmentation of $\Delta\eta = 0.05$, $\Delta\phi = 2\pi/128 \approx 0.05$ to allow finer transverse sampling near the electromagnetic shower maximum. Also, the region in the endcaps for $|\eta| > 3.2$ employs larger pad sizes because the spatial segmentation is far smaller than warranted by the typical transverse size of a shower. The centroids of successive longitudinal cells form projective towers in η-ϕ. This tower structure is shown for one quadrant of the calorimeter in Fig. 2.9.

Performance of the calorimeters was studied extensively in a test beam using particles of a wide range of energies. The energy resolution for electrons and photons is $\sigma/E \approx 16\%/\sqrt{E} \oplus 0.4\%$, where E is measured in GeV and the symbol $\oplus$ indicates addition in quadrature. For individual hadrons, the resolution is $50\%/\sqrt{E} \oplus 3\%$ [52].

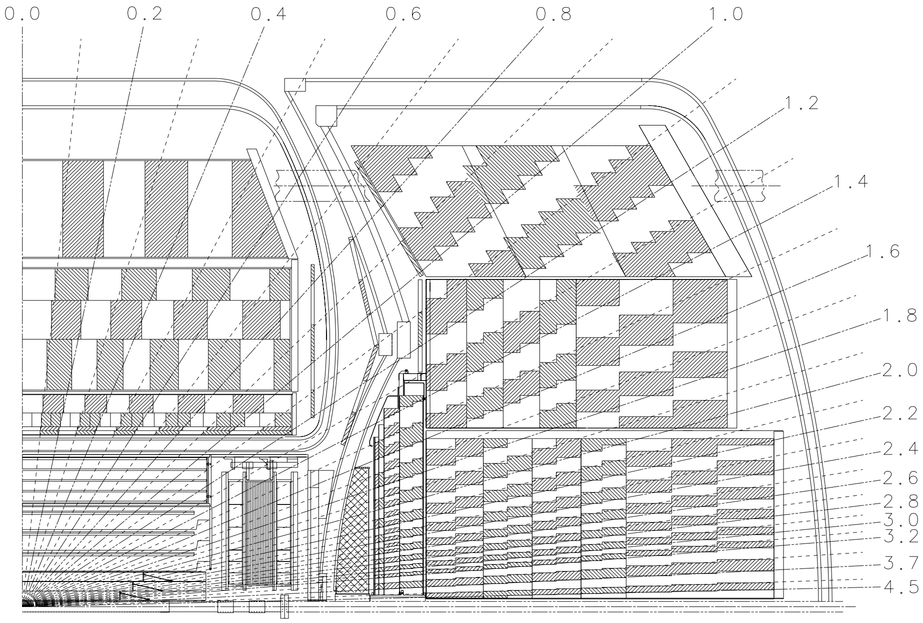

Figure 2.9: Calorimeter quadrant, showing the transverse and longitudinal segmentation. The shading indicates cells that comprise the pseudoprojective readout towers.

Central Calorimeter

The Central Calorimeter (CC), which provides coverage for $|\eta|$ up to about 1.0, surrounds the central tracking system. As Fig. 2.7 indicates, it is divided into electromagnetic, fine hadronic, and coarse hadronic sections. The electromagnetic section uses depleted-uranium absorber with plate thickness of 3 mm. The plates in the fine hadronic section are made of uranium-niobium (2%) alloy and are 6 mm thick. The coarse hadronic section, intended to detect energy leakage, has copper plates that are 46.5 mm thick.

The calorimeter construction is modular, with 32 azimuthal electromagnetic modules positioned in a ring around the drift chambers, followed by 16 azimuthal fine-hadronic modules and finally, 16 azimuthal coarse-hadronic modules. Each module is constructed in the shape of a cylindrical wedge running the full length of the CC volume. This minimizes gaps in the calorimetric coverage. The successive layers of modules are offset in ϕ so that no outgoing particle encounters more than one intermodular gap. There is a hole in one of the coarse hadronic modules at the top of the CC to allow passage of the Main Ring beam pipe.

Several parameters for the Central Calorimeter are summarized in Table 2.4. (The sampling fraction refers to the mean percentage of deposited energy that is sampled by the active medium.)

End Calorimeters

The End Calorimeters (EC) extend the coverage to $|\eta| \approx 4$. As in the CC, the absorbers in the electromagnetic and the fine hadronic modules are, respectively, depleted uranium and uranium-niobium alloy. The absorber in the coarse hadronic modules is stainless steel.

Each EC has one electromagnetic module (ECEM), followed by one fine (IFH)

Table 2.4: Parameters of the Central Calorimeter [25, 33, 34].

	EM	FH	CH
$\|\eta\|$ range	0–1.2	0–1.0	0–0.6
Absorber	U	U-Nb	Cu
Absorber thickness (mm)	3	6	46.5
LAr gap width (mm)	2.3	2.3	2.3
Number of modules	32	16	16
Number of cells per module	21	50	9
Cells per readout layer	2,2,7,10	20,16,14	9
Total readout cells	10,368	3000	1224
Total radiation lengths (X_0)	20.5	96.0	32.9
Total absorption lengths (λ_A)	0.76	3.2	3.2
Sampling fraction (%)	11.79	6.79	1.45

and one coarse (ICH) hadronic module, which form the inner ring. These modules are cylindrical, with a hole in the center for the beam pipe. There are no through-going cracks in the absorber plates. Sixteen more fine hadronic modules (MFH), each followed by a coarse hadronic module (MCH), form a ring around the inner hadronic section. Outside this ring is another ring, consisting of 16 coarse hadronic (OCH) modules. The OCH plates are positioned at an angle of 60° to the beam axis, as shown in Fig. 2.9, to preserve near-normal particle incidence. As in the central calorimeter, the OCH modules are rotated in ϕ with respect to the MFH and MCH modules to eliminate projective cracks. One of the OCH modules has a hole to allow passage of the Main Ring beam pipe.

Parameters for these modules are summarized in Table 2.5.

Table 2.5: Parameters of the End Calorimeters [25, 33, 34].

	EM	IFH	ICH	MFH	MCH	OH
$\lvert\eta\rvert$ range	1.3–3.7	1.6–4.5	2.0–4.5	1.0–1.7	1.3–1.9	0.7–1.4
Absorber	U	U-Nb	SS	U-Nb	SS	SS
Abs. thickness (mm)	4	6	6	6	46.5	46.5
LAr gap width (mm)	2.3	2.1	2.1	2.2	2.2	2.2
Number of modules	1	1	1	16	16	16
Cells per module	18	64	12	60	14	24
Cells/readout layer	2,2,6,8	16	14	15	12	8
Total readout cells	7488	4288	928	1472	384 + 64 + 896	
Total X_0	20.5	121.8	32.8	115.5	37.9	65.1
Total λ_A	0.95	4.9	3.6	4.0	4.1	7.0
Sampling fract. (%)	11.9	5.7	1.5	6.7	1.6	1.6

Inter-Cryostat Region

The regions between the CC and EC contain substantial amounts of uninstrumented material, such as the cryostat walls, in which energy can be lost, leading to poor resolution in jet energy and missing transverse energy ($\not\!\!E_T$). To compensate for this, energy is sampled in the space between the cryostats by an Intercryostat Detector (ICD), which covers the region $0.7 < |\eta| < 1.4$. Each ICD consists of a set of scintillator tiles, segmented in η and ϕ to match the calorimeters. The scintillator light is piped via wave-shifting fibers to photomultiplier tubes mounted behind the scintillator tiles. In addition, "Massless Gap" modules, so named because they include little absorber material, have been placed in both the CC and EC cryostats to sample energy deposition in these regions. These modules consist of single calorimeter cells, segmented in η and ϕ to match the calorimeter modules. But there is no absorber; instead, plates of copper-clad G10 provide the ground planes for the cells. The ICD and massless gap modules can be seen in Fig. 2.9. These features improve the energy and $\not{E}_T$ resolution of DØ [53].

2.2.4 Muon Detection

The muon system [25, 54, 55, 56] surrounds the calorimeters, as shown in Fig. 2.2 and Fig. 2.10. Muons pass through the calorimeter with minimal energy loss, so their momentum as well as their location must be determined by the muon tracking system. This is accomplished using a magnetic field inside the iron toroids of the muon system. Planes of drift tubes placed before and after the magnet determine the incident and final trajectories of each muon and thereby the momentum from the bend angle of the track.

Because the total depth of the material between the interaction point and outer muon chambers is so large, as shown in Fig. 2.11, it is highly unlikely that hadrons will punch through all the absorber and be misidentified as muons. Hence, the iron toroids also serve as hadron absorbers to stop any particles other than muons that penetrate the calorimeter.

The muon system has five toroids: one central toroid (CF), covering $|\eta| < 1$, two end toroids (EF), covering $1 < |\eta| < 2.5$, and two small-angle (SAMUS) toroids, which extend coverage to $|\eta| = 3.6$. These toroids are shown in Fig. 2.10.

The Wide-angle Muon System (WAMUS) consists of three layers of drift tubes in both the CF and EF regions. These layers are labeled in Fig. 2.10. The A layer, inside the toroid, has four planes of tubes. Used in conjunction with information from the central tracking system and the calorimeter, the A layer determines the initial trajectory of each muon. The B and C layers are located outside of the toroids and are used to determine the final trajectory of each muon. Each of these layers consists of three planes of drift tubes. The structure of drift tubes in the B

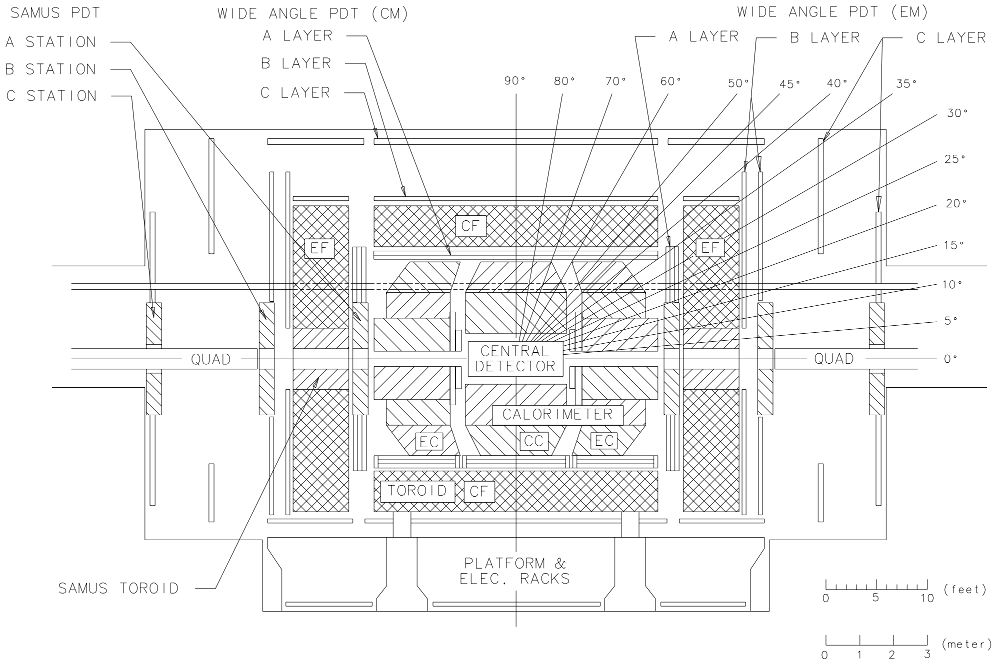

Figure 2.10: Elevation view of the DØ detector, showing the muon toroids and drift chambers.

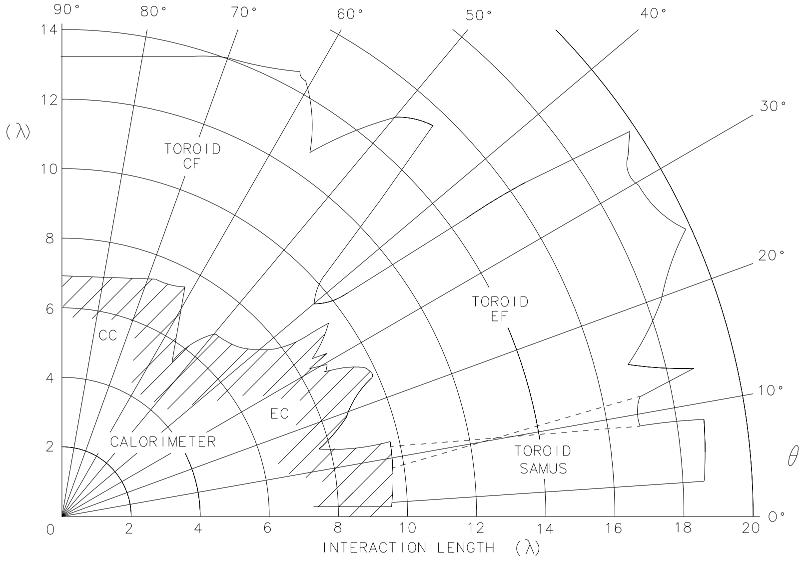

Figure 2.11: Interaction lengths of material (λ_A) as a function of rapidity.

and C layers is shown in Fig. 2.12; the A layer is similar, but has four planes of tubes instead of three. The relative offset between the planes provides resolution of the left-right ambiguity in each cell.

The drift tubes are oriented so as to provide the best possible measurement of the coordinate in the bend plane of the muon tracks. This is crucial for the momentum measurement. The longitudinal coordinate in each drift tube is measured using a diamond-shaped cathode pad. The diamond pattern is shown in Fig. 2.13. Both the inside and outside parts of this pattern are read out separately, and the ratio of these signals determines the position modulo the half-wavelength of the pattern (about 30 cm). A crude measurement of the longitudinal coordinate, based on the difference between the arrival times of the signals at each end of the sense wire, suffices to resolve this ambiguity.

The components of the Small-angle Muon System (SAMUS) are also shown in Fig. 2.10. The design is similar to that of WAMUS, but smaller cylindrical

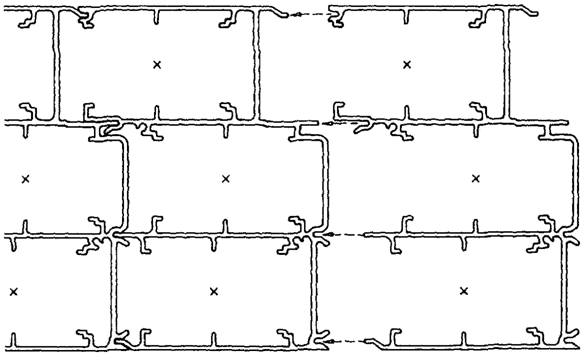

Figure 2.12: Cross section of WAMUS drift tubes. The sense wires are indicated by ×. In this view, the diamond-shaped cathode pads are on the upper and lower walls of each cell.

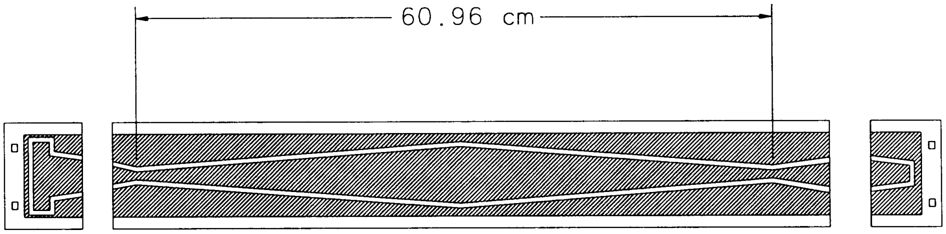

Figure 2.13: Cathode pad for a WAMUS drift cell.

Table 2.6: Parameters of the Muon System [25, 33, 34].

	WAMUS	SAMUS
$\lvert\eta\rvert$ coverage	0–1.7	1.7–3.6
Magnetic field	2 T	2 T
Interaction lengths (λ_A)	$\approx$ 13.4	$\approx$ 18.7
Number of modules	164	6
Number of drift cells	11,386	5308
Sense wire composition	50-μm Au-plated W, 300 g tension	50-μm Au-plated W, 208 g tension
Sense wire voltage	+4.56 kV	+ 4.0 kV
Cathode pad voltage	+2.3 kV	—
Gas used	Ar(90%)-CF_4(5%)-CO_2(5%)	CF_4(90%)-CH_4(90%)
Drift velocity	6.5 cm/μs	9.7 cm/μs
Maximum drift distance	5 cm	1.45 cm
Resolution: bend view	0.53 mm	0.35 mm
Resolution: non-bend view	0.3 mm	0.35 mm

drift tubes are used due to the high particle multiplicity near the beam pipe. Longitudinal coordinates are determined by orienting some of the planes at a small angle relative to the axis to provide stereo views.

Several parameters for the WAMUS and SAMUS systems are given in Table 2.6.

Multiple Coulomb scattering in the calorimeter and in the toroids limits momentum resolution in the system to around 20% accuracy for muon momenta up to 50–100 GeV. Studies of $Z \to \mu^+\mu^-$ events have yielded an estimate of the muon momentum resolution: $\delta(1/p) = 0.18(p-2)/p^2 \oplus 0.008$, where p is in GeV/c and the symbol $\oplus$ indicates addition in quadrature [57].

2.2.5 Triggering and Data Acquisition

At a luminosity of 5×10^{30} cm^{-2}s^{-1}, non-diffractive inelastic interactions occur in the Tevatron at a rate of about 150 kHz [25]. Recording of events to disk using the DØ data logger is limited to a rate of about 3 Hz. Therefore, a multilevel triggering system, with increasing sophistication at each level, is required to select the most interesting events. A brief description of the trigger and data acquisition systems is presented below. More detail can be found in Refs. [25] and [34].

Level 0

Selection of events begins with identification of inelastic events through the Level 0 trigger [25, 58, 59]. This is a hardware trigger consisting of two arrays of scintillator hodoscopes, placed between the CC and EC cryostats. The hodoscopes provide partial coverage for $1.9 < |\eta| < 4.3$ and full coverage for $2.3 < |\eta| < 3.9$. A non-diffractive inelastic collision is identified with $\geq$ 99% efficiency by the presence of signals in both Level 0 detectors [25]. The approximate position of the event vertex is determined from the difference in arrival times of signals from the two hodoscopes. This information is passed to the higher levels of the trigger system. Level 0 also serves as the luminosity monitor for DØ. The Level 0 trigger rate corresponds to the inelastic $p\overline{p}$ interaction rate of about 150 kHz.

Main Ring Veto

As has been noted, the Main Ring passes through the DØ calorimeter and muon system. Normally, during a store, the Main Ring is used for antiproton production. The presence of beam in the Main Ring causes interactions with remnant gas, etc., that spray the calorimeter or muon system. Such interactions can be vetoed at Level 1 (see below) using a special Main-Ring veto logic. In Run Ia, this was accomplished by using clock signals from the accelerator to veto triggers when the beam in the Main Ring passed through DØ. However, this led to unacceptably large (up to 25%) dead times; hence, for Run Ib, a more efficient veto scheme was developed [60], using both passive and active criteria for determining when to veto events, as described below.

Passive veto terms include the MRBS_LOSS signal, which is set in the early stages of the Main Ring's acceleration cycle, when losses are highest, and the MICRO_BLANK signal, which is set when the beam in the Main Ring passes through DØ in coincidence with the crossing of a Tevatron bunch. In addition, four active veto signals were added to the trigger logic. These vetos are based on signals detected in scintillation counters installed surrounding the Main Ring beam pipe just outside of both ends of the DØ detector. Each veto signal is activated for a fixed time interval after a sufficient number of hits are detected in the counters. All six of these signals are provided as inputs to the Level 1 trigger so that events that had interactions in the Main Ring can be vetoed.

Level 1

The process of reducing the event rate begins with the Level 1 (hardware) trigger [25, 61, 62]. This system reduces the event rate to about 150 Hz. The Level 1 trigger framework receives information from the calorimeter and muon triggers (described below) and from the Level 0 and Main Ring veto counters. The framework uses a 256-term AND/OR network that allows up to 32 distinct combinations of these inputs to be defined as trigger conditions. For each condition, any or all of the input terms may be required, vetoed, or ignored. The Level 1 trigger framework completes decisions within the 3.5-μs interval between Tevatron bunch crossings. Certain triggers require longer times and are referred to as Level 1.5 triggers.

The Level 1 calorimeter trigger [62] sums the electromagnetic, hadronic, and total energy in towers of $\Delta\eta = \Delta\phi = 0.2$. A hardware lookup table is used to convert these energies to transverse energies corresponding to an interaction at $z = 0$. Information from Level 0 is used to correct the E_T values for the true position of the vertex. The total scalar E_T is defined as the sum of the E_T in all towers. The $\not{E}_T$ is determined from the vector sum of the E_T of all towers. In addition, for Run Ib, "large tiles" were defined for use in jet triggers. These are similar to the trigger towers described above, but the dimensions of a large tile are $\Delta\eta \times \Delta\phi = 0.8 \times 1.6$. The total tower E_T, electromagnetic tower E_T, and large tile E_T are compared to programmable thresholds, and a list of towers (or tiles) above each threshold is provided to the Level 1 framework for use in trigger decisions. The scalar E_T and $\not{E}_T$ are also compared to programmable thresholds, and the results are passed to the Level 1 trigger framework.

The Level 1 muon trigger [63] determines the approximate "centroid" of each hit in the WAMUS chambers. The centroid is the half-cell that contains the most likely location of the track. Roads obtained from hits in the B and C layers are checked for a possible match to centroids in the A layer. When a match is found, a signal is passed to the Level 1 trigger framework. The full list of centroids is then sent to the Level 1.5 muon trigger for confirmation of the findings in Level 1. At Level 1.5, all combinations of A, B, and C centroids are compared to determine whether they correspond to muons with momenta above a programmable p_T threshold. SAMUS triggers at Level 1 and Level 1.5 have also been implemented, but the time required for their completion can be quite long due to the presence of many hits from the spray of particles from the Tevatron beam pipe.

When an event satisfies one or more Level 1 trigger conditions, the Level 1 framework initiates a readout of the full detector and, if necessary, initiates Level 1.5 processing. If the event fails at Level 1.5, the readout is aborted. Otherwise, the data are passed to Level 2. The event rate into Level 2 is about 150 Hz.

Level 2

The Level 2 (software) trigger [25, 64, 65, 66] consists of a farm of 48 VAX processors that collect and format the data for an event into ZEBRA [67] structures and invoke software filters that reduce the event rate from 150 Hz to about 3 Hz for data logging. Each processor is coupled to a multiport memory that is also accessed by the input data cables and the output buffer driver in order to maximize the speed of event transfers.

When a Level 1 trigger condition is satisfied, the signals from all detector channels are digitized using analog-to-digital converters that are housed in approximately 80 VME crates in the moveable counting house. In addition, information from the Level 0 and Level 1 triggers is prepared for readout. Digitization of all event information requires about 1 ms after the decision at Level 1. Each crate then transfers its data to a high-speed data cable. Eight such cables are used, corresponding, respectively, to the trigger, VTX, TRD, CDC, FDC, calorimeter (two cables), and muon data. The readout on each cable is controlled using a token-passing scheme to assure that no two crates simultaneously put data to the cable, that all required crates are read out, and that the data from all crates correspond to information for the same event [65]. The event is assigned to an idle Level 2 node. This node receives the data for the event in its multiport memory, mapping it directly into the desired event structure.

The Level 2 filtering code [66] consists of a number of tools that quickly reconstruct objects such as jets, muons, and electrons from the data. Each software tool is invoked with a set of parameters defining the minimum number of objects, the minimum E_T of each object, and other similar quantities. Up to 128 filter scripts can be defined, each consisting of one or more tools with specific values set for the parameters. Each filter script is associated with a specific Level 1 trigger and is invoked only if this trigger condition is satisfied. Information on the tool and filter results is added to the primary data located in the multiport memory.

If one or more filters are satisfied, a signal is sent to the output controller, which reads out the data for the event, including the trigger and filter information. The data are received by the host computer and logged to buffer disks, where files consisting of about 500 events are produced. These files are written to 8-mm tape for offline reconstruction and for permanent storage. The offline reconstruction algorithms will be discussed in the next chapter.

Host Computer

The host computer serves many functions in the operation of DØ. In addition to data logging, the host computer provides the user interface for run control. This interface allows the user to define triggers, select a subset of the detector crates to be read out, and begin and end data taking. Other processes on the host computer permit monitoring of data in real time so that problems can be detected quickly. In addition, the high voltage systems and other detector components are monitored, and alarms are generated if the prescribed tolerances are exceeded. These operations are described in detail in Refs. [25] and [34].

Chapter 3

Particle Identification

The DØ detector provides information about each event in the form of digitized electronic signals from its thousands of readout channels. From these signals, we reconstruct the physical objects—jets, muons, electrons, and so on—that passed through the detector. In this chapter, we present an overview of the event reconstruction program and describe the algorithms used to reconstruct the important objects for the search for the top quark in the all-jets channel.

3.1 Event Reconstruction

As we have said, Level 2 of the DØ trigger employs software algorithms to quickly reconstruct objects for use in trigger decisions. Because a fast decision is required, these algorithms do not use all of the available information. For instance, some of the detector signals are not considered at all, and information from calibration studies of individual detector channels is not available to Level 2. Complete reconstruction of events is performed offline, using a farm of processors that read the detector data from tapes and execute the program DØRECO.

3.1.1 DØRECO

The program DØRECO [68, 33, 34] reconstructs jets, muons, electrons, photons, and $\not\!\!E_T$ for each event. The results from this program are used as the starting point for every study of physics processes at DØ.

The structure of DØRECO is as follows. First, detector signals are converted to "hits." For the tracking chambers, a hit corresponds to a pulse of current of some given height on some specific chamber wire. For the calorimeter, a hit is a deposition of energy in a readout cell. In each case, to refine the measurements, DØRECO uses data from detector calibrations performed between stores. Next, the hits in the central tracking chambers are used to reconstruct charged particle tracks; these tracks are used to determine the location of the primary interaction vertex for the event. Using this vertex, jets, electrons, photons, and $\not\!\!E_T$ are reconstructed from the energy deposited in the calorimeter. Muon trajectories are reconstructed to determine the momentum of each muon. Information about the reconstructed objects is stored in files for later use in the analysis.

The results from DØRECO are stored in the form of ZEBRA [67] data structures describing the event. For each reconstructed object, DØRECO creates a ZEBRA bank containing the object's properties, such as energy, three-momentum components, and production angles. Additional information that is useful for judging the quality of the reconstruction is also included in this bank. Other information generated by DØRECO, such as the locations of hits, is stored in separate banks [68].

The output from DØRECO is recorded in two forms, each containing different levels of detail. The "standard" output, or STA, includes all of the characteristics of each reconstructed object, along with information from the Level 1 and Level 2 triggers, some of the unprocessed input data, and all of the information generated by DØRECO during the reconstruction process. The STA files are stored on 8-mm tape. They can be used to reconstruct events after changes have been made to the algorithms, or to provide all available information about individual events. The "data summary tape," or DST, is designed so that many event records can be read and analyzed quickly. It contains the information on all the reconstructed objects and information from the Level 1 and Level 2 triggers, but none of the input data and very little of the supplementary information generated by DØRECO. The DSTs are stored either on disk or on 8-mm tape [25, 68].

3.1.2 The Farm

DØ uses a large farm of Silicon Graphics and IBM processors to reconstruct events at the same rate at which they are recorded [69, 70, 71]. The farm consists of four "server" nodes, dedicated to handling input and output operations, and 24 "worker" nodes associated with each server. The worker nodes run DØRECO to reconstruct events received from the servers. Each server node has seven 8-mm tape drives and three "spooling" disks. This arrangement allows three input files to be read from tape, three files to be processed, and three output files to be written to tape, all in parallel, thereby maximizing throughput on the farm. One "job control" node coordinates activities among the servers to ensure efficient use of the available computing power. This node also provides access to the databases, executable programs, and command scripts that are used by the server and worker nodes.

The operation of the farm is as follows. Three input and three output jobs run on each server node. Each input job copies raw data files from tape to one of the three spooling disks, and each output job copies completed STA files from one spooling disk to tape for storage. In addition, another process runs on each server node that transfers completed DST files from all three spooling disks to the file server, which is a separate computer system that subjects the DST files to further processing and provides user access to data from reconstructed events.

In parallel with the input and output jobs, three processing jobs run on each server. Each processing job is assigned to a specific spooling disk and is allocated eight of the 24 worker nodes. The job transfers the data for each event in the input file on its disk to one of its allocated worker nodes. The worker node receives the data for the event and reconstructs the physical objects of interest. When the reconstruction is finished, the processing job receives the output event records (in STA and DST formats) and writes them to files on its spooling disk.

The farm can process events at a rate of 2–3 per second, which matches the rate for recording data [72].

3.2 Vertex Finding

In order to measure the polar angle (θ) for reconstructed objects, we must identify the interaction vertex for each event. Here, we briefly describe the vertex-finding algorithms used by DØ. More details can be found in Ref. [68].

The transverse (x-y) position of the interaction vertex is well constrained by the small ($\approx$ 40 μm $\times$ 40 μm) transverse size of the Tevatron beam in the DØ interaction region [20]. Consequently, it is not necessary to reconstruct this position for each event. Instead, at the beginning of each store, a vertex-finding program is used online to determine the mean x-y position of the vertex for about 500 events with tracks in the VTX chamber. The average x-y position is recorded in a database and used by DØRECO for all events in that store. The mean position is always quite close to the nominal center of the Tevatron beam and is stable over stores, fluctuating by less than 30 μm [68, 34].

The z position of the vertex is not well constrained because the Tevatron bunches are quite long ($\sim$ 30 cm). This position must therefore be determined for each event. This is done in DØRECO using the tracks reconstructed from the CDC. After all the tracks have been reconstructed, each track is projected into the r-z plane and extended to its intersection with the z axis. Clusters of tracks whose intersections with the z axis are near each other are identified, and the z position of the primary interaction vertex is determined from a Gaussian fit to the cluster that has the largest number of tracks. If other clusters are found, their positions are retained as additional vertexes. The resolution in the z position of the primary vertex is $\sim$ 6 mm if there are many tracks, or $\sim$ 2 cm if there is only one track. If there are no tracks in the CDC, as is the case for about 5% of events, tracks reconstructed from the FDC are used instead to constrain the z coordinate of the interaction point.

3.3 Jet Reconstruction

Jets of hadrons are created by the fragmentation of quarks or gluons. Due to the large number of particles in a typical jet, it is impossible to identify the individual particles or to assign each particle unambiguously to a parent parton. Experimentally, then, we must define jets according to some algorithm, and indeed many jet algorithms have been developed for this purpose. Here, we describe the algorithms used by DØRECO and explain the choice of algorithm for this search. Finally, we describe corrections to the jet energies that compensate for biases introduced by the calorimeter response and by the reconstruction algorithm.

3.3.1 Jet Algorithms

Because the fragmentation of partons into jets is characterized by small momentum transfer, we expect that most of the particles in a jet will be near each other in η-ϕ. We therefore reconstruct jets by clustering nearby depositions of energy in the calorimeter. In three of the jet algorithms used by DØRECO, jets are defined by clustering the energy deposited inside a cone of fixed radius in η-ϕ space. The fourth algorithm, called "nearest-neighbor," is based on the pattern of energy depositions in individual towers.

Common to all four algorithms is the first step: converting the calorimetric signals to the energy deposited in each cell [68]. The conversion is based on information obtained in previous test-beam studies and from the online calibrations of each readout channel between stores. The transverse energy in each cell is defined as $E_T = E \sin\theta$, where θ is defined by the center of the cell relative to the primary interaction vertex. The E_T values of individual cells are then summed longitudinally along θ in (0.1×0.1) towers of η-ϕ, and a list of towers is generated in descending order of E_T. This list of towers is used as the input to each jet algorithm.

For the fixed-cone algorithms [68, 73], "preclusters" are created from the list of towers. The first tower in the list is chosen as a "seed" for the precluster, and every tower that is within ± 0.3 units in η-ϕ of the seed and has $E_T > 1$ GeV, is added to the precluster. This precluster is saved, and the towers included in it are removed from the list of available towers. Using the next tower that remains on the list as a new seed, another precluster is formed. This process continues until every tower with $E_T > 1$ GeV has been assigned to a precluster.

Next, the jets are defined using the preclusters and all of the towers. The E_T-weighted centroid (in η-ϕ) of the precluster with largest E_T is calculated. All towers within a radius $\mathcal{R} = \sqrt{\Delta\eta^2 + \Delta\phi^2}$ of the centroid are clustered into a jet. The centroid of the jet is calculated, and all towers within $\mathcal{R}$ of the new centroid are clustered. This procedure is iterated until the centroid becomes stable. If the resulting jet has $E_T > 8$ GeV, it is retained. In order to find all of the jets, the algorithm is repeated using each precluster in turn as a starting point.

After the first jet is formed, every subsequent jet is checked to make sure that no tower has been assigned more than once. To prevent double counting of jets, the axes of the new jet and each previously-found jet are compared; if they are too close in η-ϕ (within 0.01 units), the new jet is discarded. Next, the list of towers in the new jet is checked for overlap with the list of towers in each previously-found jet. If two jets have any towers in common, then either the jets are merged, or the energy in the shared towers is divided between them. Two jets are merged into a single jet if either one shares more than 50% of its E_T with the other. Otherwise, the energy in the shared towers is divided by assigning each shared cell (not tower) to the jet whose axis is closest to that cell. In either case, the centroid and E_T of the affected jets are recalculated.

After all the jets are found, the following kinematic variables are calculated for each jet:

$$p_x = \sum_{k=\text{cells}} E^k \sin\theta^k \cos\phi^k, \tag{3.1}$$

$$p_y = \sum_{k=\text{cells}} E^k \sin\theta^k \sin\phi^k, \tag{3.2}$$

$$p_z = \sum_{k=\text{cells}} E^k \cos\theta^k, \tag{3.3}$$

$$E_T = \sum_{k=\text{cells}} E^k \sin\theta^k, \tag{3.4}$$

$$E = \sum_{k=\text{cells}} E^k, \tag{3.5}$$

$$\phi = \arctan(p_y/p_x), \tag{3.6}$$

$$\theta = \arccos(p_z/\sqrt{p_x^2 + p_y^2 + p_z^2}), \tag{3.7}$$

$$\eta = -\ln\tan(\theta/2), \tag{3.8}$$

where p_x, p_y, and p_z are the momentum components of the jet (assuming zero rest mass), E_T is the transverse momentum, and E the total energy of the jet.

Clearly, the cone size ($\mathcal{R}$) is an important parameter in this algorithm. More of a jet's energy will be contained inside a cone of larger $\mathcal{R}$. However, for events with many jets, large $\mathcal{R}$ will lead to a great deal of merging, leading to a loss of information about the detailed event structure. Because of such considerations, DØRECO reconstructs the jets in each event using three cone sizes: $\mathcal{R} = 0.3$, 0.5, and 0.7.

The nearest-neighbor algorithm [68, 74] uses the same E_T-ordered list of towers used by the cone algorithms. Beginning with the tower of largest E_T, the algorithm searches for the tower's "neighbor"—the nearby tower with next largest E_T. The search is restricted to the region where $\Delta\eta$ and $\Delta\phi$ are both less than 0.2 units (a 5×5 square of towers) and to towers with $E_T > 0.8$ GeV. If a neighbor is found, both towers are assigned to one group. The tower with largest E_T is removed from further consideration, but its newly found neighbor is not. Then the neighbor of the second tower in the E_T-ordered list is identified. If the second tower or its neighbor is part of the first group, these towers are both assigned to that group. Otherwise, they are assigned to a new group. The algorithm continues in this way until the neighbor of each tower has been identified. Because each neighbor may itself have another neighbor, the algorithm can assign many towers to one group. There is no iteration and no possibility that two groups share a tower. When all towers have been mapped, each group of connected towers is identified as a jet, but only if the E_T of the group exceeds 5 GeV. The kinematic variables for each jet are then calculated using Equations 3.1–3.8.

3.3.2 Choice of Algorithm

For each event, DØRECO provides the results from calculations using the three cone algorithms and the nearest-neighbor algorithm. A user can then select the algorithm that is best suited for any following analysis.

For the top search in the all-jets channel, one important consideration is the efficiency for reconstructing the six primary $t\bar{t}$ decay products. We have compared the four DØRECO jet algorithms [75] using a Monte Carlo simulation of $t\bar{t} \rightarrow$ all-jets events[*] with m_t of 180 GeV/c^2. (During Run Ib, the parameters of the nearest-neighbor algorithm were tuned to optimize the efficiency for reconstructing the six quarks in $t\bar{t}$ events [75]. This algorithm is now quite well suited to this search, and the results shown in Fig. 3.1 are from this optimized version. However, data from Run Ia and the early parts of Run Ib were reconstructed with the previous, non-optimized, version of the algorithm.) Figure 3.1 shows the results of the comparison. Parts (a) and (b) show, respectively, the η and p_T distributions of the six primary quarks for these events. We see that these quarks tend to be produced near $\eta = 0$, and that the p_T distribution peaks near 40 GeV/c and has an average value of about 55 GeV/c. Thus, the algorithm that we choose must have good efficiency for reconstructing jets that are produced at central rapidities with $p_T \approx$ 40 GeV/c.

To determine the efficiency of each algorithm, we searched for the six quarks in each event. A quark was defined as matched to a jet whenever the quark axis intercepted that of the jet within $\mathcal{R} = 0.5$. In Fig. 3.1(c), the efficiency for finding the quarks is shown as a function of η for all four algorithms. As this figure shows, all algorithms have low efficiency beyond $|\eta| \approx 2.5$. Fortunately, this is not an important region for $t\bar{t}$ production. In the central region, the $\mathcal{R} = 0.3$ cone

---

[*] The simulation will be described in Section 5.1.

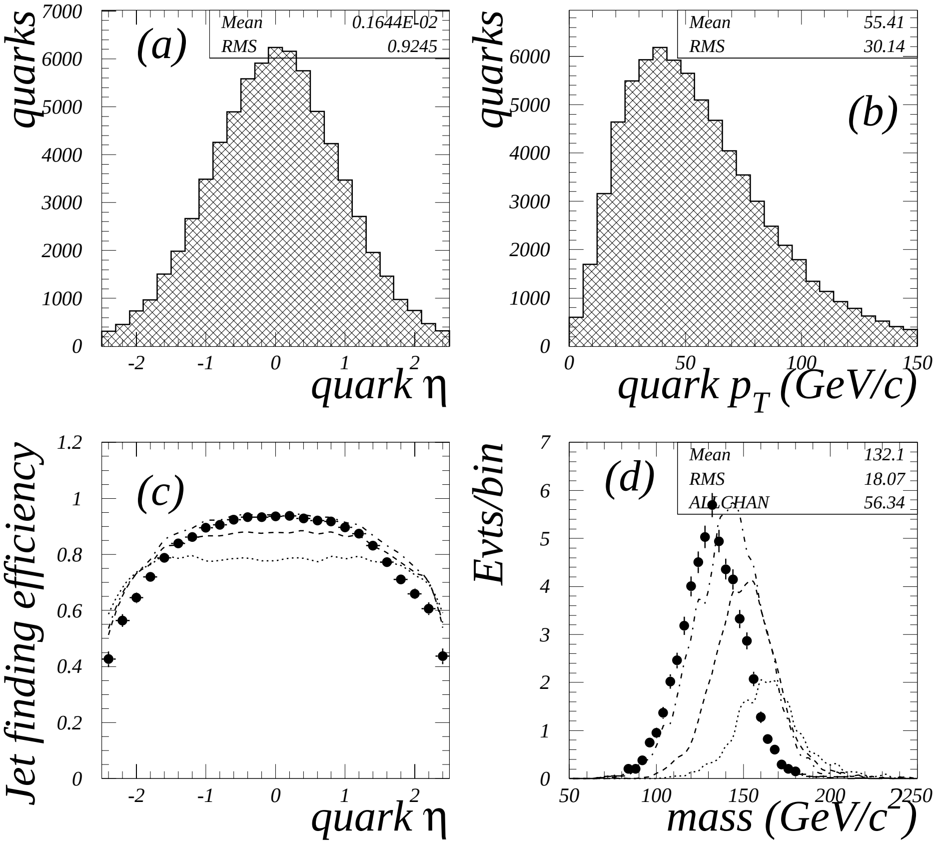

Figure 3.1: Comparison of jet algorithms. We compare the efficiency with which different jet algorithms match the six primary quarks from $t\bar{t}$ decay, for m_t of 180 GeV/c^2.

(a) η distribution of the six primary quarks.

(b) p_T distribution of the same quarks used in (a).

(c) Efficiency for reconstructing jets that match quarks, as a function of η, for $\mathcal{R} = 0.3$ cone (•), $\mathcal{R} = 0.5$ cone (dashed line), $\mathcal{R} = 0.7$ cone (dotted line), and nearest-neighbor (dot-dash line).

(d) Reconstructed mass of the top quark from correct jet combinations, using the four reconstruction algorithms (after jet energy corrections of Section 3.3.3). The areas reflect the overall efficiencies.

algorithm is almost as good as the nearest-neighbor algorithm, which appears to be most efficient.

Small differences in the efficiency (ε) of finding correct quark matchings are amplified when we examine correlations among the six quarks. The overall efficiency scales as ε^6, and the effect of this is demonstrated in Fig. 3.1(d). Here, we have reconstructed the masses of the t and $\bar{t}$ quarks using the jets that correspond to the correct combination of quarks, for events in which all six quarks were matched to jets. The distribution of masses is shown in the figure, and the area of each distribution reflects the efficiency for the corresponding algorithm to reconstruct properly all six quarks. We see that the mass is closer to the input top mass of 180 GeV/c^2 for larger cone sizes, but the price for this is a substantial loss in efficiency. It should be stressed that the energy loss due to particles radiated outside of the jet cone has not been taken into account in Fig. 3.1. When this is corrected, the mass value for the $\mathcal{R} = 0.3$ cone is expected to increase [76]. The shift in mass value is therefore less important than the loss in efficiency, and the smallest cone size appears to be the best in this case. The somewhat higher efficiency of the nearest-neighbor algorithm does not offset the lack of available data processed with this algorithm, and consequently, we choose the $\mathcal{R} = 0.3$ cone algorithm as the best tool available for our search.

3.3.3 Energy Scale Corrections

In order to study parton processes, we must correct the measured energies of jets for instrumental biases and biases from the reconstruction algorithm, as well as biases from gluon radiation.

There are three possible sources of bias in the calorimeter. First, the energy scale of the calorimeter, which was determined in test-beam studies, may not be correct for operating conditions. Second, even a high-E_T jet contains many particles with low E_T ($<$ 2 GeV). The calorimeter response is not linear at such low energies, and consequently, the sum of the energy in each tower does not accurately reflect the jet's energy. Finally, a small bias is introduced from the natural radioactivity of the uranium absorber plates, which produces additional energy in the calorimeter.

Other biases are introduced by the cone algorithm used to reconstruct jets. For instance, the hadronic shower is extended in space, and some energy can be lost because the shower extends beyond the jet cone. More energy will be lost because particles are radiated outside the cone during fragmentation and decay. Also, some energy will be added to the jet due to the "underlying event"—that is, the remnants of the spectator partons in the $p\overline{p}$ collision that are emitted into the cone of the large-E_T jet.

We correct the energies of jets to account for all of these effects. First, we correct for the electromagnetic calorimeter energy scale [57, 73, 77] by normalizing the Z mass reconstructed from $Z \to ee$ events to the LEP value, leading to a correction of about 5% in the CC and 1–2% in the EC [34]. We then corrrect for the hadronic energy scale using the "missing-p_T projection fraction" technique developed by CDF [78, 79]. This is based on a study of photon-jet events. It is assumed that in each event, the component of $\not\!\!E_T$ along the photon direction is due to mismeasurement of the jet energy. Parametrizing this effect as a function of the E_T and η of the jet, and of the fraction of the jet's energy that was deposited in the electromagnetic section of the calorimeter, provides a hadronic energy-scale correction for every jet.

Corrections for energy lost due to jet remnants showering in the calorimeter outside the cone of the jet have been determined from Monte Carlo simulations. These corrections do not include the full effect of gluon radiation outside the cone.

Additional corrections to compensate for the underlying event and for the effects of natural radioactivity in the uranium absorber plates were determined from studies of the energy flow in minimum-bias events [57].

None of the above corrections is incorporated into DØRECO. Instead, they are applied by users, via a package of software algorithms called CAFIX [80]. These algorithms correct the energies of jets, photons, and electrons, and recalculate $\not\!\!E_T$.

3.4 Muon Identification

Using information from alignment surveys and calibrations of the muon-chamber electronics, the muon reconstruction algorithm [68] begins by determining the size and point of origin of each hit in the muon drift chambers. Next, fits of straight lines to these hits are used to reconstruct track segments before and after the toroids. Complete tracks are then reconstructed by projecting each segment to the center plane of the magnet and matching inner and outer segments that intersect within an allowed error. Ambiguities in the reconstruction of segments and tracks are resolved by choosing the solution that corresponds to the muon of highest momentum, with segments that point toward the primary interaction vertex. This procedure introduces a small bias toward high-momentum muons into the algorithm.

After the track has been reconstructed in the muon chambers, it must be confirmed by hits in the calorimeter and central detectors. The calorimeter must have a trace of energy deposits corresponding to the passage of at least one minimum ionizing particle along the direction of the muon trajectory. In the central detectors, a track must be reconstructed that matches, within error, the inner segment of the muon track. If the muon is confirmed, a fit to all the data determines the trajectory and momentum of the muon. Finally, tests are performed to check the timing of the hits along the track. These tests are used to reject muons from cosmic rays that pass through the detector [57].

The criteria for muon reconstruction in DØRECO are not very restrictive. Information about each reconstructed muon track is therefore used subsequently to select muons of highest quality.

For our search, we are interested in muons that are likely to have originated from the decays of b-quarks. We refer to these as "muon-tags." Such muons will typically have low p_T and be localized near jets. To identify muon-tags, we impose the following requirements [75]:

- A fully reconstructed muon track must be present in the central (CF) region of the muon system. This is because b-quark jets from $t\bar{t}$ decays tend to be produced at central rapidities, and any increase in b-jet tagging efficiency gained through the use of forward (EF) quadrants is offset by complications from a lower track-finding efficiency.

- The track must satisfy the high-quality muon requirements. We consider the quality (χ^2 of the fit) of the track in both the bend and non-bend views, the projection of the inner track segment to the primary vertex, and the number of chambers along the track that had a hit.

- The calorimeter response in the track road must be consistent with the passage of at least one minimum ionizing particle. In particular, we require that the energy deposited in the calorimeter towers in a 2×2 road in η-ϕ around the muon trajectory be at least 1.5 times the energy expected for a minimum ionizing particle.

- The muon p_T must exceed 4 GeV/c. This requirement reduces the contamination from π and K decays and favors decays from heavy quarks.

- A jet with $|\eta| < 1$ and $E_T > 10$ GeV must be reconstructed (using the $\mathcal{R} = 0.3$ cone algorithm) within $\Delta\mathcal{R} = 0.5$ of the muon. This requirement selects muons that are products of semi-leptonic decays of heavy quarks.

The above requirements are identical to those used by DØ in identifying muon-tags for the lepton+jets channels [57], except that we require that the muon be within $\Delta\mathcal{R} = 0.5$ of a jet defined by a cone of $\mathcal{R} = 0.3$, while the other channels (which have fewer jets) use a cone of $\mathcal{R} = 0.5$.

3.5 Other Particles

DØRECO also reconstructs electrons, photons, and $\not\!\!E_T$. Electrons and photons are reconstructed using the nearest-neighbor algorithm, where the towers include only the energy deposited in each of the four EM layers and in the first FH layer [57, 68]. In addition, the algorithm's parameters are modified to achieve maximum efficiency for finding electrons and photons. To reject jets, DØRECO requires that at least 90% of each electron's or photon's energy (including all layers) is deposited in the electromagnetic section. An electromagnetic cluster is identified as an electron if there is a track in the central detectors that points toward the cluster. Clusters without such a track are identified as photons. Again, these criteria are not restrictive, and information on quality can be used to impose additional requirements. More details on electron reconstruction and the criteria used in selecting top candidates are given in Ref. [57].

The $\not\!\!E_T$ for the event is calculated from the vector sum of the E_T in each calorimeter cell, with $\not\!\!E_T$ defined as the negative of this vector [68, 73]. A second determination of $\not\!\!E_T$ that includes the p_T of reconstructed muons is also available. The CAFIX package allows the user to correct both calculations of $\not\!\!E_T$ in conjunction with the energy corrections for the calorimeter.

In our search, we use the possible presence of electrons and finite $\not{E}_T$ to reject events that are candidates for analysis of other decay channels of the $t\bar{t}$ final state.

Chapter 4

Data Samples

We now turn to the analysis of data for the search for the top quark in the all-jets channel. We begin with a discussion of the criteria used to select samples of multijet events.

4.1 Multijet Trigger

Selection of events begins online, where Level 1 and Level 2 trigger requirements are used to select events with many jets. These requirements have high efficiency for selecting events where $t\bar{t}$ decays to six jets. In order to reduce the number of events that we must consider for further analysis, the trigger requirements are designed to have low efficiency for identifying multijet events from sources other than $t\bar{t}$ decays.

During Run Ia, the Level 1 multijet trigger required that four calorimeter trigger towers (0.2×0.2 units in η-ϕ) have $E_T > 5$ GeV. In order to maximize the available luminosity, no vetoes on Main Ring activity were imposed. Studies based on a Monte Carlo simulation of $t\bar{t} \rightarrow$ all-jets events, with top mass (m_t) of 150 GeV/c^2, showed that these events satisfied the Level 1 requirement with 99% efficiency.

For events that satisfied the Level 1 requirement, jets were reconstructed at Level 2 using an $\mathcal{R} = 0.3$ cone algorithm similar to the one used in DØRECO. We required that Level 2 reconstruct at least 5 jets with $E_T > 10$ GeV and $|\eta| < 2.5$. The efficiency for satisfying Level 1 and Level 2 requirements was 86% for $t\bar{t} \rightarrow$ all-jets events with m_t of 150 GeV/c^2. For higher top masses, the E_T of the jets tends to be larger, and consequently, the efficiency is somewhat higher.

The trigger requirements were modified for Run Ib in order to reduce sensitivity to background while maintaining high efficiency for top. The new requirement at Level 1 was based on the use of large tiles (0.8×1.6 units in η-ϕ) rather than trigger towers. To maintain high efficiency for top masses as low as 150 GeV/c^2, we required three large tiles with $E_T > 15$ GeV. Because a single jet can deposit substantial energy in several towers, using the large tiles makes it more likely that an event that satisfies the Level 1 requirement does, in fact, have several distinct jets. Additional terms that required as many as 4 trigger towers with $E_T > 7$ GeV were added during the course of Run Ib in order to control the trigger rate at high luminosity by preferentially rejecting background. As in Run Ia, we did not use vetoes on Main Ring activity. The effects of these changes on the efficiency for triggering on $t\bar{t}$ events were studied using Monte Carlo simulations and were found to be negligible, especially for high-mass top. We found that the efficiency of Level 1 for Run Ib was somewhat reduced compared to Run Ia, but was still quite high: 94% for m_t of 150 GeV/c^2.

Initially, the Level 2 requirement was not changed. However, as the peak luminosity of the accelerator increased, we found it necessary to add a requirement that the sum of the E_T of the jets be greater than 110 GeV. This reduced the trigger rate considerably, but did not significantly affect the efficiency for signal for top masses above 150 GeV/c^2. For Run Ib, the efficiency for satisfying the Level 1 and

Table 4.1: Efficiency and $t\bar{t}$ yield of the multijet trigger. Values for trigger conditions from Run Ia and Run Ib are listed separately.

Top Mass	Efficiency (all-jets)		Yield (all $t\bar{t}$ decay modes)	
(GeV/c^2)	Run Ia	Run Ib	Run Ia	Run Ib
160	0.89	0.87	0.68	0.65
180	0.92	0.91	0.72	0.70
200	0.93	0.92	0.75	0.72

Level 2 requirements was 84% for m_t of 150 GeV/c^2.

The efficiency of the multijet trigger conditions for identifying $t\bar{t} \rightarrow$ all-jets events is shown for a range of top masses in Table 4.1. We also show the total $t\bar{t}$ yield, which is defined as the fraction of all $t\bar{t}$ events expected to satisfy the multijet trigger requirements. For the latter, we have considered all decay modes, assuming the branching ratios predicted by the Standard Model (see Table 1.2). The efficiency for the all-jets channel is high, and the size of the total $t\bar{t}$ yield suggests that a substantial contribution from decays other than just all-jets will be present at the trigger level. Most of the additional yield comes from the e+jets, μ+jets, and τ+jets channels, where at least four jets are expected to be present. As we will discuss in Section 4.3, we reject those events that would be included in the data samples for the analysis of e+jets and μ+jets channels. Consequently, the contribution from these channels to the all-jets search sample is expected to be small. We do not have a reliable algorithm for identifying τ leptons, so the contribution from such events, especially with small $\not\!\!E_T$, is still present in the all-jets data. As the table indicates, for a given top mass, the efficiency for the trigger conditions for Run Ia is about 2% higher than for Run Ib. The efficiency for both runs increases slightly with top mass.

The uncertainty in estimating the trigger efficiency is dominated by the accuracy with which our Monte Carlo simulation models the performance of the trigger system. For the multijet trigger, comparisons of data and Monte Carlo indicate that the simulation is accurate to within 5% [75, 81].

4.2 Removal of Instrumental Backgrounds

Some of the signals in the detector are from sources other than $p\overline{p}$ collisions in the Tevatron. These background sources include spray from proton interactions with remnant gas in the Main Ring, and noise in the detector electronics. We removed such events from subsequent analysis at only a small cost in efficiency for $t\overline{t}$ signal. The selection criteria used to accomplish this [82] are described below.

First, we identified runs that were known to have malfunctions in the calorimeter, muon, or readout system. Because such data were likely to contain spurious jets, all events in these runs were rejected. This reduced the data sample by about 4%.

Next, because the multijet trigger did not veto events during periods of intense Main Ring activity, we used the pattern of deposition of energy in the calorimeter to identify events that had substantial energy from interactions in the Main Ring. We required that the scalar sum of E_T in all cells in the coarse hadronic section of the CC and in the outer hadronic sections of both ECs be less than 500 GeV. This requirement rejected about 2% of all events.

We also rejected events that had too much energy observed in the calorimeter. A small number of events had more than 4 TeV of energy in the calorimeter and were rejected as obvious mismeasurements. In addition, we rejected events in which the scalar E_T—the sum of the E_T in all cells of the calorimeter, ICD, and massless gaps—was greater than 1 TeV. Because the $p\overline{p}$ center-of-mass energy in the Tevatron is 1.8 TeV, the likelihood of any single interaction producing 1 TeV of scalar E_T is quite small (much less than 1%); such events were attributed to noise, to events in the Main Ring, or to rare multiple interactions. These requirements removed about 2% of all events.

Noise and events from sources such as the Main Ring will generally produce extra energy in only one section of the calorimeter, causing an imbalance in the transverse energy of the event. Of course, in the all-jets $t\bar{t}$ channel we do not expect neutrinos with large E_T that would lead to substantial $\not\!\!E_T$ in the calorimeter; consequently, we rejected events with excessive $\not\!\!E_T$, using a requirement that the $\not\!\!E_T$ "significance," which we define as the ratio of $\not\!\!E_T$ to scalar E_T, be less than 0.4. The distribution in $\not\!\!E_T$ significance is shown in Fig. 4.1. It is preferable to use the significance rather than $\not\!\!E_T$ because the resolution in $\not\!\!E_T$ in DØ is essentially proportional to scalar E_T [57], and since $t\bar{t}$ events tend to have large scalar E_T, a cut on $\not\!\!E_T$ could reject $t\bar{t}$ events simply because of poor experimental resolution. By using the significance, we can minimize this problem and reject $t\bar{t}$ events from decay channels that have high-E_T neutrinos. This requirement removed another 2% of all events.

The surviving events still showed evidence of contamination from interactions caused by protons in the Main Ring, as can be seen from the distribution in jet ϕ shown in Fig. 4.2. To remove these, we rejected any event that had a jet in the region $|\eta| < 1.5$ and $1.6 < \phi < 1.8$ (*i.e.*, where the Main Ring passes through the outer region of the central calorimeter), but only if over 40% of the transverse energy was deposited in the coarse hadronic section of the calorimeter. About 8% of all events were rejected through this criterion.

Some of the remaining events had jets that could be attributed to noise in the calorimeter electronics or to fluctuations in the natural radioactivity from the uranium absorber. To remove this contamination, we rejected events that had a jet with more than 70% of the E_T located in the coarse hadronic section; this com-

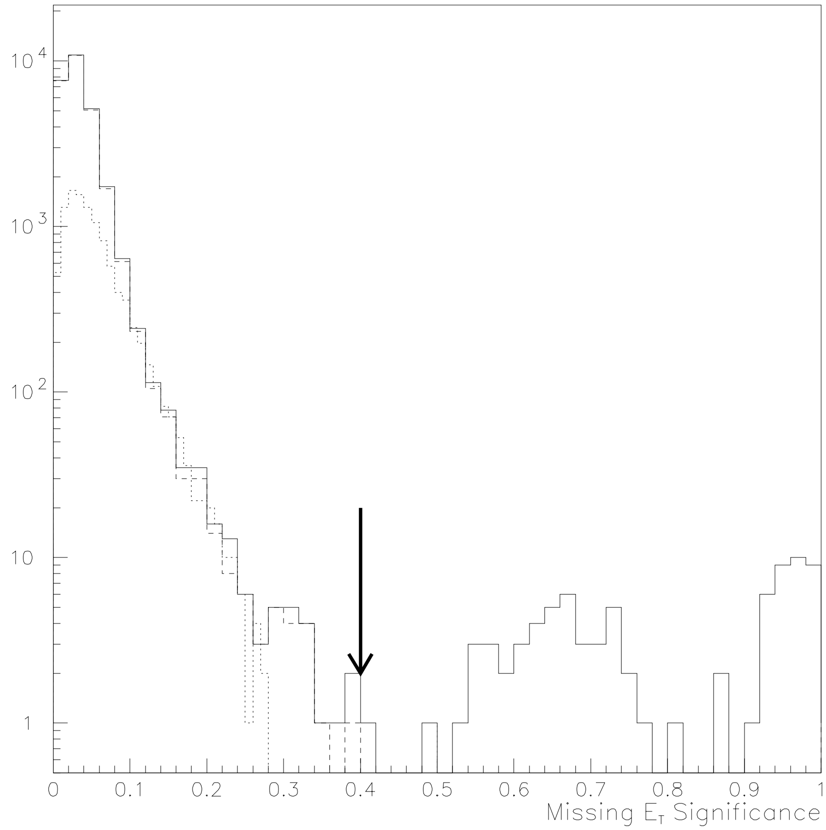

Figure 4.1: Distribution in $\not\!\!E_T$ significance for a subset of data, before (solid line) and after all criteria of Section 4.2 (dashed line). The dotted line represents the shape of the distribution for 180-GeV/c^2 $t\bar{t}$ events from ISAJET Monte Carlo. Our cutoff point is indicated by the arrow.

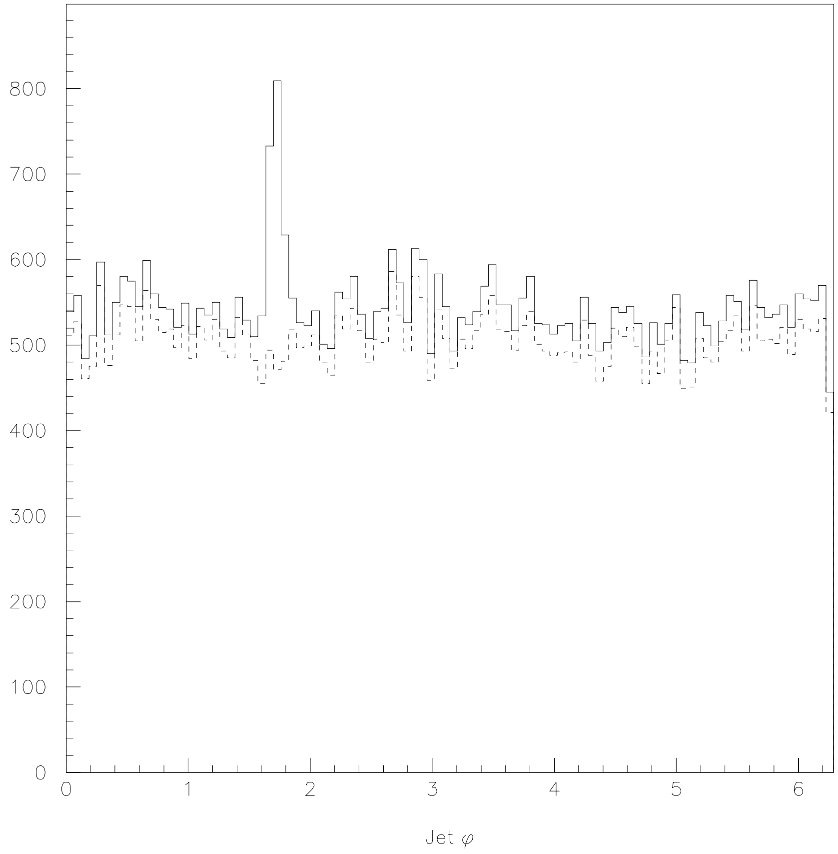

Figure 4.2: Distribution in ϕ of jets for a subset of data, before (solid line) and after all criteria of Section 4.2 (dashed line). The Main Ring is at $\phi \approx 1.7$.

prised about 1% of the remaining data. We also identified cells with largest (cell 1) and second-largest (cell 2) E_T in each jet, and required that $E_T(\text{cell } 1)/E_T(\text{cell } 2)$ be less than 50. Events with jets that failed this requirement, corresponding to about 1% of the remaining events, were rejected.

For about one in every 20,000 events, the $\mathcal{R} = 0.3$ cone algorithm reconstructed more than 14 jets per event. These events were also rejected.

In addition, we rejected events from another small source of noise, namely, grounding problems that occasionally led to spurious signals in all the cells in the outermost ring ($|\eta| = 1.4$) of the ECEM calorimeters. These events were removed using a cut on an energy-weighted RMS deviation of the jets in η, defined as:

$$\eta^2_{RMS} = \frac{\sum_{jets} \eta^2 E_T}{\sum_{jets} E_T} - \left(\frac{\sum_{jets} \eta E_T}{\sum_{jets} E_T} \right)^2 . \tag{4.1}$$

The distribution in this quantity, for data and for two samples of Monte Carlo $t\bar{t}$ events, is shown in Fig. 4.3. Requiring $\eta_{RMS} > 0.1$ removed such events (less than 1% of the data) without reducing the efficiency for $t\bar{t}$ signal.

The effect of the above requirements on the efficiency for $t\bar{t}$ signal has been studied using Monte Carlo simulations. We find that the total effect is a loss of only about 0.5% in efficiency.

4.3 “Generic” and “Search” Samples

After removing the instrumental backgrounds, we still had about one million events, of which about 200 were expected to be due to $t\bar{t}$ production. We reduced this sample by applying further selection criteria to reject background.

First, we required that DØRECO find five jets (using the $\mathcal{R} = 0.3$ cone algorithm) with $|\eta| < 2.5$ and $E_T > 8$ GeV prior to application of CAFIX corrections. Then

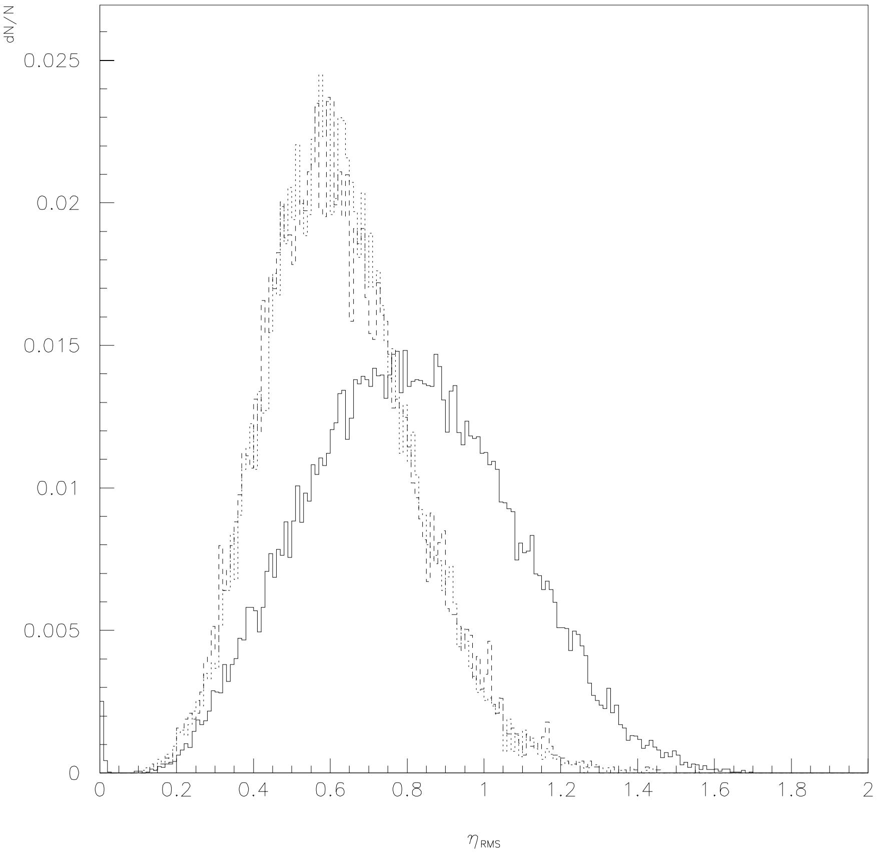

Figure 4.3: Distribution in η_{RMS} for data (solid line) and for ISAJET $t\bar{t}$ Monte Carlo, with m_t of 140 GeV/c^2(dashed line) and 180 GeV/c^2 (dotted line). These distributions are normalized to the same area. The events in the lowest bins, which are due to noise, are rejected by requiring $\eta_{RMS} > 0.1$.

we required that H_T, defined as:

$$H_T \equiv \sum_{j=1}^{N} E_T^j, \tag{4.2}$$

where the sum includes all jets in the event with $|\eta| < 2.5$, be at least 115 GeV. We refer to the events that satisfy these criteria as comprising the "generic" multijet sample. This sample consisted of 77,575 events from Run Ia and 294,980 events from Run Ib. It was used to determine the probability of finding a muon-tag in a jet in background events (see Section 5.4.2).

Starting with the generic sample, we imposed additional requirements to define the "search" sample. First, we required that each event have six jets with $|\eta| < 2.0$ and $E_T > 10$ GeV (after applying CAFIX corrections). Figure 4.4(a) shows the distribution in the number of jets in each event that meet these requirements for the generic multijet data sample, and for Monte Carlo $t\bar{t}$ events assuming m_t of 160 and 200 GeV/c^2. Requiring at least six jets leads to some loss in the efficiency for signal, but the rejection in background (*i.e.*, data) is large enough that imposing this requirement enhances the signal-to-background ratio. We also increased the H_T threshold requirement to 150 GeV, where only jets with CAFIX-corrected E_T above 15 GeV and $|\eta| < 2.0$ are included in the calculation of H_T. The distribution in H_T for the generic multijet data sample, and for the two sets of Monte Carlo $t\bar{t}$ events, is shown in Fig. 4.4(b). We see that requiring $H_T > 150$ GeV has very little effect on $t\bar{t}$ events. Finally, we rejected events that had an isolated electron with $E_T > 20$ GeV or an isolated muon with $p_T > 15$ GeV/c. By rejecting these events, we ensured that the result from the all-jets channel was statistically independent of results from the lepton+jets channels, which require isolated leptons with high p_T [2, 57]. The search sample consisted of 12,948 events from Run Ia and 45,277 events from Run Ib. As its name suggests, the search for a top signal was performed

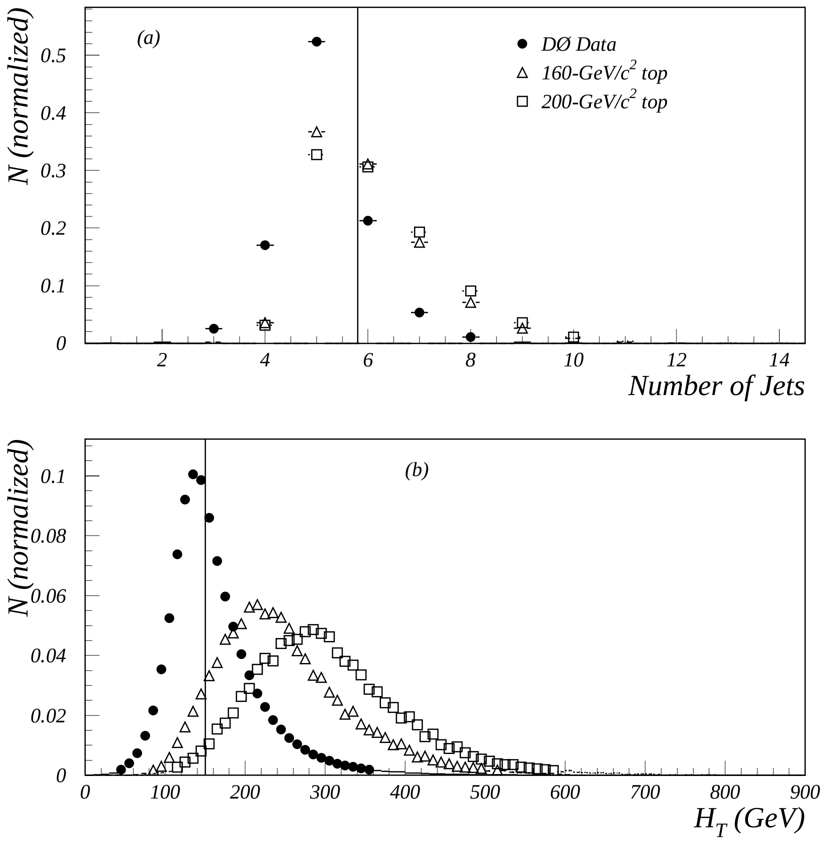

Figure 4.4: Distributions in number of jets (a) and H_T (b) for the generic multijet data sample (circles), and for ISAJET $t\bar{t}$ Monte Carlo with m_t of 160 GeV/c^2 (triangles) and 200 GeV/c^2 (squares). The distributions have been normalized to the same area. The minimum threshold requirements used to define the search sample are indicated by a vertical line in each plot.

using this sample.

4.4 Comparison of Run Ia and Run Ib Data

In our search for $t\bar{t}$ in the all-jets channel, we use data collected during two different running periods, during which there were changes in the trigger requirements and in the DØRECO algorithms. If the two data samples were sufficiently different in character, then our search could be sensitive to specific properties of the data from Run Ia and Run Ib. To investigate this issue, we have used the separate generic multijet data samples to identify any differences in the data collected during the two periods.

Figure 4.5 shows the distributions in H_T, the highest jet E_T value in each event, the sixth-highest jet E_T value in each event, and the E_T distribution of all the jets. The data for both running periods have been normalized to the same area. Very little difference is observed between Run Ia and Run Ib, and no systematic shift in the energy scale is apparent in either the H_T or inclusive jet E_T distributions.

We do see a small discrepancy in the E_T distribution for the sixth-highest jet: the energy scale for these low-E_T jets appears to be a bit lower in Run Ib. We have established [75] that this effect can be traced to a change in the sampling weights used in DØRECO for the ICD region, which were higher for the reconstruction of data from Run Ia than Run Ib. This affects the likelihood that any low-E_T jet in the ICD region would survive the 8-GeV cutoff imposed by DØRECO. However, the size of the effect is small enough that it is possible to consider the data from Run Ia and Run Ib together, at least as far as properties of jets are concerned.

There were also changes in the performance of the muon chambers during the course of the run (due largely to aging of the chambers in the high-rate environment). These changes caused some differences in the reconstruction of muons for events from Run Ia and Run Ib. In Section 5.4, we will describe how these differences are handled in our search.

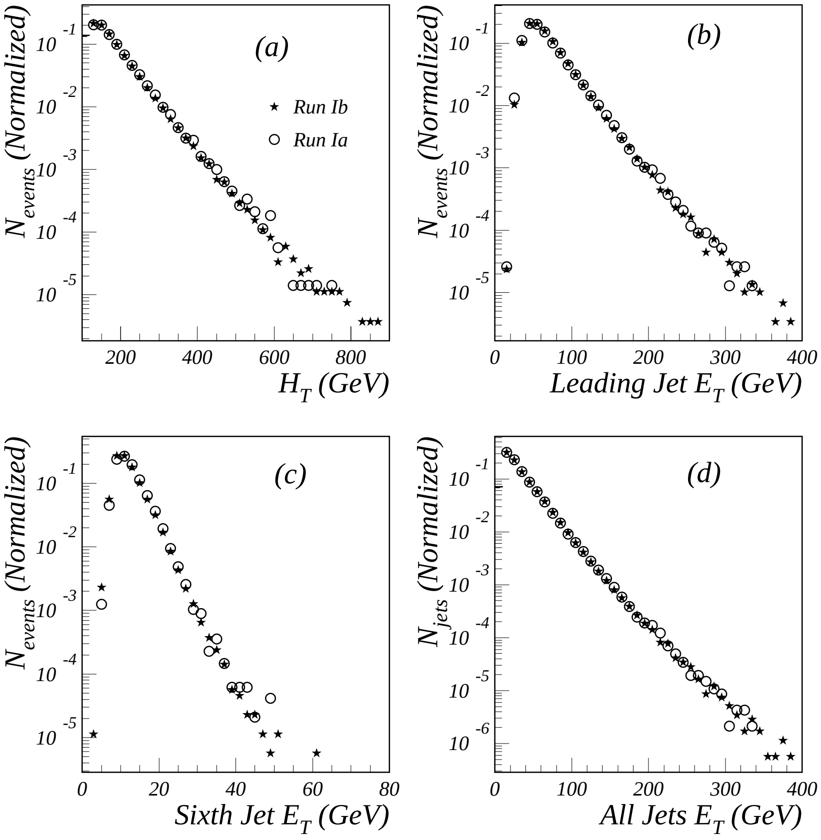

Figure 4.5: Distributions in E_T-related quantities for Run Ia (circles) and Run Ib (stars). Shown are distributions in H_T (a), E_T of the jet with highest E_T in each event (b), E_T of the jet with sixth-highest E_T in each event (c), and E_T of all jets (d). Distributions for both running periods have been normalized to the same area.

Chapter 5

Comparing Signal to Background

In Chapter 4, we described the criteria used to select the data sample for the search for the top quark in the all-jets channel. However, the ratio of signal to background that we expect in the search sample is still extremely small. In this chapter, we will describe two methods of distinguishing signal from background. First, we will introduce four parameters that distinguish the kinematics of $t\bar{t}$ production from other processes. Then we will describe a method of exploiting the presence of b-quark jets in $t\bar{t}$ events. In Chapter 6, we will use these properties to try to determine whether a contribution from $t\bar{t}$ production is present in the data.

5.1 Simulation of $t\bar{t}$ Events

Before we can distinguish between signal and background, we must know what to expect from each. In the case of signal, no large samples of $t\bar{t}$ events exist, and therefore, we must determine the properties of $t\bar{t}$ production from the Standard Model. However, quantum processes can be described only in probabilistic terms, and processes such as the fragmentation of partons into jets are too complex and too poorly understood to be calculated analytically. To solve these difficulties, computer programs have been developed that use simulation (Monte Carlo) techniques [7, 83], making use of random number generators. These programs simulate the behavior of elementary particles and the response of the detector to these particles in individual events. In an ideal simulation, the distribution in any physical quantity (such as the number of jets or H_T) for a large number of simulated events will match the distribution observed for real events.

We use Monte Carlo programs to generate large numbers of $p\overline{p} \rightarrow t\overline{t}$ events. Inputs to the program include the assumed mass of the top quark, along with values of other parameters for the Standard Model, such as the masses of the W and Z bosons. The specific interactions involve partons within a proton and an antiproton that collide to produce a $t\overline{t}$ pair. The four-momenta of the incident partons are chosen according to parton distribution functions that provide the momentum fractions for the constituents of a proton. The colliding partons determine the observed momenta of the t and $\overline{t}$ quarks. Decays of the t and $\overline{t}$ quarks, as well as their eventual fragmentation in the final state into jets, are also simulated in the Monte Carlo. The radiation and subsequent fragmentation of gluons from any of the quarks or gluons in the event is also modeled, and finally, the remnants of the original $p\overline{p}$ system (including any gluon radiation) are fragmented into hadrons. A more detailed description of these complex programs is given in Ref. [33, 84].

Several programs for generating events from $p\overline{p}$ collisions are available for general use. These tend to differ primarily in the modeling of the fragmentation of partons into jets. Also, because the parton distribution functions for the proton are not known precisely, most programs offer several choices for this aspect of the simulation. The differences among models affect the properties of the generated jets and other particles. It is therefore important to compare more than one model of a process with the data. For our analysis, we have used samples of $t\overline{t}$ events generated using the program ISAJET [85]. In order to estimate the reliability of the simulation, we have also considered samples of $t\bar{t}$ events generated using the program HERWIG [86].

In order to compare Monte Carlo events to our data, we must also model the response of the DØ detector to the generated particles. Our detector simulation is based on the program GEANT [87], which uses Monte Carlo methods to simulate the interaction of high-energy particles with matter. GEANT must be provided with a description of the composition and geometry of each part of the detector and information about the measured response and resolution of each subsystem. Except for the calorimeter, the parametrization of the detector geometry with the "DØGEANT" program is quite detailed. If the simulation of jets in the calorimeter were to involve full shower development in each absorber plate and sampling region, it would require far too much time to be of practical value. We have therefore chosen to represent the calorimeter as a homogeneous mixture of absorber and argon, with a resolution matched to the data obtained in the test beam. For each chosen interaction, the DØGEANT program uses Monte Carlo methods to generate corresponding signals that might be observed in the DØ detector. More details of the simulation procedure can be found in Refs. [25, 68].

Because a jet may consist of hundreds of particles, the time required to simulate the response of the detector to a jet—even using the homogeneous model of the calorimeter—is quite long. For many applications, we have found it acceptable to reduce the computing power required by further simplifying this aspect of the simulation. Instead of simulating the shower and calorimeter response for every particle in every jet, a "shower library" has been created [88]. This library consists of many showers generated by DØGEANT, for different types of particles, over an appropriate range of energies, production angles, and interaction points. For each particle in a jet, a corresponding shower is selected from the library, and these showers are combined to yield the total response to the jet. This response is then smeared to account for the effects of the energy resolution of the calorimeter. Although using the shower library reduces the possible variations within jets, the general quality of the simulation appears to be unaffected.

We also have a program that models the response of the trigger system [33, 68] for use in studying the effects of any particular requirements. The efficiency of the multijet trigger for selecting $t\bar{t}$ events, which was listed in Table 4.1, was determined from this simulation.

Finally, after generation, Monte Carlo events are processed using DØRECO and compared with data in fully reconstructed form. Information about the reconstructed particles and partons in each event is also used to compare the reconstructed objects to the original objects generated in the Monte Carlo.

The DØ collaboration has accumulated large samples of Monte Carlo $t\bar{t}$ events that have been used in searching for and studying the properties of the top quark. A sample of 30,000 $t\bar{t}$ events was generated with ISAJET with each of the following top masses: 140, 160, 180, and 200 GeV/c^2. These samples include events for all decay channels allowed by the Standard Model, with fractions determined by the appropriate branching ratios. Consequently, $t\bar{t} \rightarrow$ all-jets events comprise about 44% of each sample (about 13,500 events at each top mass). The events have all been processed using the trigger simulator and DØRECO, and will be used to represent the $t\bar{t}$ signal in our analysis.

We will optimize the selection criteria for data using the events where $t\bar{t}$ decays to all jets. However, in calculating any cross section for $t\bar{t}$ production, we will have to check the sensitivity of our selection criteria to other $t\bar{t}$ decay modes. For this purpose, we use the full $t\bar{t}$ samples (30,000 events).

Table 5.1 lists the acceptance and expected number of $t\bar{t} \rightarrow$ all-jets events ($N_{t\bar{t}}$) for the generic and search data samples from Run Ia and Run Ib (see Section 4.3).

Table 5.1: Acceptance and expected number of $t\bar{t} \to$ all-jets events ($N_{t\bar{t}}$) for generic and search samples. $N_{t\bar{t}}$ is based on the measured cross section for $t\bar{t}$ production.

Top Mass	Generic Sample		Search Sample	
(GeV/c^2)	Acceptance	$N_{t\bar{t}}$	Acceptance	$N_{t\bar{t}}$
160	0.880	244	0.607	168
180	0.917	193	0.664	140
200	0.929	153	0.705	116

For each sample, we have determined the number of expected events from the standard definition:

$$N_{t\bar{t}} = \varepsilon_{\text{all-jets}} \times \text{BR} \times \sigma_{t\bar{t}} \int \mathcal{L}\, dt, \tag{5.1}$$

where $\sigma_{t\bar{t}}$ is the cross section for $t\bar{t}$ production measured by DØ [2, 89], $\int \mathcal{L}dt$ is the integrated luminosity (58.4 pb^{-1}), $\varepsilon_{\text{all-jets}}$ is the acceptance for detecting $t\bar{t} \to$ all-jets events (given in Table 5.1), and BR is the 44% branching ratio expected for the all-jets channel. Since the generic data sample contains over 372,000 events, and the search sample, 58,000, the ratio of signal to background in the search sample is therefore always $\lesssim 1/350$.

As we have noted, it is important to understand to what extent the analysis depends on the details of the model used for simulating $t\bar{t}$ production. For that reason, we have used HERWIG (which models parton fragmentation quite differently from ISAJET) to generate samples consisting of 5,000 $t\bar{t} \to$ all-jets events, with each of the following top masses: 140, 150, 160, 180, and 200 GeV/c^2. We estimate the extent to which our analysis depends on the details of the simulation by comparing results from the two generators. We find that the differences are small on average, but in rare cases (the tails of distributions), they can become substantial. These effects will be addressed in Chapter 6.

5.2 Using Data as Background

As we noted in Chapter 1, modeling multijet background processes on the basis of QCD is not a reliable approach, and we have no satisfactory theoretical simulation of the background. However, the search sample itself represents a relatively pure background sample. The generic sample has even smaller "contamination" from signal, but due to its less restrictive requirements on the number of jets and on H_T, its kinematic properties are substantially different from those of the search sample. We therefore use the search sample of data as representative of the background, and compare these events to Monte Carlo $t\bar{t}$ events in order to identify kinematic variables that can be used as selection criteria for the signal.

5.3 Kinematic Properties of $t\bar{t}$ Events

As a result of our studies, we have identified several parameters that provide good discrimination between $t\bar{t}$ signal and background in multijet events. These parameters quantify features that serve to distinguish the kinematics of $t\bar{t}$ production from background. In selecting data for the search sample, we made use of only one kinematic parameter, H_T. Many other parameters can be constructed that can be used to distinguish signal from background. Here, we present distributions of four such parameters, compare their discriminating power, and examine the correlations among them. In Chapter 6, we will define the final selection criteria for our analysis using all four of these parameters. Ref. [82] contains a more detailed study of the kinematics, and discusses other, less useful, discriminators.

For the comparison of different parameters, we have used all of the events in the search sample to represent background. We have also applied the requirements that define the search sample to the $t\bar{t}$ Monte Carlo and retained contributions only from events in the all-jets channel for determining the acceptance at any stage of the analysis.

5.3.1 H_T^{3j}

The most common background processes are of the type in which two partons (usually gluons) scatter, producing two or three partons with large E_T that subsequently radiate additional gluons. These radiated gluons tend to have much lower E_T than their parents. In contrast, most of the jets in $t\bar{t}$ events originate from the decays of the two massive quarks and tend to have large E_T. We therefore expect that a variant of H_T, in which the two jets in the event with largest E_T are excluded, can provide substantial discriminating power between signal and background [90]. Assigning a consecutive number to each jet in an event, in order of descending E_T, we define:

$$H_T^{3j} = \sum_{j=3}^{N} E_T^j, \tag{5.2}$$

where in the sum we choose to include only jets with $|\eta| < 2$ and $E_T > 10$ GeV.

Distributions in this parameter are shown in Fig. 5.1(a), for data (which is mainly background) and for ISAJET $t\bar{t}$ Monte Carlo with m_t of 160 and 200 GeV/c^2. All samples have been normalized to the same area. In Fig. 5.1(b), we show the absolute number of events that survive a threshold requirement on H_T^{3j} as a function of that threshold, for data and for both $t\bar{t}$ Monte Carlo samples. The number of $t\bar{t}$ events is determined from the acceptance and $t\bar{t}$ cross section via Equation 5.1. In Fig. 5.1(c), we give an estimate of the expected ratio of signal to background in the data as a function of threshold requirement on H_T^{3j}. Here we have assumed that the data contain the number of top events ($N_{t\bar{t}}$) indicated in Fig. 5.1(b), so that $N_{\text{bkg}} = N_{\text{data}} - N_{t\bar{t}}$. The results for m_t of 160 and 200 GeV/c^2 are shown. Finally, in Fig. 5.1(d), we show an estimate of the statistical significance of the signal as a function of threshold requirement, with significance defined as $N_{t\bar{t}}/\sqrt{N_{\text{data}}}$. Again, we show results for m_t of 160 and 200 GeV/c^2. The apparent structure in parts (c) and (d) of Fig. 5.1 may be the result of statistical fluctuations in the region where only a few events satisfy the threshold requirement.

As Fig. 5.1 indicates, the effect of H_T^{3j} depends on the mass of the top quark, and its discriminating power clearly increases with m_t. In order to observe a signal, we must achieve a signal-to-background ratio that is close to unity. A requirement on H_T^{3j} alone does not suffice to achieve this without eliminating almost all of the expected signal.

5.3.2 Centrality

Events that involve very hard scattering of the incident partons tend to produce particles with large transverse momenta, generally at large angles relative to the beam. Because top production involves a hard scatter (momentum transfer comparable to m_t), whereas other QCD processes are "softer," a parameter that characterizes the fraction of momentum in the transverse plane should be a useful discriminator between signal and background. We define the quantity centrality ($\mathcal{C}$) as:

$$\mathcal{C} = \frac{\sum\limits_{j=1}^{N} E_T^j}{\sum\limits_{j=1}^{N} E^j}, \tag{5.3}$$

where the sums include all jets in the event with $|\eta| < 2$ and $E_T > 10$ GeV. The advantage of this parameter is that, unlike H_T or H_T^{3j}, it depends only weakly on the mass of the top quark.

Characteristics of $\mathcal{C}$ are shown in Fig. 5.2, in a format identical to that used for H_T^{3j}. In Fig. 5.2(a), we see that $\mathcal{C}$ does not depend on top mass. The difference in

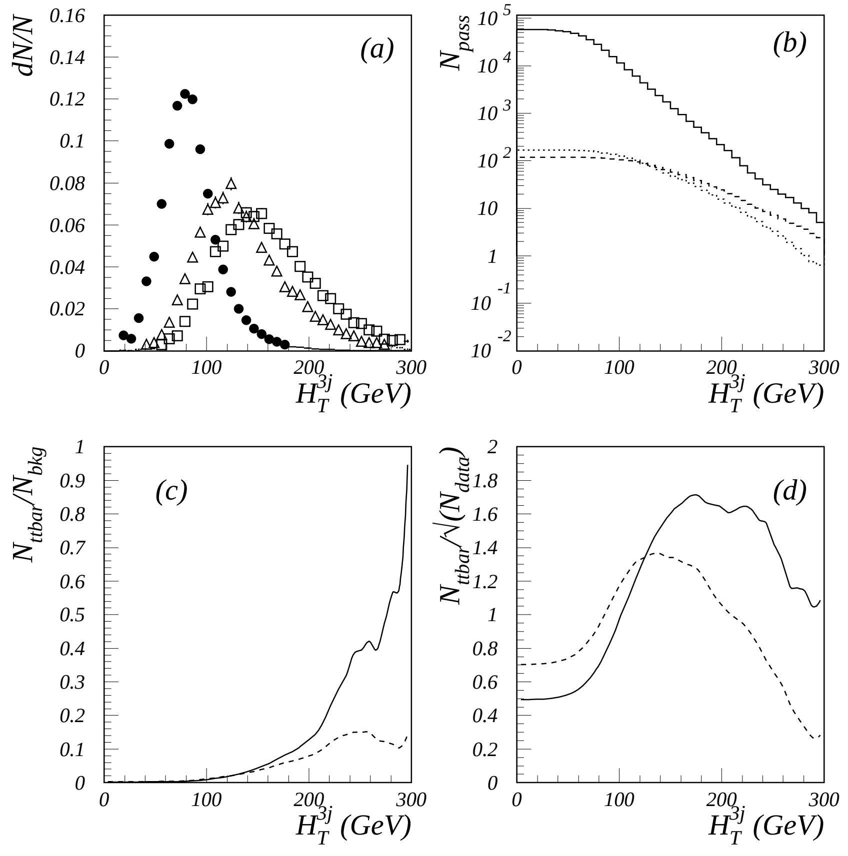

Figure 5.1: Characteristics of H_T^{3j}.

(a) Distribution in H_T^{3j} for DØ data (circles), and for ISAJET $t\bar{t}$ Monte Carlo with m_t of 160 GeV/c^2 (triangles) and 200 GeV/c^2 (squares), with all distributions normalized to the same area.

(b) Number of events above threshold as a function of threshold on H_T^{3j}, for DØ data (solid line) and for $t\bar{t}$ Monte Carlo with m_t of 160 GeV/c^2 (dotted line) and 200 GeV/c^2 (dashed line).

(c) Ratio of signal to background as a function of threshold on H_T^{3j}, for m_t of 160 GeV/c^2 (dashed line) and 200 GeV/c^2 (solid line). Background is estimated by $N_{\rm bkg} = N_{\rm data} - N_{t\bar{t}}$.

(d) Statistical significance of the signal, defined as $N_{t\bar{t}}/\sqrt{N_{\rm data}}$, as a function of threshold on H_T^{3j}, for m_t of 160 GeV/c^2 (dashed line) and 200 GeV/c^2 (solid line).

signal-to-background ratio for different top masses, displayed in Fig. 5.2(c), is due solely to the dependence of the $t\bar{t}$ cross section on m_t. We note from Fig. 5.2(c) that $\mathcal{C}$ is a far weaker discriminator between signal and background than H_T^{3j}: its peak value in signal-to-background ratio is much lower. However, as we will discuss in Section 5.3.5, $\mathcal{C}$ is useful in corrrelation with other parameters.

5.3.3 Aplanarity

The quantity aplanarity, derived from the momentum tensor, is a standard event-shape parameter used in analysis of data at e^+e^- colliders [91]. It has also been used in the analysis of $t\bar{t} \to$ lepton+jets events at DØ [2]. The components ($\mathcal{M}_{\alpha\beta}$) of the momentum tensor are given by:

$$\mathcal{M}_{\alpha\beta} = \sum_{i=1}^{N} p_\alpha(i) p_\beta(i), \tag{5.4}$$

where N is the number of jets in the event with $|\eta| < 2$ and $E_T > 10$ GeV, and α, β refer to the components of the three-momentum vectors of each jet. This tensor represents the momentum flow in an event as an ellipsoid in three-momentum space. The eigenvalues of the tensor (which are proportional to the lengths of the principal axes of the ellipsoid) roughly describe the shape of the momentum flow.

To remove the dependence on total momentum, we normalize the eigenvalues so that their sum is 1. Denoting the normalized eigenvalues by $Q_1 \leq Q_2 \leq Q_3$, we define the quantity aplanarity ($\mathcal{A}$) as:

$$\mathcal{A} = \frac{3}{2} Q_1. \tag{5.5}$$

Because three-momenta are used, the momentum tensor is not Lorentz invariant. It is therefore necessary to specify a reference frame for the calculation. The

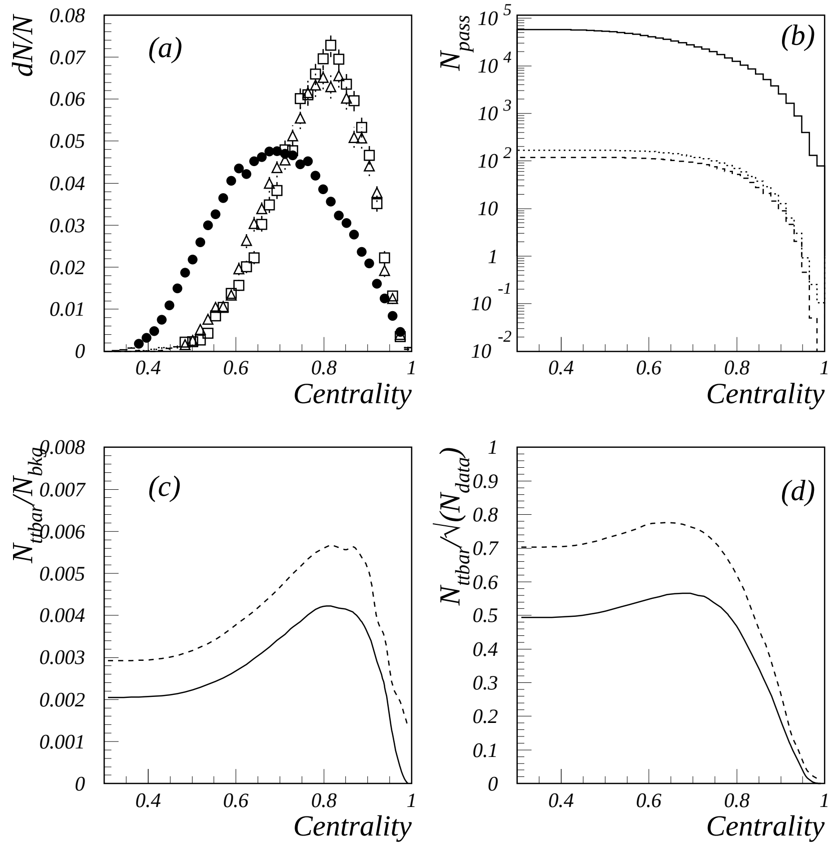

Figure 5.2: Characteristics of $\mathcal{C}$.
(a) Distribution in $\mathcal{C}$ for DØ data (circles), and for ISAJET $t\bar{t}$ Monte Carlo with m_t of 160 GeV/c^2 (triangles) and 200 GeV/c^2 (squares), with all distributions normalized to the same area.
(b) Number of events above threshold as a function of threshold on $\mathcal{C}$, for DØ data (solid line) and for $t\bar{t}$ Monte Carlo with m_t of 160 GeV/c^2 (dotted line) and 200 GeV/c^2 (dashed line).
(c) Ratio of signal to background as a function of threshold on $\mathcal{C}$, for m_t of 160 GeV/c^2 (dashed line) and 200 GeV/c^2 (solid line). Background is estimated by $N_{\rm bkg} = N_{\rm data} - N_{t\bar{t}}$.
(d) Statistical significance of the signal, defined as $N_{t\bar{t}}/\sqrt{N_{\rm data}}$, as a function of threshold on $\mathcal{C}$, for m_t of 160 GeV/c^2 (dashed line) and 200 GeV/c^2 (solid line).

standard choices are the lab frame or the center-of-momentum frame (of the jets). In the multijet sample, we find that the choice makes little difference; for simplicity, we use the lab frame.

Characteristics of $\mathcal{A}$ are shown in Fig. 5.3, again using the format of Fig. 5.1. In Fig. 5.3(a), we see that, just as for centrality, the shape of the distribution in $\mathcal{A}$ is independent of the mass of the top quark. Fig. 5.3(c) shows that $\mathcal{A}$ is a more powerful discriminator than $\mathcal{C}$, but not as powerful as H_T^{3j}, in distinguishing between signal and background.

5.3.4 Average Jet Count

Beyond requiring at least six jets, the number of jets in an event (above some threshold in E_T) is of limited value in discriminating between background and $t\bar{t} \rightarrow$ all-jets events (see Fig. 4.4(a)). A jet-counting parameter that includes information on the E_T of the jets—for instance, by averaging over multiple thresholds in E_T—can provide additional discrimination. The use of such a parameter was inspired by the work of F. Tkachov [92], but the formulation is our own [82].

We have formulated an average jet-count parameter, N_{jets}^A, which is defined as:

$$N_{jets}^A = \frac{\displaystyle\int_{15}^{45} E_T^{thr}\, N(E_T^{thr})\, dE_T^{thr}}{\displaystyle\int_{15}^{45} E_T^{thr}\, dE_T^{thr}}, \tag{5.6}$$

where $N(E_T^{thr})$ is the number of jets in the event with $|\eta| < 2$ and $E_T > E_T^{thr}$. This formula yields the E_T-weighted average of $N(E_T^{thr})$ over thresholds ranging from 15 to 45 GeV. The choice for the range of thresholds is motivated by the range of typical jet E_T expected in $t\bar{t} \rightarrow$ all-jets events.

The discriminating power of N_{jets}^A arises from the fact that QCD background

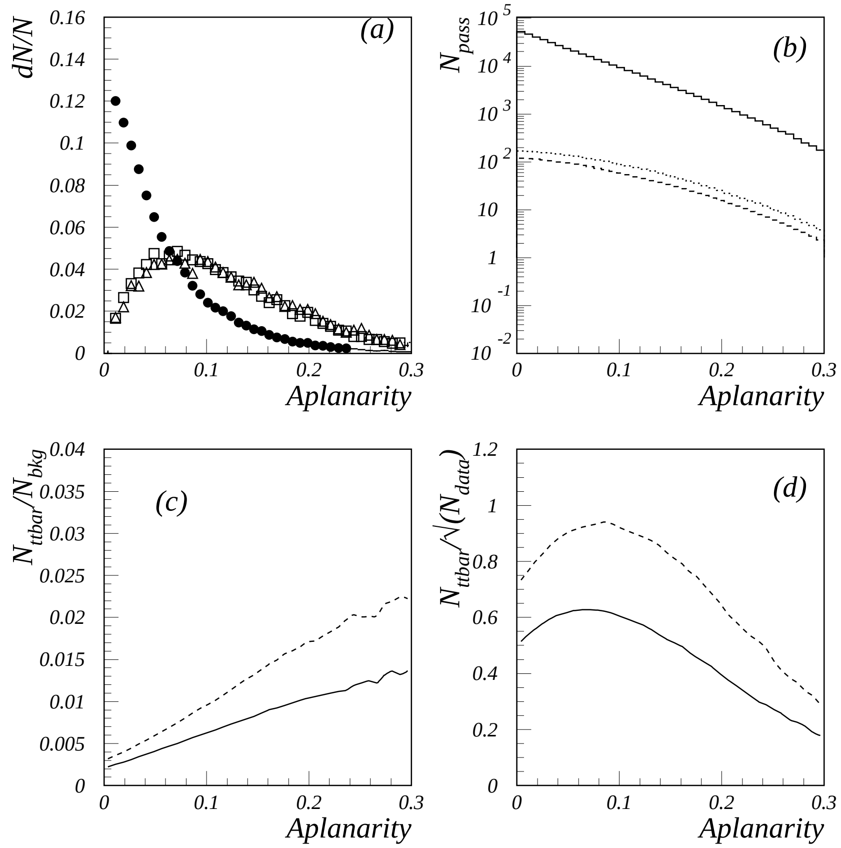

Figure 5.3: Characteristics of $\mathcal{A}$.

(a) Distribution in $\mathcal{A}$ for D0 data (circles), and for ISAJET $t\bar{t}$ Monte Carlo with m_t of 160 GeV/c^2 (triangles) and 200 GeV/c^2 (squares), with all distributions normalized to the same area.

(b) Number of events above threshold as a function of threshold on $\mathcal{A}$, for D0 data (solid line) and for $t\bar{t}$ Monte Carlo with m_t of 160 GeV/c^2 (dotted line) and 200 GeV/c^2 (dashed line).

(c) Ratio of signal to background as a function of threshold on $\mathcal{A}$, for m_t of 160 GeV/c^2 (dashed line) and 200 GeV/c^2 (solid line). Background is estimated by $N_{\mathrm{bkg}} = N_{\mathrm{data}} - N_{t\bar{t}}$.

(d) Statistical significance of the signal, defined as $N_{t\bar{t}}/\sqrt{N_{\mathrm{data}}}$, as a function of threshold on $\mathcal{A}$, for m_t of 160 GeV/c^2 (dashed line) and 200 GeV/c^2 (solid line).

processes tend to involve a hard scatter that produces two or three jets with large E_T; the remaining jets come from gluon radiation, which tends to produce jets with lower E_T than the typical jets expected in $t\bar{t}$ decays. The use of a single E_T threshold in jet counting reduces the information available to quantify the jet multiplicity in an event. Because N_{jets}^A is an average over a range of thresholds, it provides sensitivity to the E_T spectrum of the jets within an event.

Characteristics of N_{jets}^A are shown in Fig. 5.4, again using the format of Fig. 5.1. The distributions in N_{jets}^A, shown in Fig. 5.4(a), indicate that this parameter is indeed a powerful discriminator. In fact, as we can see by comparing Fig. 5.4(d) to Fig. 5.1(d), N_{jets}^A is about as powerful as H_T^{3j}. We note that, like H_T^{3j}, this parameter depends on m_t.

5.3.5 Comparison of Parameters

Here, we discuss briefly the relative merits of the four parameters and some of the correlations among them. A more detailed study of these issues is presented in Ref. [82].

We use parts (c) and (d) of Figs. 5.1–5.4 to compare the parameters. We see that for a top mass of 200 GeV/c^2, H_T^{3j} and N_{jets}^A are clearly the most powerful discriminators between $t\bar{t}$ signal and background. For an appropriate choice of threshold, either of these parameters can be used to improve the statistical significance of the signal to about 1.5 standard deviations (assuming that $\sqrt{N_{\rm data}}$ represents a standard deviation). For lower top mass (160 GeV/c^2), their advantage is smaller, but they still remain the strongest discriminators.

Aplanarity and centrality are less powerful, but they are nevertheless useful discriminators, as we will see when we examine the correlations among the parameters. For instance, shown in Fig. 5.5 is the distribution in the $\mathcal{A}$-H_T^{3j} plane, for

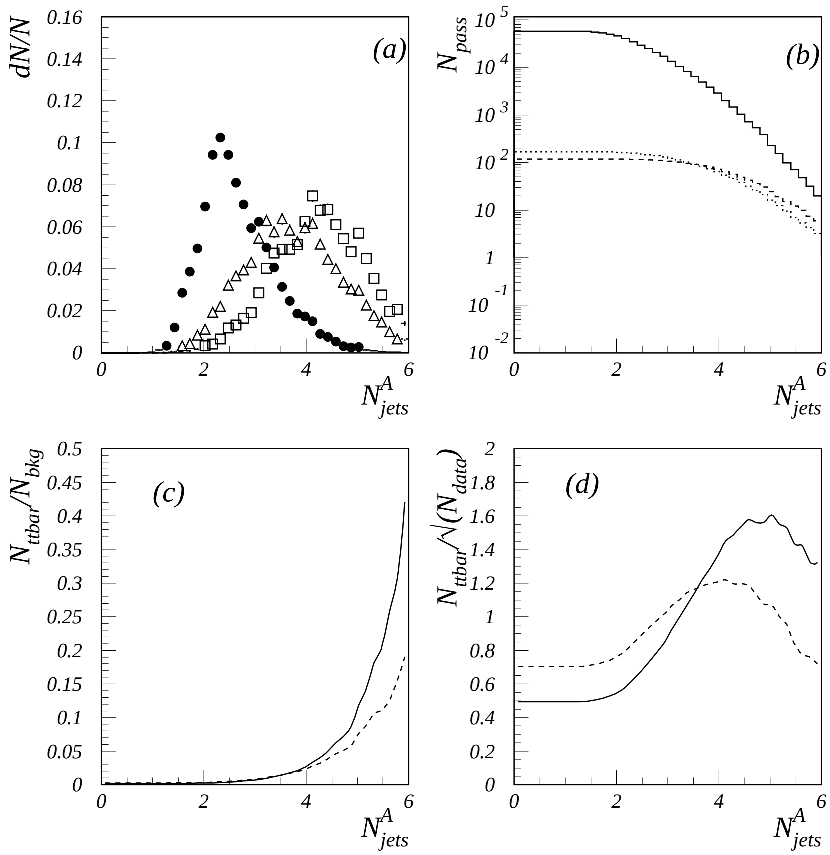

Figure 5.4: Characteristics of N^A_{jets}.
(a) Distribution in N^A_{jets} for DØ data (circles), and for ISAJET $t\bar{t}$ Monte Carlo with m_t of 160 GeV/c^2 (triangles) and 200 GeV/c^2 (squares), with all distributions normalized to the same area.
(b) Number of events above threshold as a function of threshold on N^A_{jets}, for DØ data (solid line) and for $t\bar{t}$ Monte Carlo with m_t of 160 GeV/c^2 (dotted line) and 200 GeV/c^2 (dashed line).
(c) Ratio of signal to background as a function of threshold on N^A_{jets}, for m_t of 160 GeV/c^2 (dashed line) and 200 GeV/c^2 (solid line). Background is estimated by $N_{\rm bkg} = N_{\rm data} - N_{t\bar{t}}$.
(d) Statistical significance of the signal, defined as $N_{t\bar{t}}/\sqrt{N_{\rm data}}$, as a function of threshold on N^A_{jets}, for m_t of 160 GeV/c^2 (dashed line) and 200 GeV/c^2 (solid line).

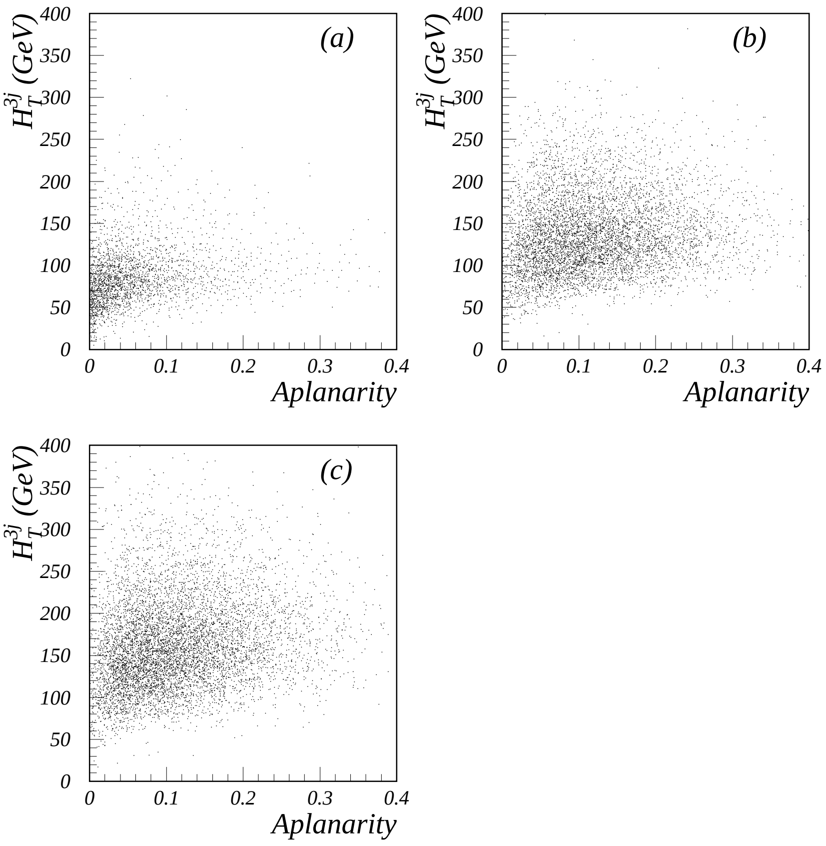

Figure 5.5: Distribution in the $\mathcal{A}$-H_T^{3j} plane, for DØ data (a), and for ISAJET $t\bar{t}$ Monte Carlo with m_t of 160 GeV/c^2 (b) and 200 GeV/c^2 (c).

DØ data (mainly background) and for ISAJET $t\bar{t}$ Monte Carlo with m_t of 160 and 200 GeV/c^2. Figure 5.1(d) suggests that requiring $H_T^{3j} > 170$ GeV would maximize $N_{t\bar{t}}/\sqrt{N_{\rm data}}$ for m_t of 200 GeV/c^2. This requirement would reject most of the background. However, Fig. 5.5 suggests that if we reduce the H_T^{3j} threshold to only about 140 GeV, but impose a threshold requirement of $\mathcal{A} > 0.05$, we would achieve comparable background rejection with higher acceptance for signal.

We have also examined correlations between $\mathcal{A}$ and $\mathcal{C}$, as shown in Fig. 5.6. We

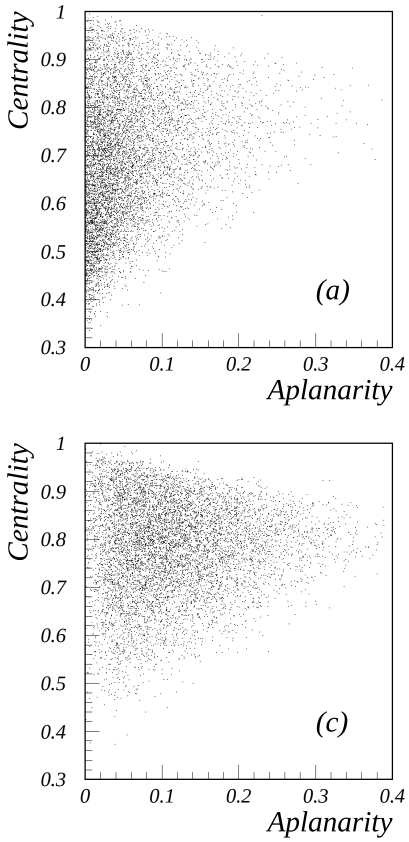

Figure 5.6: Distribution in the $\mathcal{C}$-$\mathcal{A}$ plane, for DØ data (a), and for ISAJET $t\bar{t}$ Monte Carlo with m_t of 160 GeV/c^2 (b) and 200 GeV/c^2 (c).

see that imposing a requirement such as $\mathcal{C} > 0.7$ allows us to relax the threshold on $\mathcal{A}$, thereby improving the acceptance for signal while maintaining equivalent background rejection. In addition, imposing requirements on $\mathcal{A}$ and $\mathcal{C}$ allows us to relax the requirements on H_T^{3j} and N_{jets}^A, thereby improving our sensitivity to $t\bar{t}$ at lower mass. Thus, although $\mathcal{A}$ and $\mathcal{C}$ are not very powerful discriminators, they can be quite useful in selecting $t\bar{t}$ events.

Finally, the correlation between the most sensitive parameters, H_T^{3j} and N_{jets}^A, is

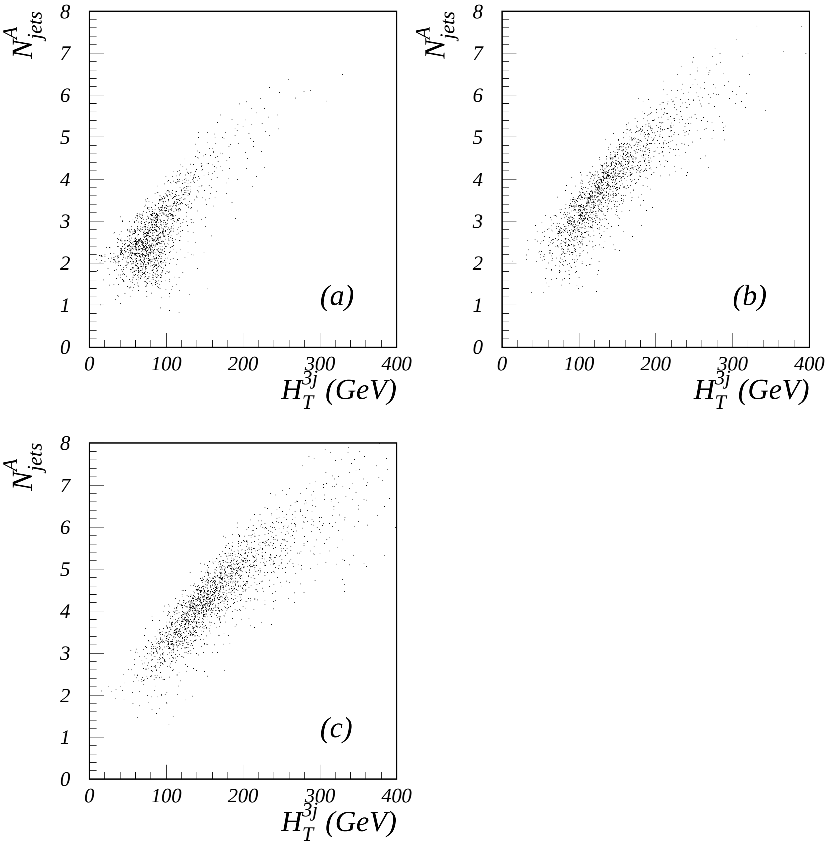

Figure 5.7: Distribution in the H_T^{3j}-N^A_{jets} plane, for DØ data (a), and for ISAJET $t\bar{t}$ Monte Carlo with m_t of 160 GeV/c^2 (b) and 200 GeV/c^2 (c).

worth noting. Scatter plots in these variables for data and $t\bar{t}$ Monte Carlo are shown in Fig. 5.7. We see that these parameters are strongly correlated, which is to be expected, given their respective definitions. Nevertheless, imposing requirements on both of these parameters appears to be advantageous [75, 82].

The method used to optimize selection criteria for the search for $t\bar{t} \rightarrow$ all-jets using all four of these parameters will be discussed in Chapter 6.

5.4 Muon-Tagging

In addition to kinematic properties, we will also use the presence of a heavy quark in the $t\bar{t}$ final state to distinguish signal from background. As we described in Chapter 1, every $t\bar{t}$ event contains two b quarks. Many $t\bar{t}$ events produce c quarks as well, either from decays of the W bosons or from cascade decays of the b quarks. Only a small fraction of background processes produce heavy quarks. At DØ, heavy-quark jets are tagged by requiring the presence of a nearby muon ("muon-tagging"). This is a well established procedure in studies of $t\bar{t}$ production using lepton+jets final states [2, 57, 93]. Muon-tagging improves background rejection, and sources of background from light quarks and gluons can be estimated in a straightforward manner.

The requirements used to select muon-tags for our analysis were described in Section 3.4. As was mentioned there, muon-tags are required to have $p_T > 4$ GeV/c, and to be located within $\Delta\mathcal{R} = 0.5$ of a jet. Here, we describe how the rates for muon-tagging in signal and background events can be determined.

5.4.1 Muon-Tagging Rate for $t\bar{t}$ Events

About 10% of the heavy quarks decay semileptonically to a muon (and other particles, including ν_μ). When all contributions from decays of b quarks and $W \to c$ decays are considered, then almost half of all $t\bar{t} \to$ all-jets events are expected to yield at least one muon from heavy quark decays [94]. The efficiency of the criteria of Section 3.4 for identifying such muons is about 40% [57]. Consequently, we expect to find a muon that tags a jet in about 20% of signal events.

We have also calculated the efficiency for muon-tagging in $t\bar{t} \to$ all-jets events by applying to the ISAJET Monte Carlo samples the criteria for identifying muon-tags (see Section 3.4). For m_t of 160 to 200 GeV/c^2, the efficiency is found to be

$(21 \pm 1)\%$, consistent with the estimated 20% value for the acceptance.

5.4.2 Muon-Tagging Rate for Background

The characteristic muon-tagging rate for background was derived from the generic data sample. We parametrized the probability that a given jet was tagged as a function of the E_T of the jet. By summing this probability over all jets in an event, we found the probability that the event would have at least one muon-tag.

We considered data from Run Ia and Run Ib separately in order to ensure that any effect due to changes in the muon system between the two runs was handled properly. A drop in efficiency of the muon chambers between Run Ia and Run Ib, due to aging of the chambers in the high-rate environment, was observed in the analysis of data for the lepton+jets channels [95]. The change is especially pronounced in the EF region ($1 < |\eta| < 1.7$), but since we have restricted muon-tags for both runs to the CF region ($|\eta| < 1$), the net effect on our data is small.

Figures 5.8(a) and 5.9(a) show, for Run Ia and Run Ib, respectively, the distribution in E_T values for jets in the generic data sample with $|\eta| < 1$ and $E_T >$ 10 GeV, with and without the requirement of having a muon-tag. Part (b) of each figure shows the corresponding "tagging rate" for jets (*i.e.*, the ratio of the number of tagged jets to the total number of jets) in each bin of E_T. In order to minimize the statistical fluctuations at large E_T, we have used logarithmic binning in E_T.

We parametrized the tagging rate as a function of jet E_T, using the form

$$P_{\mu\text{-tag}} = A + B \log_{10}(E_T), \qquad (5.7)$$

where $P_{\mu\text{-tag}}$ is the tagging rate for jets shown in Figs. 5.8(b) and 5.9(b). From a fit to the generic data sample from Run Ia, we obtained $A = -0.00601 \pm 0.00076$ for the intercept, and $B = 0.00337 \pm 0.00024$ for the slope of the dependence. For

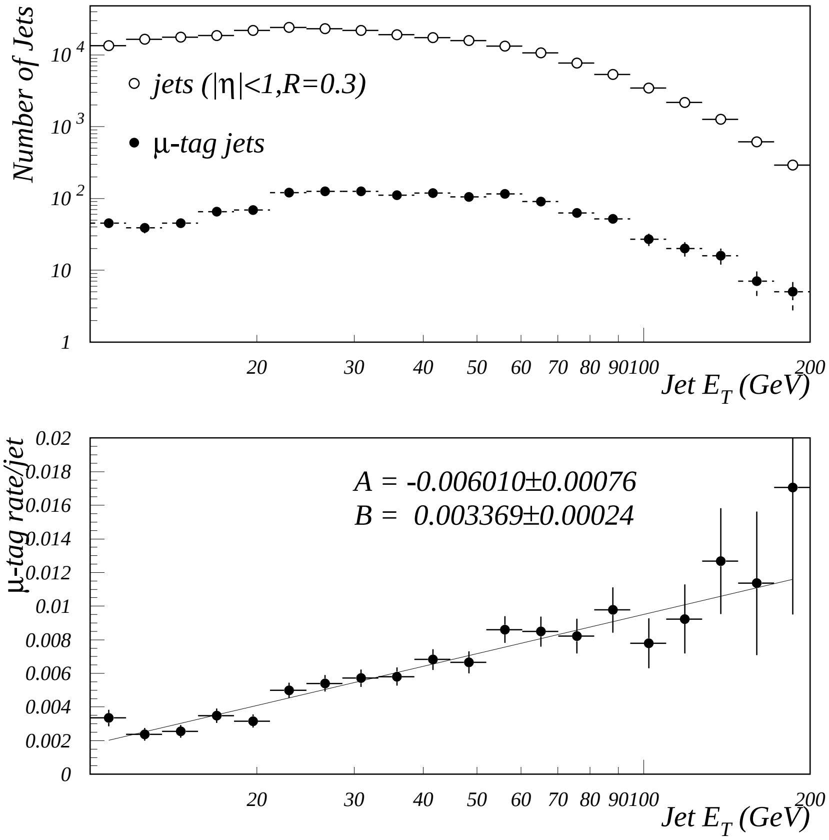

Figure 5.8: Muon-tagging rate for Run Ia, using the generic data sample. (a) Distribution in E_T for jets with $|\eta| < 1$ and $E_T > 10$ GeV (open circles) and for the subset of those jets that have a muon tag (solid circles), and (b) the ratio of tagged jets to all jets in each E_T bin. In part (b), results are shown of a fit to $P_{\mu\text{-tag}} = A + B\log_{10}(E_T)$.

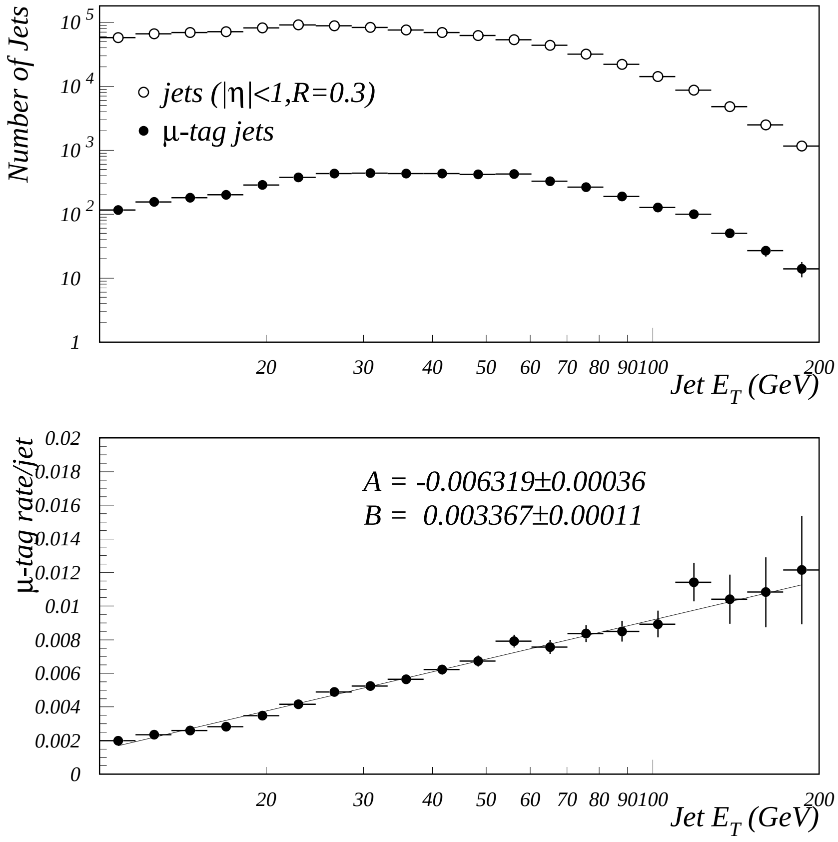

Figure 5.9: Muon-tagging rate for Run Ib, using the generic data sample. (a) Distribution in E_T for jets with $|\eta| < 1$ and $E_T > 10$ GeV (open circles) and for the subset of those jets that have a muon tag (solid circles), and (b) the ratio of tagged jets to all jets in each E_T bin. In part (b), results are shown of a fit to $P_{\mu\text{-tag}} = A + B\log_{10}(E_T)$.

Run Ib, the fit parameters were $A = -0.00632 \pm 0.00036$ and $B = 0.00337 \pm 0.00011$. The results for the two parts of the run are consistent with each other, the average probability of finding a muon that tags any given jet being about 0.5% per jet. We therefore expect that about 3–4% of background events will have a muon-tag. Comparing this to the 20% of $t\bar{t}$ events expected to have a tag, we see that requiring a muon-tag should improve background rejection by about a factor of five.

To estimate the number of muon-tagged events in a multijet data sample, we used the E_T of the jets in each event and the parametrization of $P_{\mu\text{-tag}}$ given in Equation 5.7. The expected number of muon-tagged events in a sample is given by:

$$N_{\text{tag}}(pred) = \sum_{events} \sum_{jets} P_{\mu\text{-tag}}, \tag{5.8}$$

where the sum over jets includes only jets with $|\eta| < 1$ and $E_T > 10$ GeV, and the sum over events includes only the events remaining in the sample after all requirements except that for the muon-tag have been imposed.

Our estimate for the expected number of muon-tags assumes that the heavy quark content in the data is not affected significantly by the kinematic selection criteria (using H_T^{3j}, $\mathcal{A}$, $\mathcal{C}$, and N_{jets}^{A}). Of course, this assumption is only correct if the $t\bar{t}$ component of the sample is negligible. However, because we will impose selection criteria designed to enrich the $t\bar{t}$ fraction, we expect the number of muon-tagged events remaining in the sample (after imposing kinematic criteria) to exceed the number predicted for background alone (Equation 5.8). A significant excess would constitute possible evidence for $t\bar{t}$ production.

To estimate the uncertainty in the predicted number of background muon-tagged events, we allowed the parameters A and B to vary within their uncertainties. Using the search sample of data, which contains a large number of events and a small (about 1% after imposing the muon-tag requirement) expected contribution from $t\bar{t}$ production, we found that the predicted number of events with a muon-tag varies by 5%, and assigned this as the uncertainty in the background prediction due to uncertainty in the fit of the tagging rate. We also found that by using the central values of A and B from the generic sample, we could predict the number of events in the search sample that had a muon-tag to within this 5% uncertainty.

In addition, we examined the dependence of the tagging rate on the kinematic parameters of Section 5.3. Figure 5.10 shows the distribution in each of these parameters for events with a muon-tag from the Run Ib search sample. For each of the four parameters, the prediction appears to describe the observed distribution rather well. For Run Ia, the quality of the prediction is similar.

We have also looked for evidence that hadrons from high-momentum jets pass through the iron, thereby simulating muons. As noted in Chapter 2, the calorimeter and muon system contain many interaction lengths of material in order to prevent this occurrence. However, because we use kinematic criteria that tend to select events with high-E_T jets, it is possible that such hadronic "punchthrough" can be larger in our final candidate sample than in the generic sample, in which case the background would be underestimated. (We are not concerned with muons produced in the decays of pions and kaons in jets, as this contribution should already be modeled by the background prediction.) This issue has been studied extensively, and the effect has been found to be negligible [57, 96].

Due to sources other than $t\bar{t}$ production, the imposition of our kinematic selection requirements may affect the b-quark content of the selected events relative to that of the generic sample. This would also cause the background estimate of Equation 5.8 to be too low. Figure 5.10 does not show evidence of such an effect, and additional studies [75] using Monte Carlo models of QCD b-quark production indicate that this causes less than 10% of an effect, which we will use for ascribing

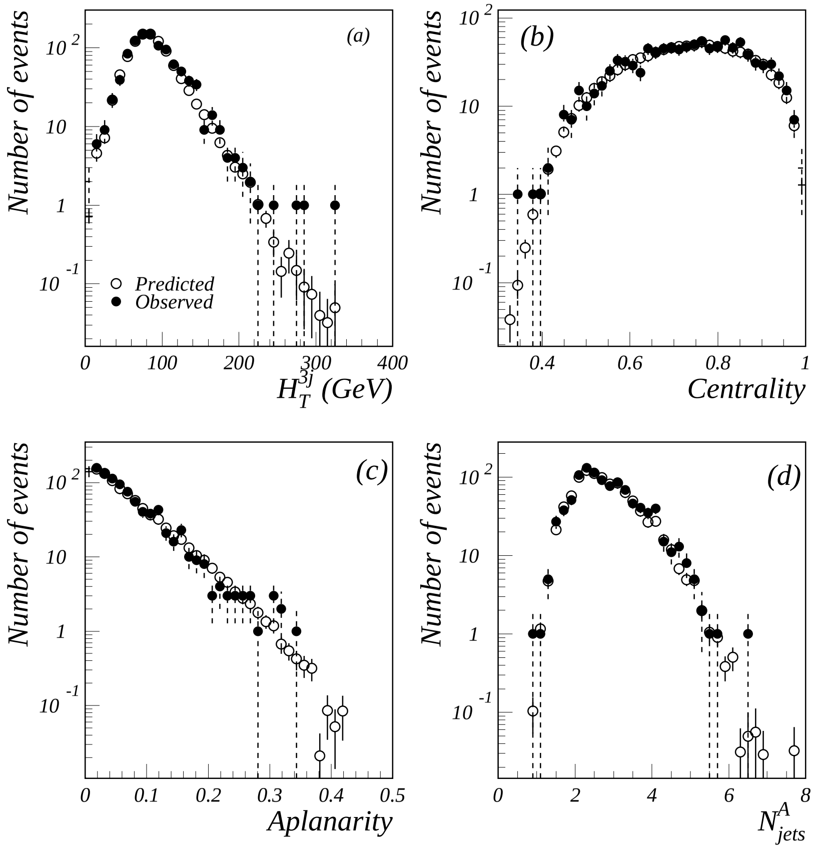

Figure 5.10: Predicted number (open circles) and observed number (solid circles) of events with a muon tag in the search sample from Run Ib, shown as a function of H_T^{3j}, $\mathcal{C}$, $\mathcal{A}$, and N_{jets}^{A}, respectively, in (a), (b), (c), and (d).

a systematic uncertainty in our background estimates.

Finally, we have studied the effect of the Main Ring on the muon-tagging rate. As we noted in Chapter 4, events that occurred during periods of intense Main-Ring activity were not rejected by the multijet trigger, and our quality requirements (see Section 4.2) may not have removed them all. We have therefore examined each of the events that satisfied our final selection criteria (to be defined in Section 6.1) for evidence of contamination from interactions in the Main Ring, but found no such problem. In addition, we have examined the muon-tagging rate to see whether it depends on the status of the Main Ring, by comparing the muon-tag rate for events that occurred during the MRBS_LOSS or MICRO_BLANK[*] intervals, when effects from interactions in the Main Ring are most likely, to the rate for events that occurred outside those intervals. We conclude that the uncertainty due to effects from the Main Ring is 0.6%.

---

[*] See Section 2.2.5.

Chapter 6

Selection of Candidate Events

In the previous chapter we described the kinematic parameters that can be used to distinguish $t\bar{t}$ events from background, and a way of estimating the expected background when a muon-tag is required. Here we apply selection criteria to the search sample, using both the kinematic properties and muon-tags, in order to determine whether a contribution from $t\bar{t}$ production is present in the data.

6.1 Optimization of Selection Criteria

To define optimal selection criteria, we must again use data to model the background. Because it is desirable to optimize such criteria using a data sample that is statistically independent of the data that will be used in the search, we chose to divide the search sample into two parts. We randomly selected 9,766 events from the search sample (as defined in Section 4.3), divided between Run Ia and Run Ib in proportion to their respective luminosities, and designated this as the "background-study" sample. This sample was used to define the optimal selection criteria. The remaining 48,459 events were designated the "final" data sample, and the search for a $t\bar{t}$ signal was subsequently performed using this sample, which corresponds to an integrated luminosity of 48.6 pb^{-1}.

Each of the events in the background-study sample was assigned a weight proportional to its probability of having a muon-tag, as determined from the background tagging function (Equation 5.8). The proportionality constant was chosen to make the sum of the weights for all events in the background-study sample (satisfying some given set of criteria) equal the expected number of muon-tagged background events in the final data sample (satisfying the same criteria).

The signal sample consisted of 8,880 ISAJET $t\bar{t} \rightarrow$ all-jets events that satisfied all the requirements used to define the search sample. We chose a top mass of 180 GeV/c^2 for the optimization procedure so that the selection requirements would be efficient over the full range of likely values for the top mass. Each signal event was assigned a weight of 0.2 (reflecting the approximate probability of finding a muon-tag in a $t\bar{t}$ event), which was multiplied by a constant factor that made the sum of the weights for all events (satisfying some given set of criteria) equal the number of muon-tagged $t\bar{t}$ events expected in the final data sample. A 44% branching ratio for $t\bar{t} \rightarrow$ all-jets and the value of the total $t\bar{t}$ cross section measured by DØ were, as usual, assumed in the analysis. In order to improve the statistics in the optimization procedure, we did not require a muon-tag in either the signal or background-study samples.

We optimized a set of criteria by requiring that the values of each of the four parameters H_T^{3j}, $\mathcal{A}$, $\mathcal{C}$, and N_{jets}^{A} exceed some given thresholds. The possible values of the thresholds were taken from an "importance-sampled" grid in the four-parameter phase space [75, 82]. For any event (X), in either the background-study or the signal sample, we found the sum of the weights for events in the signal sample and the sum of the weights for events in the background-study sample that had values of all four parameters greater than the values in event X. The optimization involved performing this procedure for all events in both samples. We could then identify a set of selection requirements for the four parameters that, for example, achieved maximum significance for signal, maximum background rejection at some fixed efficiency for signal, or some other such choice.

The results obtained from testing some possible sets of thresholds are shown in Fig. 6.1, where we plot the expected number of muon-tagged signal events ($N_{t\bar{t}}$) vs. the expected number of muon-tagged background events ($N_{\rm bkg}$) for each set of thresholds. The numbers of events correspond to an integrated luminosity of 48.6 $\rm pb^{-1}$. The upper edge of the envelope—where expected signal is maximized for any given level of background—defines a family of optimal sets of threshold values for the kinematic parameters. Points below this edge correspond to combinations of thresholds that yield lower ratios of signal to background and therefore would not be optimal for selecting $t\bar{t}$ events for further study. Our selection criteria for the search sample excluded possibilities in this region, and the optimization procedure did not consider sets of parameters that had poor combinations of threshold values.[*]

In Fig. 6.2, we show the points along the optimal boundary for the region of $N_{\rm bkg} < 85$. We find that this boundary can be characterized roughly by $N_{t\bar{t}} \approx 1.4\sqrt{N_{t\bar{t}} + N_{\rm bkg}}$, which represents the presence of a $t\bar{t}$ signal with a statistical significance of 1.4 standard deviations. The corresponding contour is shown as a dashed line.

We have chosen two sets of kinematic criteria corresponding to two points along the optimal boundary to be used for selecting candidate events. These points have been labeled as "Set I" and "Set II" in Fig. 6.2. The criteria of Set I were chosen because they produced an expected signal-to-background ratio that was

---

[*] Threshold values below $H_T^{3j} = 50$ GeV, $\mathcal{C} = 0.4$, $N_{jets}^{A} = 1.5$, and $\mathcal{A} = 0.02$ were not considered.

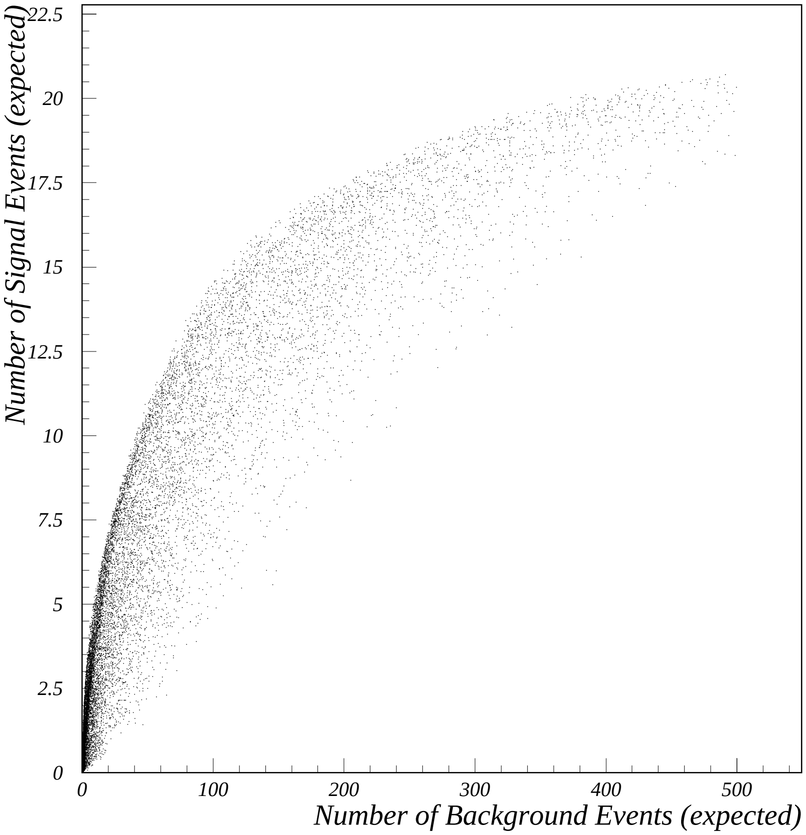

Figure 6.1: Output from the grid-search algorithm. Shown are predictions for the number of muon-tagged background events and the number of muon-tagged signal events expected for an integrated luminosity of 48.6 pb^{-1}, for different values of thresholds on the chosen kinematic parameters. Background is modeled by a subset of the DØ data, and signal is modeled using ISAJET Monte Carlo with m_t of 180 $\mathrm{GeV/c}^2$. Each point corresponds to a different choice of thresholds for the input parameters.

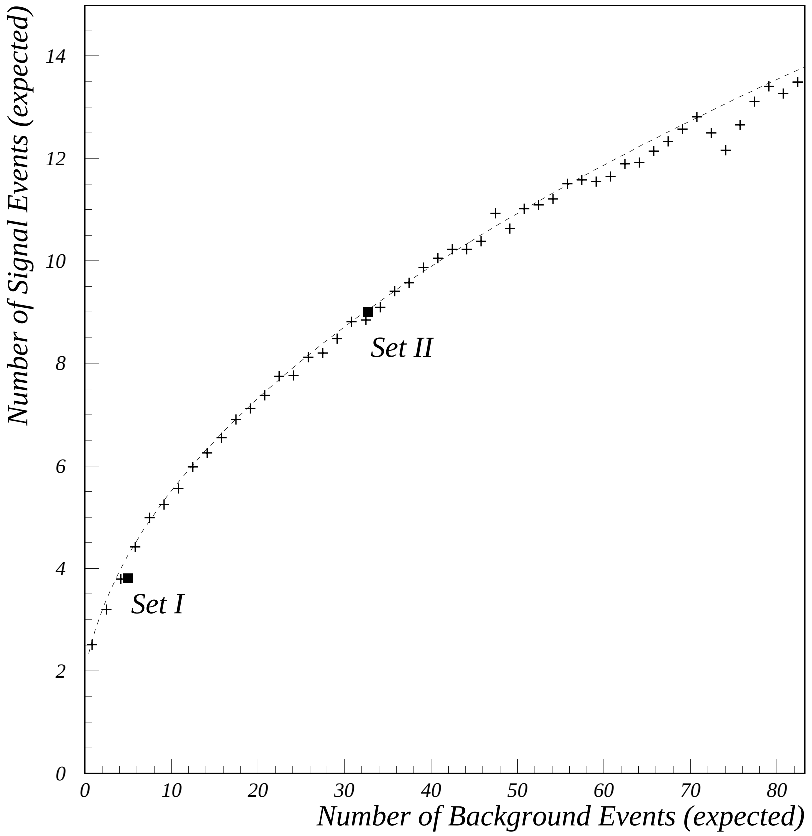

Figure 6.2: Optimal boundary from the grid search. For each level of background, we have plotted the maximum expected signal attainable using the grid-search algorithm. The dashed line represents a contour of constant statistical significance (see text). Our two chosen sets of criteria are indicated as Set I and Set II.

Table 6.1: Threshold values and expected results for our two sets of selection criteria.

	Set I	Set II
Thresholds:		
H_T^{3j} (GeV)	144.7	137.6
$\mathcal{C}$	0.739	0.698
N_{jets}^{A}	3.32	3.10
$\mathcal{A}$	0.131	0.048
Acceptance ($\varepsilon_{\text{all-jets}}$):		
m_t = 160 GeV/c^2	0.0134 ± 0.0033	0.0338 ± 0.0078
m_t = 180 GeV/c^2	0.0218 ± 0.0052	0.0526 ± 0.0121
m_t = 200 GeV/c^2	0.0307 ± 0.0074	0.0721 ± 0.0166
Expected $N_{t\bar{t}}$:		
m_t = 160 GeV/c^2	3.10	7.82
m_t = 180 GeV/c^2	3.81	9.23
m_t = 200 GeV/c^2	4.20	9.87
Expected N_{bkg}	4.99	32.7

near unity, with several events expected from signal. The criteria of Set II were less restrictive, thereby providing a larger sample of candidate events that still had adequate sensitivity to contributions from $t\bar{t}$ production. The values of the thresholds for the kinematic parameters for both sets are listed in Table 6.1, along with the expected yields for signal and background. The acceptance ($\varepsilon_{\text{all-jets}}$) of these criteria for selecting $t\bar{t} \rightarrow$ all-jets events is also listed for top masses of 160, 180 and 200 GeV/c^2.

In order to check that our results do not depend strongly on the particular sets of chosen thresholds, we have studied six other sets of criteria that correspond to points along the optimal boundary. (Appendix A provides details of this study.) Other studies that demonstrate the reliability of the grid-search algorithm for selecting optimal criteria are described in Ref. [75].

The uncertainties listed in Table 6.1 for $\varepsilon_{\text{all-jets}}$ include a statistical uncertainty of 5% for Set I and 3% for Set II. This corresponds to the number of events in the Monte Carlo that satisfied the selection criteria. In addition, several sources of systematic uncertainty have been investigated, as described below.

One major source of systematic uncertainty is the relative energy scale for jets between data and Monte Carlo. The absolute energy scale is not particularly relevant for our search. However, if jets in the Monte Carlo events have substantially larger (or smaller) energies than corresponding jets in the data, then the acceptance for selecting $t\bar{t}$ events will be miscalculated. The uncertainty in the relative scale is a major contributor to the uncertainty in $\varepsilon_{\text{all-jets}}$. The corrections of CAFIX are only reliable to 10% accuracy, and varying the energy scale in the Monte Carlo by this amount suggests a 16% uncertainty in acceptance for the chosen criteria.

Another important issue is how well the ISAJET generator models the physics of $t\bar{t}$ production and decay. To estimate the effect of uncertainty in the model, we compared the acceptance for a given set of criteria using ISAJET events to that obtained using HERWIG. We found a systematic uncertainty of 13% due to differences between the generators at the parton level. We also found a 10% uncertainty due to the reliability with which GEANT models detector performance and the variation in true detector performance with time.

We have also considered the possibility that an event with a muon-tag may be less likely to satisfy the kinematic selection requirements because part of the tagged jet's initial energy was transferred to the muon and the (undetected) ν_μ. If this effect were significant, we would expect the muon-tagging rate for $t\bar{t}$ events to depend on the specifics of the kinematic criteria. We examined the efficiency of the muon-tag requirement for $t\bar{t}$ events over a range of possible kinematic criteria and found no such effect. Consequently, we do not regard this as a significant source of uncertainty in $\varepsilon_{\text{all-jets}}$.

Table 6.2: Sources of uncertainty in $\varepsilon_{\text{all-jets}}$.

	Size of effect	
Source of Uncertainty	Set I	Set II
Energy scale	16%	15%
Model accuracy	13%	13%
Detector response	10%	10%
Trigger model (§5.1)	5%	5%
Statistical uncertainty	5%	4%
Total uncertainty	24%	23%

The contributions to the uncertainty in $\varepsilon_{\text{all-jets}}$ are summarized in Table 6.2. The total uncertainty was obtained by adding these effects in quadrature.

To measure the total cross section for $t\bar{t}$ production accurately, it is important to account for any contributions that may be present in the final data sample from $t\bar{t}$ decay channels other than all-jets. In Table 6.3, we list $\sum \varepsilon \times \text{BR}$, that is, the acceptance for all $t\bar{t}$ decay modes, including all-jets, and the corresponding expected yield of $t\bar{t}$ events. Comparing these values to those predicted for only all-jets decays (Table 6.1), we see that about 15–18% of the total yield in our all-jets sample can be attributed to channels other than all-jets. About 40% of these additional events are from the τ+jets decay mode, while the rest are from e+jets and μ+jets events for which the lepton did not satisfy the identification requirements for searches in those channels.

6.2 Results

We applied the criteria listed in Table 6.1 to the data, excluding the events that were used in the background-study sample. As indicated before, the final data

Table 6.3: Expected $t\bar{t}$ yields, including contributions from channels other than all-jets, for our two sets of selection criteria.

	Set I	Set II
$\sum \varepsilon \times \mathrm{BR}$:		
m_t = 160 GeV/c^2	0.0070 ± 0.0018	0.0182 ± 0.0044
m_t = 180 GeV/c^2	0.0117 ± 0.0027	0.0289 ± 0.0066
m_t = 200 GeV/c^2	0.0163 ± 0.0037	0.0398 ± 0.0092
Expected $t\bar{t}$ yield:		
m_t = 160 GeV/c^2	3.67	9.54
m_t = 180 GeV/c^2	4.58	11.1
m_t = 200 GeV/c^2	4.45	11.3

sample consisted of 48,459 events, corresponding to an integrated luminosity of 48.6 pb^{-1}. We first applied the threshold requirements on H_T^{3j}, $\mathcal{C}$, N_{jets}^A, and $\mathcal{A}$, as listed in Table 6.1. The number of events in the final data sample satisfying these requirements, prior to requiring a muon-tag, was denoted by N_{data}. Then, using Equation 5.8, we determined the expected number of muon-tagged background events (N_{bkg}). Finally, we required a muon-tag, and found the number of candidate events (N_{obs}). The excess is defined as $N_{\mathrm{excess}} = N_{\mathrm{obs}} - N_{\mathrm{bkg}}$.

Before calculating the $t\bar{t}$ cross section, we introduced a small correction to N_{bkg}, for the following reason. If $t\bar{t}$ events are contained in a sample of events prior to requiring a muon-tag, the background in the corresponding muon-tagged sample will be overestimated in proportion to the fraction of $t\bar{t}$ events contained in that sample. We have chosen to correct for this effect. If N_{excess} corresponds to the number of $t\bar{t}$ events in the sample after imposing a muon-tag requirement, then dividing N_{excess} by the muon-tagging efficiency for $t\bar{t}$ events (20%) yields the approximate number of $t\bar{t}$ events in the data sample prior to requiring a muon-tag.

Table 6.4: Sources of uncertainty in N_{bkg}. These sources were discussed in Section 5.4.2.

Source	Size of effect Set I	 Set II
b-quark content	10%	10%
Tag rate parametrization	5%	5%
Main Ring activity	0.6%	0.6%
Statistical uncertainty	7%	3%
Total uncertainty	14%	12%

We can then define the estimated fraction of $t\bar{t}$ events in the sample (f_{sig}) as:

$$f_{\mathrm{sig}} = \frac{N_{\mathrm{excess}}}{0.2\, N_{\mathrm{data}}}. \tag{6.1}$$

The corrected estimate for the number of background events is then given by:

$$N_{\mathrm{bkg}}(\mathrm{corr}) = N_{\mathrm{bkg}}(1 - f_{\mathrm{sig}}). \tag{6.2}$$

This correction reduced the background estimate (and increases the signal) by 0.6 events for Set I and 1.4 events for Set II. Half this correction was added in quadrature with the uncertainty in N_{bkg} to account for the overall uncertainty of the correction.

Sources of uncertainty in N_{bkg} were discussed in Section 5.4.2. They are summarized in Table 6.4. Again, we defined the total uncertainty as the sum of the separate contributions added in quadrature.

The results obtained using the criteria of Set I and Set II are shown in Table 6.5. We have listed both the corrected and uncorrected background estimates for each set of criteria.

Table 6.5: Results of applying the criteria of Set I and Set II to DØ data.

Criteria Used	N_{data} (before tag)	N_{bkg}	N_{obs}	Excess	N_{bkg}(corr) (Eq. 6.2)
Set I	203	7.7 ± 1.1	11	3.3	7.1 ± 1.1
Set II	946	34.2 ± 4.1	42	7.8	32.8 ± 4.2

For both sets of criteria, we observe a small excess of events above the estimated background. Assuming Poisson fluctuations in the number of observed events, the standard deviation is just $\sqrt{N_{\text{obs}}}$, and the statistical significance of this excess is about one standard deviation. Consequently, we cannot state with great assurance that our data require the presence of a contribution from $t\bar{t}$ production. We emphasize that Set I and Set II do not represent independent experiments; Set I is in fact a subset of Set II.

6.3 Properties of the Candidate Events

In search of additional evidence for $t\bar{t}$ production, we have examined the properties of the 42 candidate events that satisfied the criteria of Set II. We have compared the distributions in the kinematic parameters for the events that satisfied the criteria of Set II to those expected for background. These distributions are shown in Fig. 6.3, where we have used the 946 untagged events, each weighted by its probability of having a muon-tag, to represent the expected ("predicted") background; the 42 candidate events are labeled as "observed." Aside from the total number of observed events being somewhat larger than predicted from background, we do not see a clear difference between the two distributions.

In addition, we have used the DØ event display program to examine each event

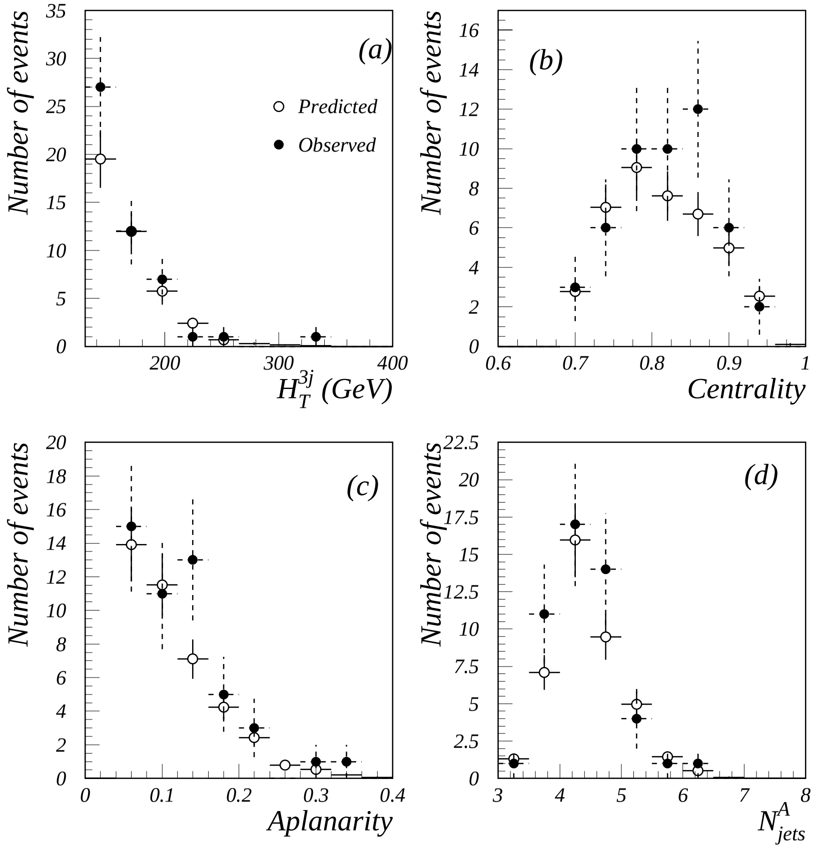

Figure 6.3: Kinematic properties of events that satisfy the criteria of Set II. Shown are distributions in H_T^{3j} (a), $\mathcal{C}$ (b), $\mathcal{A}$ (c), and N_{jets}^A (d), for predicted background (open circles) and observed events (solid circles).

that satisfied the requirements of Set II. Some of the events are quite intriguing, showing many of the properties expected for $t\bar{t}$ events. Two displays of an event, which also satisfied the criteria of Set I, are shown in Figs. 6.4 and 6.5. In these "lego" plots, η-ϕ coordinates are plotted in the horizontal plane, and E_T is represented by the height of each lego tower. Although we cannot conclude whether any given event is due to $t\bar{t}$ production, the structure of this event is quite characteristic of such processes. Figure 6.4 shows the calorimeter towers used to reconstruct jets. The patterns of hatching indicate the assignment of the towers to the jets found by DØRECO using the $\mathcal{R} = 0.3$ cone algorithm. As the figure indicates, this event has six distinct jets, each with large E_T. In Fig. 6.5, all the objects reconstructed by DØRECO are shown. The jet at $\eta = 0.7$ and $\phi = 5.6$ has a muon-tag, with $p_T(\mu)$ $= 7.3$ GeV/c. Two other muons were reconstructed by DØRECO, but both have p_T < 4 GeV/c. These muons could be the result of decays of pions or kaons from the nearby jets. We also note that DØRECO identified two "photons," but both have $E_T < 2$ GeV and could be the result of noise in the calorimeter. (As discussed in Chapter 3, DØRECO does not impose quality requirements for photons.) The clear six-jet structure seen in this event is also present in several other candidate events.

6.4 Cross Section for $t\bar{t}$ Production

Finally, assuming that the observed event excess is due to $t\bar{t}$ production, we calculated the cross section for $t\bar{t}$ production ($\sigma_{t\bar{t}}$). Our extracted cross section can be compared with previous measurements of $t\bar{t}$ production in other channels.

In calculating the cross section, we used our corrected estimate for the background:

$$\sigma_{t\bar{t}} = \frac{N_{\rm obs} - N_{\rm bkg}({\rm corr})}{(\sum \varepsilon \times {\rm BR}) \times \int \mathcal{L}dt}, \tag{6.3}$$

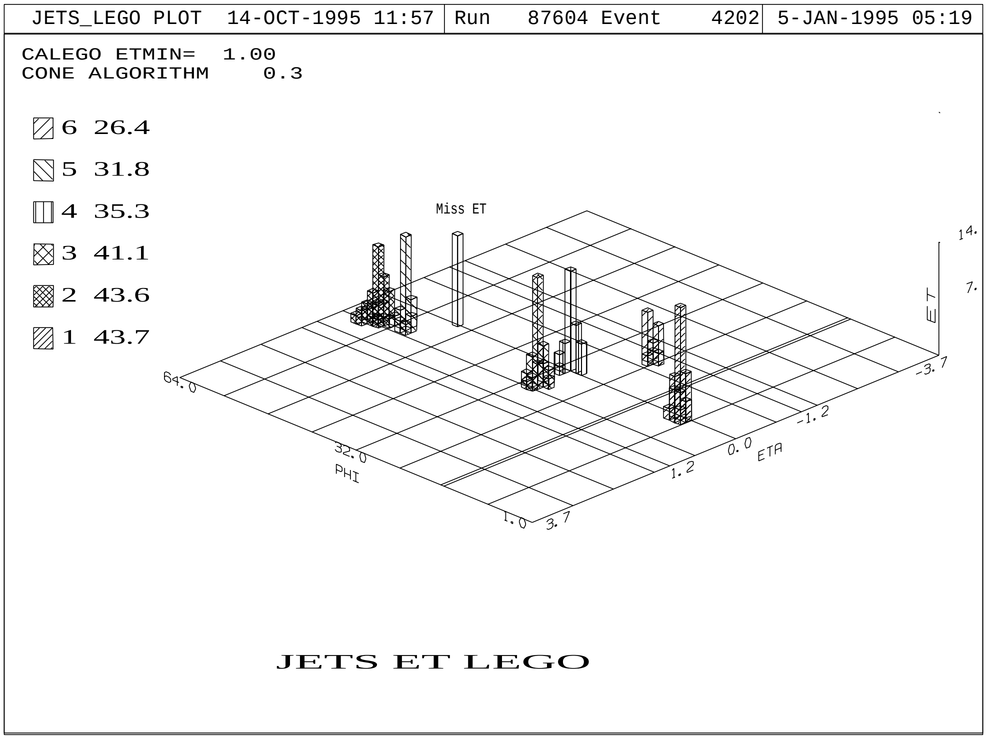

Figure 6.4: Calorimeter towers in each jet, for one of our candidate events. The E_T of each jet, prior to CAFIX corrections, is listed.

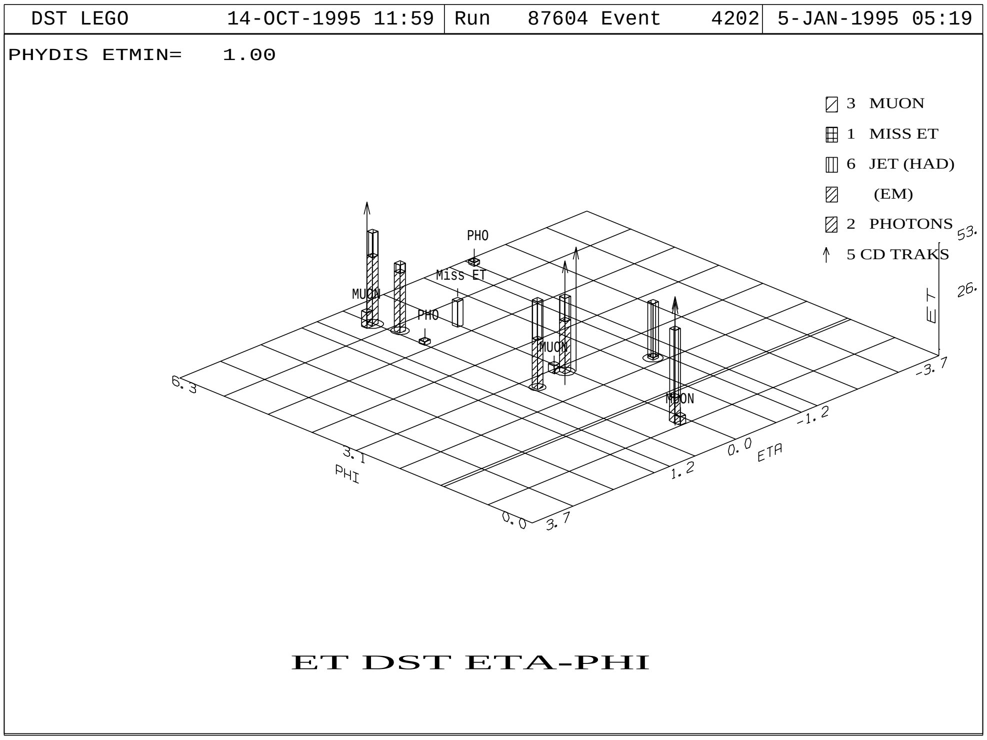

Figure 6.5: Reconstructed objects for one of our candidate events. This event has six distinct jets, one of which (at $\eta = 0.7$, $\phi = 5.6$) is tagged by a muon. Two other low-p_T muons have been reconstructed. The “photons” shown here may be due to noise.

where N_{obs} is the total number of observed events, $N_{\text{bkg}}(\text{corr})$ is the expected number of background events after correcting for the presence of $t\bar{t}$ production in untagged events (described in Section 6.2); $\sum \varepsilon \times \text{BR}$ is the sum over all decay channels of the branching ratio times the acceptance of the final criteria for selecting $t\bar{t}$ events (listed in Table 6.3); and $\int \mathcal{L}dt$ is the integrated luminosity. For purposes of determining the efficiency, we assume that $m_t = 200$ GeV/c^2.

We obtain the uncertainty in the cross section measurement from the addition of separate contributions in quadrature:

$$(\frac{\delta\sigma}{\sigma})^2 = \frac{N_{\text{obs}}}{[N_{\text{obs}} - N_{\text{bkg}}(\text{corr})]^2} + \frac{[\delta N_{\text{bkg}}(\text{corr})]^2}{[N_{\text{obs}} - N_{\text{bkg}}(\text{corr})]^2} + (\frac{\delta\varepsilon}{\varepsilon})^2 + (\delta\mathcal{L})^2, \tag{6.4}$$

where δN_{bkg} is the error in the estimated number of background tagged events (Table 6.5), $\delta\varepsilon$ is the estimated error in the acceptance, ε is the acceptance, and $\delta\mathcal{L}$ is the estimated relative error (12%) in the calculation of the integrated luminosity.

Using the criteria of Set I, we found that $\sigma_{t\bar{t}} = 4.9 \pm 4.6$ pb. (The criteria of Set II yielded a consistent value: $\sigma_{t\bar{t}} = 4.8 \pm 4.2$ pb.) Our measurement is consistent with results published by DØ from other channels [2], for which the measured value of $\sigma_{t\bar{t}}$ was 6.4 ± 2.2 pb. However, as we have indicated previously, our measured excess is consistent with zero and therefore does not establish conclusively the presence of a $t\bar{t}$ signal in the all-jets channel.

Chapter 7

Conclusion and Discussion

Using the D0 detector at Fermilab, we have searched for the top quark in the all-jets channel. The search was performed on data corresponding to an integrated luminosity of 48.6 pb^{-1}. As described in Chapter 6, we found 11 events that satisfied the final selection criteria, with an expected background of 7.7 ± 1.1 events. Based on the small excess of observed events above background, the cross section for $t\bar{t}$ production was found to be 4.9 ± 4.6 pb. Our cross section is consistent with previous measurements reported by D0 [2] and CDF [3]. Nevertheless, the signal is not sufficiently significant to establish the unambiguous existence of the channel $t\bar{t} \rightarrow$ all-jets.

We have presented a method for detecting a $t\bar{t}$ signal in the all-jets mode, which, with additional data, can provide clear evidence for a signal. Analysis of the later part of Run Ib is now in progress, and the additional data will increment the integrated luminosity to about 93 pb^{-1}. Based on the results reported in this dissertation, and assuming that no changes will be made to the selection criteria, we would expect to observe only about 19 events from all of Run I, with a predicted background of about 13 events. The statistical significance of the excess would improve, but only to about 1.3 standard deviations, which is still not large enough for claiming the unequivocal presence of a $t\bar{t}$ signal.

However, it may be possible to improve the background rejection by modifying the selection criteria. For instance, new criteria for the identification of muon-tags are being developed. These criteria will enable us to extend muon-tagging into the EF region ($1 < |\eta| < 1.7$) of the muon system, thereby increasing the acceptance for tagging heavy quarks in $t\bar{t}$ events. Furthermore, there have been recent suggestions concerning novel use of kinematic parameters. As just one example, F. Tkachov has proposed a class of parameters called "jet discriminators," which define a continuous scale for jet multiplicity in an event [92]. These parameters provide more information about multijet structure than our present jet-counting parameter, N^A_{jets}. If a practical method of calculating these jet discriminators from experimental data could be developed, our ability to reject background would improve significantly. Other parameters, which may lead to to improvements in background rejection, are also being explored [97].

We also note that more sophisticated techniques for selecting candidate events are being developed at DØ [97, 98, 99]. In this dissertation, we have used a single threshold setting on each of four kinematic parameters. While this appears to be an effective way to proceed, it does not exploit all the correlations among parameters that were noted in Chapter 5. Methods of event selection that make more use of the correlations are currently being developed. One such method, known as the artificial neural network [100], incorporates correlations among parameters in an elegant and general way. Using such techniques, we hope to improve background rejection at a fixed acceptance for signal, and thereby improve the statistical significance of our result.

Once a significant excess is established, we can attempt to measure the mass of the top quark. Unlike other decay channels, the all-jets mode does not contain high-p_T neutrinos, and consequently, complete kinematic information about the $t\bar{t}$ decay is available in the event. The principal difficulty lies in associating the jets with the correct parent partons. Each top quark decays to a b quark and a W boson, and the latter subsequently decays to two light quarks. Consequently, for an event that has six jets, there are 90 distinct assignments of the jets to the quarks. For events that have additional jets due to gluon radiation, the number of possible assignments increases rapidly. Many of the incorrect assignments yield results that are incompatible with a $t\bar{t}$ decay, and therefore, a kinematic-fitting program can be used to rule them out. Work on kinematic fitting and mass measurement in the all-jets channel is currently in progress [101], and if we can extract a data sample with a significant $t\bar{t}$ component, it should be possible to measure the mass of the top quark.

The prospects for studies of $t\bar{t} \rightarrow$ all-jets in the future are bright. Upgrades to the DØ detector and to the Fermilab accelerator complex are in progress, in preparation for the next Tevatron collider run, which is now scheduled to begin in 1999. The Main Injector, now under construction, will replace the Main Ring [102], and the addition of a new antiproton accumulator is also planned. As a result of these improvements, the luminosity in the Tevatron will increase by a factor of about ten. We can therefore expect at least ten times more data to be available from the next run.

The upgraded DØ detector [103] will be well suited to studies of $t\bar{t} \rightarrow$ all-jets. The quality of the calorimetry will remain high, and the inner tracking detectors will be replaced by a silicon vertex detector and a scintillating fiber tracker. The improved resolution of the new vertex detector will make it possible to tag b-quark jets by identifying a displaced secondary vertex inside a jet. In addition, the upgraded detector will have a magnetic field in the inner tracking region, which will make it possible to tag b-quark jets by their decays to electrons as well as to muons.

With these improvements to the detector and the accelerator, it should be possible to collect and identify a large sample of $t\bar{t}$ events with which to test the predictions of the Standard Model for the cross section and branching ratio in the all-jets channel, and in addition, to obtain a precise measurement of the mass of the top quark.

Bibliography

[1] D. Griffiths, *Introduction to Elementary Particles*, New York: John Wiley & Sons, 1987.

[2] S. Abachi *et al.* (DØ Collaboration), *Phys. Rev. Lett.* **74**, 2632 (1995).

[3] F. Abe *et al.* (CDF Collaboration), *Phys. Rev. Lett.* **74**, 2626 (1995).

[4] A. Das, T. Ferbel, *Introduction to Nuclear and Particle Physics*, New York: John Wiley & Sons, 1994.

[5] K. Gottfried, V. F. Weisskopf, *Concepts of Particle Physics* (2 vols.), New York: Oxford University Press, 1986.

[6] M. Kaku, *Quantum Field Theory: A Modern Introduction*, New York: Oxford University Press, 1993.

[7] Particle Data Group, "Review of Particle Properties," *Phys. Rev. D* **50**, 1173 (1994).

[8] R. P. Feynman, *QED: The Strange Theory of Light and Matter*, Princeton, NJ: Princeton University Press, 1985.

[9] J.T. Linneman, "Jet Physics at DØ and CDF," in *Proceedings of the XXVII International Conference on High Energy Physics: 20–27 July 1994, Glas-*

gow, Scotland, UK, P. J. Bussey and I. G. Knowles, eds., Philadelphia: Institute of Physics, 1995.

[10] G. Arnison *et al.* (UA1 Collaboration), *Phys. Lett.* **B122**, 103 (1983); *Phys. Lett.* **B126**, 398 (1983).

[11] G. Kane, *Modern Elementary Particle Physics: The Fundamental Particles and Forces?*, Reading, Mass.: Addison-Wesley Publishing Company, 1993.

[12] A. G. Clark, "Experimental Aspects of Hadron Collider Physics," in *Techniques and Concepts of High-Energy Physics VI*, T. Ferbel, ed., New York: Plenum Press, 1991.

[13] S. Abachi *et al.* (DØ Collaboration), *Phys. Rev. Lett.* **72**, 2138 (1994).

[14] F. Abe *et al.* (CDF Collaboration), *Phys. Rev. D* **50**, 2966 (1994); *Phys. Rev. Lett.* **73**, 225 (1994).

[15] E. Laenen, J. Smith, W. L. van Neerven, *Phys. Lett.* **B321**, 254 (1994).

[16] J. Donoghue, E. Golowich, B. Holstein, *Dynamics of the Standard Model*, Cambridge, England: Cambridge University Press, 1992.

[17] F. A. Berends, H. Kuijf, *Nucl. Phys.* **B353**, 59 (1991).

[18] C. J. Maxwell, *Nucl. Phys.* **B316**, 321 (1989).

[19] W. T. Giele, D. A. Kosower, H. Kuijf, "A Preliminary Calculation of the Background to t Detection with Tagged bs," *Nucl. Phys. B (Proc. Suppl.)* **23A**, 22 (1991).

[20] J. Thompson, "Introduction to Colliding Beams at Fermilab," Fermilab Preprint FERMILAB-TM-1909 (unpublished), 1994.

[21] L. M. Lederman, "The Tevatron," *Scientific American*, Vol. 264, No. 3 (March 1991), pp. 48-55.

[22] R. C. Fernow, *Introduction to Experimental Particle Physics*, New York: Cambridge University Press, 1986.

[23] C. W. Schmidt, C. D. Curtis, *IEEE Trans. Nucl. Sci.*, **NS-26**, 4120 (1979).

[24] H. T. Edwards, *Ann. Rev. Nucl. Part. Sci.* **35**, 605 (1985).

[25] S. Abachi *et al.* (DØ Collaboration), *Nucl. Instr. and Meth.* **A338**, 185 (1994).

[26] S. Aronson *et al.* (DØ Collaboration), "Design Report: The DØ Experiment at the Fermilab Antiproton-Proton Collider," DØ Note 137 (unpublished), 1984.

[27] P. Grannis, "The DØ Detector at the Fermilab Collider," DØ Note 558 (unpublished), 1987.

[28] H. Bøggild and T. Ferbel, *Ann. Rev. Nucl. Part. Sci.* **24**, 451 (1974).

[29] F. Sauli, "Principles of Operation of Multiwire Proportional and Drift Chambers," in *Experimental Techniques in High Energy Physics*, T. Ferbel, ed., Menlo Park, Calif.: Addison-Wesley Publishing Company, 1987.

[30] A. R. Clark *et al.*, *Nucl. Instr. and Meth.* **A261**, 420 (1987).

[31] A. R. Clark *et al.*, *Nucl. Instr. and Meth.* **A279**, 243 (1989).

[32] A. R. Clark *et al.*, *Nucl. Instr. and Meth.* **A315**, 193 (1992).

[33] J. H. Cochran, Jr., *Search for Truth in the eμ Channel at DØ*, Ph.D. Thesis, State University of New York at Stony Brook, December 1993 (unpublished).

[34] S. S. Snyder, *Measurement of the Top Quark Mass at DØ*, Ph.D. Thesis, State University of New York at Stony Brook, May 1995 (unpublished).

[35] V. L. Ginzberg, I. M. Frank, *JETP* **16**, 15 (1946).

[36] J. D. Jackson, *Classical Electrodynamics* (2nd Edition), New York: John Wiley & Sons, 1975.

[37] K. Kleinknecht, "Particle Detectors," in *Experimental Techniques in High Energy Physics*, T. Ferbel, ed., Menlo Park, Calif.: Addison-Wesley Publishing Company, 1987.

[38] F. Feinstein, *Etude d'un Detecteur a Rayonnement de Transition pur l'Experience DØ au FNAL*, Ph.D. Thesis, A'l'Universite de Paris-Sud, Centre d'Orsay, December 1987 (unpublished).

[39] J.-F. Detœuf *et al.*, *Nucl. Instr. and Meth.* **A279**, 310 (1989).

[40] Y. Ducros *et al.*, *Nucl. Instr. and Meth.* **A277**, 401 (1989).

[41] D. Pizzuto, *DØ Central Tracking Chamber Performance Studies*, Ph.D. Thesis, State University of New York at Stony Brook, December 1991 (unpublished).

[42] T. Behnke, *The Central Drift Chamber for the DØ Experiment: Design, Construction, and Test*, Ph.D. Thesis, State University of New York at Stony Brook, August 1989 (unpublished).

[43] J. W. Bantly, *The DØ Detector Forward Drift Chamber Performance and Physics Capability in the 1990 FNAL Testbeam Run*, Ph.D. Thesis, Northwestern University, June 1992 (unpublished).

[44] R. Avery *et al.*, *IEEE Trans. Nucl. Sci.* **NS-40**, 573 (1993).

[45] C. W. Fabjan, R. Wigmans, *Rept. Prog. Phys.* **52**, 1519 (1989).

[46] C. Fabjan, "Calorimetry in High-Energy Physics," in *Experimental Techniques in High Energy Physics*, T. Ferbel, ed., Menlo Park, Calif.: Addison-Wesley Publishing Company, 1987.

[47] R. Wigmans, *Nucl. Instr. and Meth.* **A265**, 273 (1988).

[48] S. J. Wimpenny *et al.*, *Nucl. Instr. and Meth.* **A279**, 107 (1989).

[49] A. L. Spadafora *et al.*, *Nucl. Instr. and Meth.* **A315**, 279 (1992).

[50] P. Franzini *et al.*, *Nucl. Instr. and Meth.* **A289**, 438 (1990).

[51] H. Aihara *et al.*, *IEEE Trans. Nucl. Sci.* **NS-38**, 398 (1991).

[52] S. Abachi *et al.* (DØ Collaboration), *Nucl. Instr. and Meth.* **A324**, 53 (1992).

[53] K. Streets, "The DØ Inter-Cryostat Detector, Massless Gaps, and Missing E_T Resolution," in *Proceedings of the Third International Conference on Calorimetry in High-Energy Physics: Corpus Christi, Texas, September 29–October 2, 1992*, P. Hale, J. Siegrist, eds., Singapore: World Scientific, 1993.

[54] C. Brown *et al.*, *Nucl. Instr. and Meth.* **A279**, 331 (1989).

[55] J. M. Butler *et al.*, *Nucl. Instr. and Meth.* **A290**, 122 (1990).

[56] Yu. M. Antipov *et al.*, *Nucl. Instr. and Meth.* **A297**, 121 (1990).

[57] S. Abachi *et al.* (DØ Collaboration), *Phys. Rev. D* **52**, 4877 (1995).

[58] G. S. Gao, R. Partridge, *IEEE Trans. Nucl. Sci.* **NS-38**, 286 (1991).

[59] J. Bantly *et al.*, "The Level 0 Trigger for the DØ Detector," DØ Note 1996, 1993. Submitted to *IEEE Trans. Nucl. Sci.*.

[60] N. Amos, "Main Ring Veto Counters for Run 1b," DØ Note 2072, 1994 (unpublished).

[61] M. Abolins *et al.*, *IEEE Trans. Nucl. Sci.* **NS-36**, 384 (1989).

[62] M. Abolins *et al.*, *Nucl. Instr. and Meth.* **A289**, 543 (1990).

[63] M. Fortner *et al.*, *IEEE Trans. Nucl. Sci.* **NS-38**, 480 (1991).

[64] D. Cutts *et al.*, *IEEE Trans. Nucl. Sci.* **NS-36**, 738 (1989).

[65] D. Cutts *et al.*, "Operation of the DØ Data Acquisition System," in *Proceedings of the International Conference on Computing in High-Energy Physics '92: Annecy, France*, C. Verkerk, W. Wojcik, eds., CERN 92-07, 1992.

[66] J. T. Linnemann *et al.*, "The DØ Software Trigger," in *Proceedings of the International Conference on Computing in High-Energy Physics '92: Annecy, France*, C. Verkerk, W. Wojcik, eds., CERN 92-07, 1992.

[67] M. Goosens *et al.*, *ZEBRA*, CERN Program Library Number Q100 (1992).

[68] G. Manning *et al.* (DØ Collaboration), "DØ Software Documentation" (in preparation), July 1995.
URL: `http://d0wop.fnal.gov/software/offline_document.ps`

[69] A. Para *et al.*, "The DØ Offline Production and Analysis," in *Proceedings of the International Conference on Computing in High-Energy Physics '92: Annecy, France*, C. Verkerk, W. Wojcik, eds., CERN 92-07, 1992.

[70] S. Kunori, private communication.

[71] K. Denisenko, "TPM Production Manager Operator's Manual and User's Guide," DØ Note 2024, 1994 (unpublished).

[72] H. Schellman, private communication.

[73] M. F. Paterno, *A Search for Squarks and Gluinos in* $p\overline{p}$ *Collisions at* $\sqrt{s} = 1.8$ *TeV with the DØ Detector*, Ph.D. Thesis, State University of New York at Stony Brook, May 1994 (unpublished).

[74] S. Youssef, *Comp. Phys. Comm.* **45**, 423, 1987.

[75] C. Stewart, C. Cretsinger, E. Won, "Search for the Top Quark in the All-Jets Channel at DØ ," DØ Note 2588A, 1995 (unpublished).

[76] O. Dahl *et al.*, "Kinematic Fitting for the Mass of the Top Quark," DØ Note 2408, 1995 (unpublished).

[77] A. J. Milder, *Dijet Angular Distributions in* $p\overline{p}$ *Collisions at* $\sqrt{s} = 1800$ *GeV Using the DØ Detector*, Ph.D. Thesis, University of Arizona, 1993 (unpublished).

[78] F. Abe *et al.* (CDF Collaboration), *Phys. Rev. Lett.* **69**, 2896 (1992).

[79] A. Milder, R. Astur, "Jet Energy Calibration using the Missing E_T Projection Fraction," DØ Note 1657, 1993 (unpublished).

[80] T. Joffe-Minor, R. Astur, "A Study of the Effects of the CAFIX Energy Scale Corrections," DØ Note 2211, 1994 (unpublished).

[81] S. Ahn, private communication.

[82] C. Cretsinger, C. Stewart, "Preliminary Study of Parameters for Top to Jets Event Selection," DØ Note 2499, 1995 (unpublished).

[83] F. James, "Monte Carlo Theory and Practice," in *Experimental Techniques in High Energy Physics*, T. Ferbel, ed., Menlo Park, Calif.: Addison-Wesley Publishing Company, 1987.

[84] B. R. Webber, *Ann. Rev. Nucl. Part. Sci.* **36**, 253 (1986).

[85] F. Paige, S. Protopopescu, BNL Report No. BNL38034, 1986 (unpublished), release v. 6.49.

[86] G. Marchesini, *et al.*, *Comp. Phys. Comm.*, **67**, 465, 1992.

[87] F. Carminati, *et al.*, "GEANT User's Guide," CERN Program Library, 1991 (unpublished).

[88] N. Graf, "The DØ Shower Library," in *Proceedings of the First International Conference on Calorimetry in High Energy Physics: Fermi National Accelerator Laboratory, Batavia, Ill., 29 October–1 November 1990*, D. F. Anderson *et al.*, eds., Teaneck, NJ: World Scientific, 1991.

[89] J. Bantly, private communication.

[90] A. Castro *et al.* (CDF Collaboration), "Multi-jet Analysis for the Top Search at the Fermilab Collider," Fermilab preprint FERMILAB-Conf-94/152-E (CDF), June 1994 (unpublished).

[91] V. D. Barger, R. J. N. Phillips, *Collider Physics*, Reading, Mass.: Addison-Wesley, 1987.

[92] F. V. Tkachov, "Calorimetric Measurements and Jet Counting," in *Proceedings of the Joint International Workshop: VIII Workshop on High Energy Physics and Quantum Field Theory & III Workshop on Physics at VLEPP,*

Zvenigorod, Russia, 15-21 September 1993, B. B. Levtchenko, ed., Moscow: Izdatel'sto Moskovskovo Universiteta, 1994.

[93] H. Xu, *Search for the Top Quark in the Electron + Jets + Soft Muon Channel at DØ*, Ph.D. Thesis, Brown University, 1995 (unpublished).

[94] R. Yamada, "c-Tagging of Jets from W Decays," DØ Note 2250, FERMILAB-FN-625, 1994 (unpublished).

[95] J. Hobbs, H. Zhu, private communication.

[96] C. Stewart, E. Won, private communication.

[97] N. Amos, private communication.

[98] J. Moromisato, private communication.

[99] H. Prosper, private communication.

[100] C. Peterson, T. Rögnvaldsson, *Comp. Phys. Comm.*, **81**, 185 (1994).

[101] E. Won, "A Preliminary Analysis of the Mass of the Top Quark Using SQUAW in the All-jets Channel," DØ Note 2586, 1995 (unpublished).

[102] C. S. Mishra, "The Fermilab Main Injector," in *Proceedings of the Annual Meeting of the Division of Particles and Fields of the American Physical Society, Batavia, Illinois, 10–14 November 1992.*

[103] The DØ Collaboration, "E823 (The DØ Upgrade)," DØ Note 1733, 1993 (unpublished).

Appendix A

Consistency Check of the Grid Search

As mentioned in Chapter 6, we studied six other sets of thresholds, in addition to Set I and Set II. The purpose of this study was to confirm that the results obtained from the grid search are stable over a range of possible choices of thresholds on the kinematic parameters.

Each of the six sets of criteria used to confirm the consistency of the results corresponds to a point on the optimal boundary shown in Fig. 6.2. The values of the thresholds on H_T^{3j}, $\mathcal{C}$, N_{jets}^{A}, and $\mathcal{A}$ are listed in Table A.1. The expected acceptance ($\varepsilon_{\text{all-jets}}$) and yields for signal (assuming $m_t = 200$ GeV/c^2) and background, based on the output from the grid-search algorithm, are listed in Table A.2.

To determine whether the results depend on the criteria chosen, we applied each of the sets of criteria listed in Table A.1 to the 48,459 events in the final data sample, just as we did for Set I and Set II in Chapter 6. We then used any observed excess to calculate a cross section for $t\bar{t}$ production, following the procedures described in Chapter 6. This allowed us to verify the consistency of

Table A.1: Threshold values for six sets of criteria used for the consistency study.

	Threshold Values			
Set No.	H_T^{3j} (GeV)	$\mathcal{C}$	N_{jets}^{A}	$\mathcal{A}$
1	130.6	0.571	3.13	0.057
2	137.2	0.522	3.46	0.052
3	136.2	0.669	3.67	0.072
4	137.8	0.682	3.68	0.088
5	147.8	0.550	3.18	0.112
6	142.7	0.619	4.26	0.184

Table A.2: Acceptance and expected yields for six sets of criteria used for the consistency study.

Set No.	$\varepsilon_{\text{all-jets}}$	$N_{t\bar{t}}$	N_{bkg}
1	0.0826	11.3	50.6
2	0.0793	10.9	42.4
3	0.0638	8.74	26.6
4	0.0544	7.44	18.0
5	0.0437	5.98	11.6
6	0.0173	2.37	1.59

Table A.3: Results from the six sets of criteria used for the consistency study.

Criteria	N_{data}	N_{bkg}	N_{obs}	Excess	$\sum \varepsilon \times \text{BR}$	$\sigma_{t\bar{t}}(\text{pb})$
1	1537	50.1 ± 6.0	61	10.9	0.046 ± 0.011	5.7 ± 4.7
2	1266	41.8 ± 5.0	51	9.2	0.044 ± 0.010	5.0 ± 4.4
3	761	26.9 ± 3.5	33	6.1	0.035 ± 0.008	4.3 ± 4.2
4	555	19.8 ± 2.6	27	7.2	0.029 ± 0.007	5.9 ± 4.4
5	359	12.7 ± 1.7	14	1.3	0.024 ± 0.005	1.3 ± 3.6
6	80	2.9 ± 0.5	2	-0.9	0.009 ± 0.002	-2.1 ± 3.6

the results in a straightforward manner. The results are listed in Table A.3. As usual, the values of $\sum \varepsilon \times \text{BR}$, listed in Table A.3, include contributions from all $t\bar{t}$ decay channels.

We see that, except for the most restrictive criteria (Set 6), all sets of criteria yielded an excess. The statistical significance of the excess is ≤ 1.4 standard deviations, not large enough to confirm the presence of $t\bar{t}$ production. Within their uncertainties, the cross sections calculated for the six sets of criteria are all consistent with each other. They are also consistent with the cross section reported in Chapter 6. We emphasize that there is considerable overlap among the data samples that satisfy these sets of criteria, so that this study does not constitute an independent validation of the results presented in Chapter 6. This study simply shows that the results do not depend strongly on the particular criteria chosen.